
AIJ Benchmarks for Validation of CFD Simulations Applied to Pedestrian Wind Environment around Buildings



Architectural Institute of Japan

Copyright © 2016 Architectural Institute of Japan. All Rights Reserved.

AIJ Benchmarks for Validation of CFD Simulations
Applied to Pedestrian Wind Environment around Buildings

Architectural Institute of Japan
5-26-20, Shiba, Minato-ku, Tokyo 108-8414, JAPAN
Tel: +81-3-3456-2051
Fax: +81-3-3456-2058
<https://www.aij.or.jp/>

Issued **September 26, 2016**
ISBN978-4-8189-5001-6 C3052

Edited and published by Architectural Institute of Japan

Notice

Copyright of this publication is proprietary to the Architectural Institute of Japan and is protected under the Copyright Act of Japan and other acts and conventions. Private use by the individual or other use (including reproduction, modification, or distribution) of the publication beyond the scope permitted by the Copyright Act is prohibited without the permission of the right holder.

The Architectural Institute of Japan has made every effort to assure the accuracy of this publication and shall not be liable for any decision or act that the User makes by using the information contained in this publication.

PREFACE

As computer facilities and computational fluid dynamics (CFD) software have been significantly improved in recent years, the prediction and assessment of the pedestrian wind environment around buildings using CFD have become practical at design stages. Therefore, guidelines that summarize important points for using the CFD technique for appropriate prediction of the pedestrian wind environment are required. To this end, a working group for CFD prediction of the pedestrian wind environment around buildings was established in the Architectural Institute of Japan (AIJ); they started providing practical guidelines for applying CFD to the pedestrian wind environment around buildings from 2001. After years of discussion and experience on numerical and physical experimental studies, in 2007, the working group compiled and published '*The guidebook of CFD for predicting pedestrian wind environment around buildings: guidelines and validation database*' in Japanese, which contains the proposed guidelines, fundamental knowledge of CFD applied to an urban wind environment, and the results of benchmark tests. The results of the benchmark tests formed the basis for the guidelines. In the benchmark tests, cross comparisons were conducted between the results of CFD predictions, wind tunnel tests, and field measurements for seven test cases, which have been conducted for investigating the influence of many types of computational conditions for various flow fields. This part also includes information on the computational details used by the working group members. The proposed guidelines by AIJ has been published as a peer-reviewed journal paper in English (Tominaga et al., 2008) and it has been referred to by researchers worldwide. However, complete results of the benchmark test have not been published in English, although some parts have already been published as English journal papers (Mochida, 2002; Tominaga et al., 2004; Yoshie et al., 2007).

Owing to strong requests from inside and outside Japan, AIJ has decided to publish this booklet in English in order to share the complete results of the benchmark tests with the international research community. These benchmark tests were mainly conducted from 2005 to 2006. Although we are convinced that most of the results are still useful for researchers and practitioners at present, relevant studies have progressed annually. We recommend you use this booklet along with other relevant recent research.

July, 2016

Architectural Institute of Japan

List of Committee members:

Research Committee on Environmental Engineering

Chairman	Hirofumi Hayama
Secretaries	Toshie Iwata
	Koki Kikuta
Members	Hisashi Kotani
	(omitted)

Managing Committee on Publication of Environmental Engineering

Chairman	Kimiya Murakami
Secretaries	Junta Nakano
	Takahiro Tanaka
Members	(omitted)

Sub Committee for CFD Prediction of pedestrian wind environment around buildings

Chairman	Akashi Mochida (Tohoku University)
Secretaries	Yoshihide Tominaga (Niigata Institute of Technology)
Members	Yoshihiro Ishida (Institute of Industrial Science, the University of Tokyo) Takeshi Ishihara (The University of Tokyo) Kiyoshi Uehara (National Institute for Environmental Studies) Hiroto Kataoka (Obayashi Corporation) Takashi Kurabuchi (Tokyo University of Science) Nobuyuki Kobayashi (Tokyo Polytechnic University) Ryozo Ooka (Institute of Industrial Science, the University of Tokyo) Taichi Shirasawa (Tokyo Polytechnic University) Naoya Tsuchiya (Takenaka Corporation) Yoshitami Nonomura (Fujita Corporation) Tsuyoshi Nozu (Shimizu Corporation) Kazuyoshi Harimoto (Taisei Corporation) Kazuki Hibi (Shimizu Corporation) Shuzo Murakami (Keio University) Ryuichiro Yoshie (Tokyo Polytechnic University) Masaru Yoshikawa (Taisei Corporation)

(Members and their affiliations in the published year of the original guidebook)

References:

- Mochida, A., Tominaga, Y., Murakami, S., Yoshie, R., Ishihara, T., Ooka, R., 2002. Comparison of various $k-\epsilon$ model and DSM applied to flow around a high-rise building - report on AIJ cooperative project for CFD prediction of wind environment -, Wind & Structures 5, 227-244.
- Tominaga, Y., Mochida, A., Shirasawa, T., Yoshie, R., Kataoka, H., Harimoto, K., Nozu, T., 2004. Cross comparisons of CFD results of wind environment at pedestrian level around a high-rise building and within a building complex, Journal of Asian Architecture and Building Engineering 3, 63-70.
- Yoshie, R., Mochida, A., Tominaga, Y., Kataoka, H., Harimoto, K., Nozu, T., Shirasawa, T., 2005. Cooperative

project for CFD prediction of pedestrian wind environment in the Architectural Institute of Japan, Journal of Wind Engineering and Industrial Aerodynamics 95, 1551-1578.

Tominaga, Y., Mochida, A., Yoshie, R., Kataoka, H., Nozu, T., Yoshikawa, M., Shirasawa, T., 2008. AIJ guidelines for practical applications of CFD to pedestrian wind environment around buildings, Journal of Wind Engineering and Industrial Aerodynamics 96, 1749-1761.

Contents

1	Outline of benchmark tests	
1.1	Purpose of benchmark tests	1
1.2	Test case table	1
2	Benchmark tests of flow around a single-building model	
2.1	Flow around a high-rise building with a 2:1:1 shape (RANS model)	3
2.1.1	Outline of object wind tunnel test	
2.1.2	Preliminary calculations for setting the ground surface boundary conditions for the benchmark test	
2.1.3	Calculation conditions for the benchmark test (basic calculation conditions)	
2.1.4	Results of preliminary calculations based on standard $k-\varepsilon$ model and basic calculation conditions	
2.1.5	Impact of various calculation conditions on calculation results	
2.1.6	Results of benchmark tests by different organizations—impact of turbulence model	
2.1.7	Impact of grid system	
2.2	Flow around a high-rise building with a 2:1:1 shape (LES)	24
2.2.1	Impact of inflow turbulence	
2.2.2	Impact of Smagorinsky constant	
2.3	Flow around a high-rise building with a 4:4:1 shape	41
2.3.1	Outline of object flow field	
2.3.2	Effects of various boundary conditions (study of benchmark basic calculation conditions)	
2.3.3	Results of benchmark tests by several organizations—mainly the effect of the turbulence model	
2.3.4	Summary of the analysis of flow around a high-rise building with a 4:4:1 shape	
2.4	Summary of the benchmark tests of flow around a single-building model	54
3	Benchmark tests of flow around building group models	
3.1	Flow around a simple building group model	56
3.1.1	Introduction	
3.1.2	Outline of wind tunnel experiment	
3.1.3	Calculation conditions	
3.1.4	Analysis results	
3.1.5	Summary of the analysis of flow around a simple building group model	
3.2	Flow around a high-rise building in a multi-block model	65
3.2.1	Outline of wind tunnel experiment	
3.2.2	Results of wind tunnel experiments	
3.2.3	Calculation conditions	
3.2.4	Analysis cases	
3.2.5	Comparison of analysis results	
3.2.6	Summary of the analysis of flow around a high-rise building in a multi-block model	

4	Benchmark tests of flow in actual city block	
4.1	Introduction	79
4.2	Flow around a building complex in an actual urban area with dense concentration of low-rise buildings in Niigata City	79
4.2.1	Building complex studied	
4.2.2	Outline of wind tunnel experiment	
4.2.3	Outline of CFD simulations	
4.2.4	Comparison according to wind speed ratio	
4.2.5	Comparison according to wind environment evaluation scale	
4.2.6	Summary of the analysis of flow around a building complex in an actual urban area with dense concentration of low-rise buildings in Niigata City	
4.3	Flow around a group of high-rise buildings in the Shinjuku sub-central area	92
4.3.1	Outline of wind tunnel experiments and measurements compared	
4.3.2	Outline of numerical calculation	
4.3.3	Comparison of wind speed ratios	
4.3.4	Summary of the analysis of flow around a group of high-rise buildings in the Shinjuku sub-central area	
4.4	Summary of the benchmark tests of flow in actual city block	97
5	Benchmark test of flow around trees	
5.1	Introduction	98
5.2	Outline of measurements of objects for comparison	98
5.3	Outline of numerical calculations	99
5.4	Impact of boundary conditions/parameters	101
5.4.1	Impact of grid discretization (comparison of TU1 and TU2)	
5.4.2	Differences between analysis codes under identical conditions (comparison of TU1, TU3, and O7)	
5.4.3	Impact of turbulence model (TU1, TU3, TU2, and TU5)	
5.4.4	Impact of ground surface boundary conditions (comparison of O2 and O7)	
5.4.5	Impact of leaf area density a (comparison of O6 and O10)	
5.4.6	Impact of resistance coefficient C_f (comparison of O7 and O8)	
5.4.7	Impact of model coefficient C_{pel} (comparison of TU2 and TU4)	
5.4.8	Comparison of type B and type C tree canopy models (comparison of TU5 and TU6)	
5.5	Summary of the benchmark test of flow around trees	105
References		106

1. Outline of benchmark tests [42]

1.1 Purpose of benchmark tests

Benchmark tests for various flow fields were conducted to provide practical guidelines for identifying calculation conditions and methods to be used, such as boundary conditions or turbulence models, in the application of computational fluid dynamics (CFD) to analysis of the pedestrian wind environment around buildings. In the benchmark tests, the same target flows were analyzed using commonly applied calculation methods and different CFD codes possessed by the committee members' organization of the Working Group. The benchmark tests were conducted to assess the sensitivity of various calculation conditions on the prediction results obtained under circumstances in which the boundary conditions were set to be as close to identical as possible. A detailed implementation manual was prepared for the benchmark tests, and the CFD simulations were performed based on the manual. The specific settings given in the manual were prepared based on the members' past experience and knowledge related to CFD simulations for flow around buildings.

The wind tunnel experiment results presented in this booklet can also be viewed as a validation database on the following web site:

<http://www.aij.or.jp/jpn/publish/cfdguide/index.htm>

1.2 Test case table

The seven benchmark test cases described in this booklet are listed in Table 1-2-1. Outlines of these test cases are shown in Figures 1-2-1 to 1-2-7.

Table 1-2-1. Benchmark test cases

Case		Wind directions	Target experiment/measurement	
			Anemometer	References
A single high-rise building model	2:1:1 shape	0°	Split fiber probe (SFP)	[1][2]
	4:1:1 shape	0°	SFP	[3]
City blocks	Simple city blocks	0°, 22.5°, 45°	Thermistor anemometry	[4]
	A high-rise building in city blocks	0°, 22.5°, 45°	SFP, thermistor anemometry	-
Building complexes in actual urban areas	Niigata	16 wind directions	Thermistor anemometry	-
	Shinjuku	16 wind directions	Thermistor anemometry (wind tunnel) three-cup anemometer (field measurement)	[5][6]
Tree model	Tsuiji pines	0°	Three-dimensional ultrasonic anemometers (field measurement)	[7]

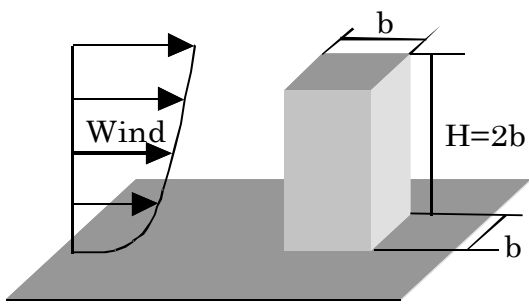


Figure 1-2-1. A single high-rise building
(2:1:1 shape)

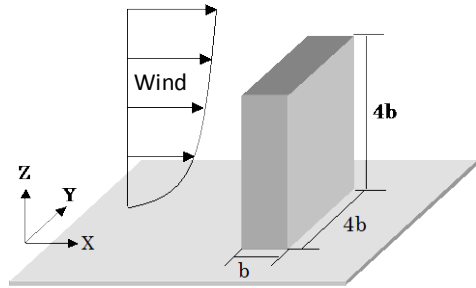


Figure 1-2-2. A single high-rise building
(4:4:1 shape)

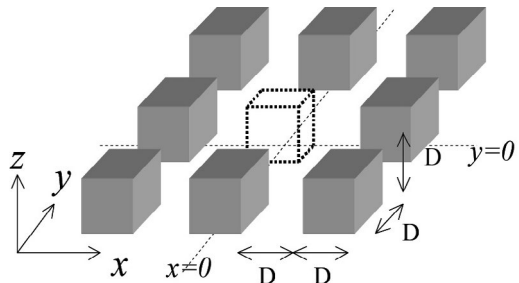


Figure 1-2-3. Simple city blocks

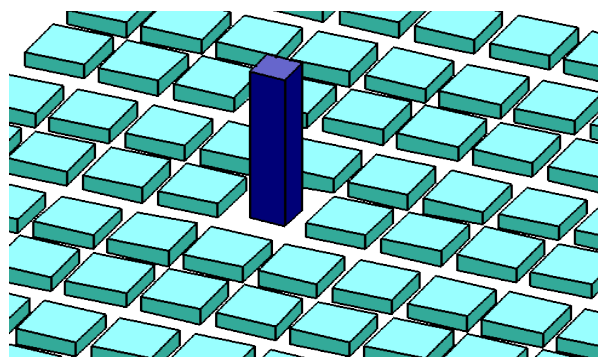


Figure 1-2-4. A high-rise building among city blocks

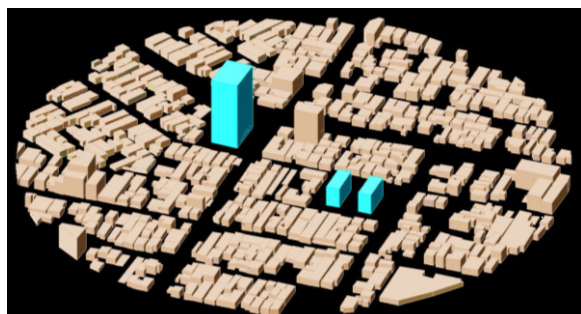


Figure 1-2-5. Building complexes in actual urban areas (Niigata)

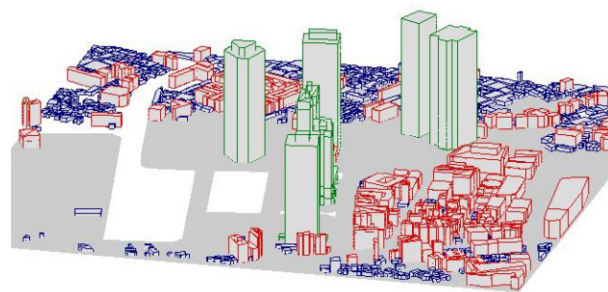


Figure 1-2-6. Building complexes in actual urban areas (Shinjuku)

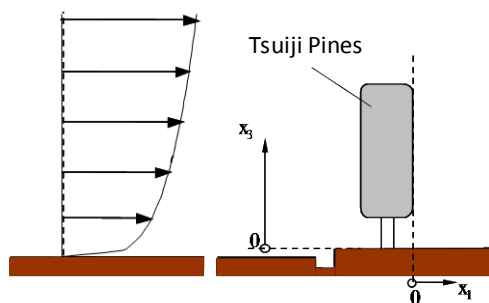


Figure 1-2-7. Tree model

2. Benchmark tests of flow around a single-building model

2.1 Flow around a high-rise building with a 2:1:1 shape (RANS model)

2.1.1 Outline of wind tunnel test

In the benchmark test for a high-rise building with a 2:1:1 (height: width: depth) shape, the experimental results reported by Meng and Hibi [1] were used to verify the CFD simulation results. This experiment involved detailed measurement of the flow field around a 2:1:1-shaped building placed in a turbulent boundary layer. The exponent for the power law of the vertical profile of the mean inflow velocity was approximately 0.27 (Figure 2-1-1). The time-averaged wind velocities and the standard deviation of the fluctuating velocities were measured three-dimensionally using a split fiber probe. The model building was 0.08 m in width and depth (b) and 0.16 m in height (h). The turbulence was measured on a vertical section of the building center ($y/b = 0$) and on planes at 1/16 ($z/b = 0.125$) and 10/16 ($z/b = 1.25$) of the building height. The measurement points are shown in Figure 2-1-2 and Figure 2-1-3.

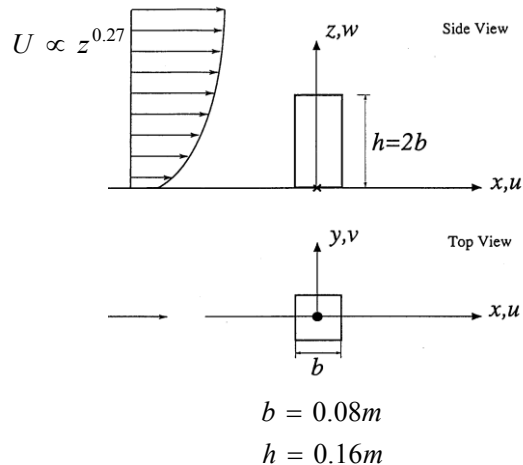


Figure 2-1-1. Configuration of the experimental model [1]

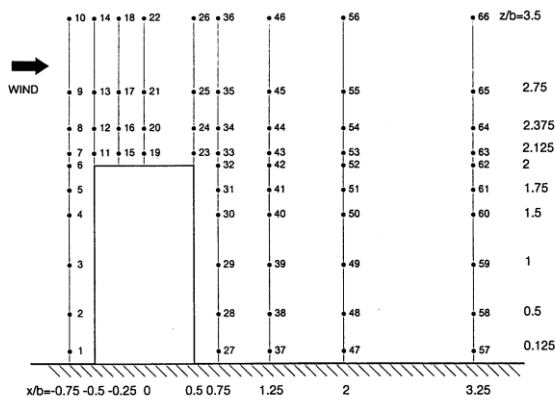


Figure 2-1-2. Measurement points on the vertical section ($y = 0$)

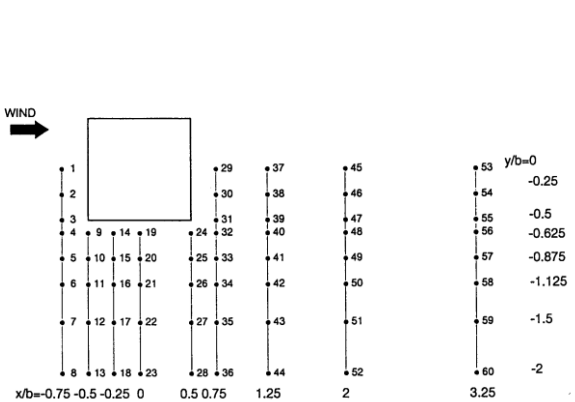


Figure 2-1-3. Measurement points on the horizontal section ($z = 0.125b$ and $1.25b$)

2.1.2 Preliminary calculations for setting the ground surface boundary conditions for the benchmark test [8]

2.1.2.1 Purpose

When analyzing a simple boundary layer flow without a building, it is important to reproduce accurately the horizontal change in the vertical profile of the average wind speed above the wind tunnel floor. This depends on appropriate selection of the surface boundary conditions. To identify appropriate ground surface boundary conditions for use in the benchmark test, a fundamental study of simple boundary layer flow was performed.

2.1.2.2 Outline of calculation

- Software: STREAM ver.2.10
- Turbulence model: standard $k-\varepsilon$ model
- Computational domain: $20b (x) \times 7.68b (z)$ (two-dimensional)
- Grid discretization: $40 (x) \times 32 (z)$. The grid width adjacent to the ground surface was $0.102b (= 0.0082 \text{ m})$, and the expansion ratio was 1.05 in the vertical direction.
- The difference scheme for the convection terms was QUICK.
- Boundary conditions: the mean wind velocity and k at the inflow boundary were obtained by interpolating the profile obtained from the experiment [1]. The value of ε was obtained from the following equation, assuming local equilibrium of the production term P_k in the k equation.

$$\varepsilon \equiv P_k \equiv - \langle u' w' \rangle \frac{\partial \langle u \rangle}{\partial z} \quad (2.1.1)$$

Here, if it is presumed that $-\langle u' w' \rangle \equiv C_\mu^{1/2} k$,

$$\varepsilon \equiv C_\mu^{1/2} k \frac{\partial \langle u \rangle}{\partial z} \quad (2.1.2)$$

The gradients of variables normal to the upper and outflow boundaries were considered to be equal to zero.

2.1.2.3 Comparison of ground surface boundary conditions

The following three types of ground surface boundary conditions were compared using the six cases listed in Table 2-1-1.

Table 2-1-1. Computed cases for investigation of ground surface boundary condition

Case 1	Logarithmic law for smooth wall	
Case 2	Power-law type	Power index: 1/7
Case 3	z_0 type	$z_0 = 1.36 \times 10^{-6} \text{ m}$
Case 4	z_0 type	$z_0 = 1.36 \times 10^{-5} \text{ m}$ (case 3 \times 10)
Case 5	z_0 type	$z_0 = 1.36 \times 10^{-4} \text{ m}$ (case 3 \times 100)
Case 6	z_0 type	$z_0 = 1.10 \times 10^{-3} \text{ m}$ (Case 3 \times 800)

a) Case using logarithmic law for smooth surface (case 1)

$$\frac{\langle u \rangle_P}{u_*} = \frac{1}{\kappa} \ln \frac{u_* h_P}{v} + 5.5 \quad (2.1.3)$$

Using the wind velocity adjacent to the wall surface $\langle u \rangle_P$ and the distance from the wall surface h_P , u_* is obtained by iteration using eq. (2.1.3). The wall surface stress $\tau_w = \rho u_*^2$ is an input to the momentum equations.

b) Case using power law (case 2)

$$\frac{\langle u \rangle_0}{\langle u \rangle_P} = \left(\frac{h_0}{h_P} \right)^{1/m} \quad (2.1.4)$$

The virtual wind velocity $\langle u \rangle_0$ at the inside of the wall surface is estimated based on the 1/7 power law, using its distance from the wall surface h_0 , the wind velocity $\langle u \rangle_P$, and the distance of the first fluid cell from the wall surface h_P . The velocity gradient on the wall surface is an input to the momentum equation.

c) Case using logarithmic law of z_0 (cases 3 to 6)

$$\frac{\langle u \rangle_P}{u_*} = \frac{1}{\kappa} \ln \frac{h_P}{z_0} + A \quad (\text{for this calculation, } A = 0) \quad (2.1.5)$$

By assuming a value for z_0 , u_* is obtained from the wind velocity adjacent to the wall surface $\langle u \rangle_P$ and the distance from the wall surface h_P . The wall surface stress $\tau_w = \rho u_*^2$ is an input to the momentum equation, as in the case of equation (2.1.3). The selection of a value for z_0 is important. In this study, the value was estimated to be $z_0 = 1.36 \times 10^{-6}$ m, based on the velocity gradient near the ground surface in the inflow velocity profile for this experiment, but the calculations were also performed by multiplying this value 10, 100, and 800 times for purposes of comparison.

2.1.2.4 Calculation results

Figure 2-1-4 shows the velocity distributions near the floor surface at locations $5b$ and $10b$ downwind of the inflow boundary. In case 3 (\times), for which the smallest z_0 value was used, the wind velocity near the ground surface recovered most near the ground surface, but in case 6 (\bullet), for which the largest z_0 value was used, the deficit of the velocity was too large. There was little difference between the results obtained using the logarithmic law (case 1) and those obtained using the power law (case 2), but recovery of velocities was observed in both cases. The velocity profile at the inflow boundary was maintained best in case 5.

In case 3, even though the value of z_0 was obtained from the experimental velocity distribution, it was too small. This was attributed to the fact that the velocity gradient near the floor surface was formed by friction with the wind tunnel floor surface but that the structure of the overall boundary layers, including the higher wind velocity gradient, was governed by the degree of roughness upwind of the wind tunnel. Thus, a larger z_0 was suitable for maintaining the inflow profile. The value of $z_0 = 1.36 \times 10^{-4}$ m (100 times case 3) that was used for case 5 can be interpreted as follows. First, the value of k ($0.37 \text{ m}^2/\text{s}^2$) for the measurement point closest to the wall surface ($z = 0.0625b$) was used to estimate u_* by solving eq. (2.1.6).

$$u_* \cong C_\mu^{1/4} \sqrt{k} = 0.09^{1/4} \sqrt{0.37} = 0.33 \text{ m/s} \quad (2.1.6)$$

The value of $z_0 = 1.8 \times 10^{-4}$ m was obtained by substituting this u_* value and the wind velocity at the measurement height of the k value (2.75 m/s) into the equation (2.1.5). This z_0 value was almost equal to the value of z_0 used in case 5. The results of the calculation obtained using $z_0 = 1.8 \times 10^{-4}$ m are shown in Figure 2-1-5 (1). This profile agrees

well with the results shown in Figure 2-1-5 (2) along every measurement line. Therefore, the z_0 -type logarithmic law with $z_0 = 1.8 \times 10^{-4}$ m was used in the benchmark test.

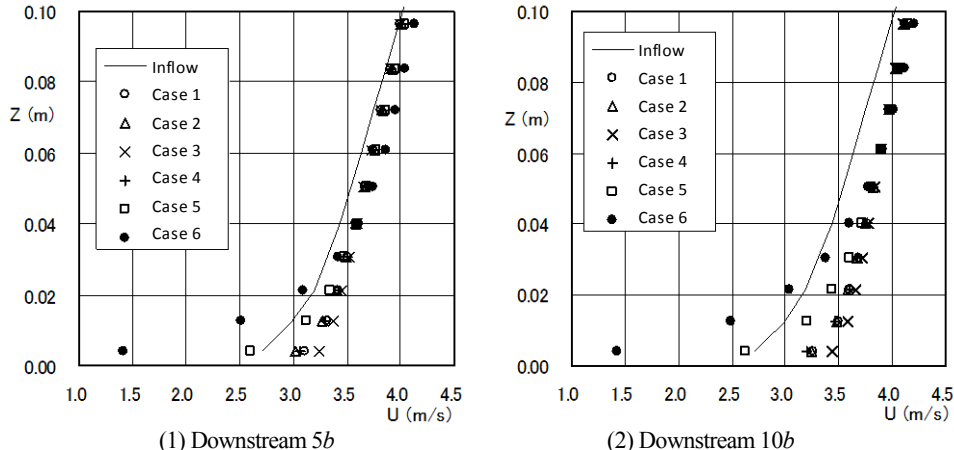


Figure 2-1-4. Vertical profiles of $\langle u \rangle$ in downstream position (calculations)

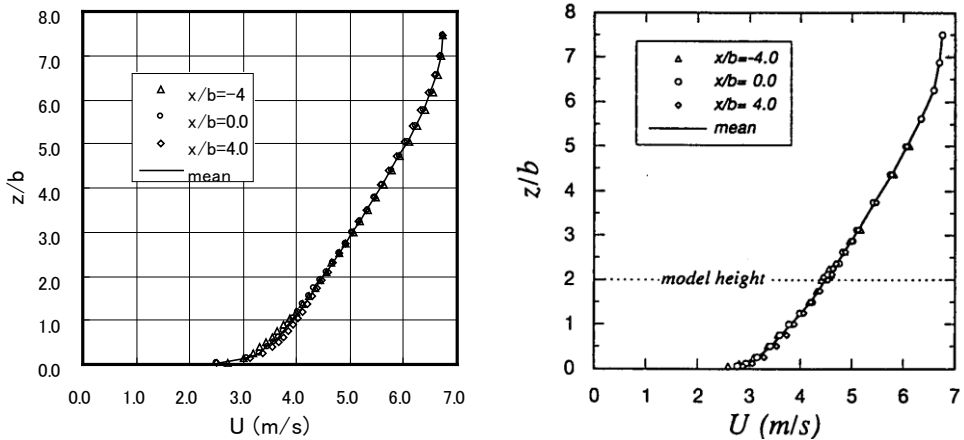


Figure 2-1-5. Vertical profile of $\langle u \rangle$

2.1.3 Calculation conditions for the benchmark test (basic calculation conditions)

The basic calculation conditions established for the benchmark test are listed in Table 2-1-2 and illustrated in Figures 2-1-6 and 2-1-7. However, the conditions were initially provisional. Before the benchmark tests were performed by each organization, preliminary calculations using the standard $k-\epsilon$ model described in the next section and a sensitivity study of the calculation conditions described in the subsequent section were performed to confirm that the basic calculation conditions were appropriate.

Table 2-1-2. Calculation conditions for benchmark use (basic calculation conditions)

Computational domain	$21b (x) \times 13.75b (y) \times 11.25b (z)$ which corresponds to the size of the wind tunnel
Grid discretization	$60 (x) \times 45 (y) \times 39 (z) = 105,300$ cells (Figure 2-1-6). The building was

	discretized into $9 \times 9 \times 15$ grids
Scheme for advection term	Quick scheme for $\langle u \rangle$ $\nu \times w \otimes k - \epsilon$
Building wall surface	Logarithmic law for smooth surface wall
Surface of wind tunnel side wall	Logarithmic law for smooth surface wall
Surface of wind tunnel ceiling	Logarithmic law for smooth surface wall
Surface of wind tunnel floor	Logarithmic law with roughness length ($z_0 = 1.8 \times 10^{-4}$ [m])
Inflow boundary condition	Interpolated value of U and k from the experimental approaching flow $\epsilon = C_\mu^{1/2} k \cdot \partial \langle u \rangle / \partial z$ ($\epsilon = P_k$) (Figure 2-1-7)
Outflow boundary condition	Zero-gradient condition

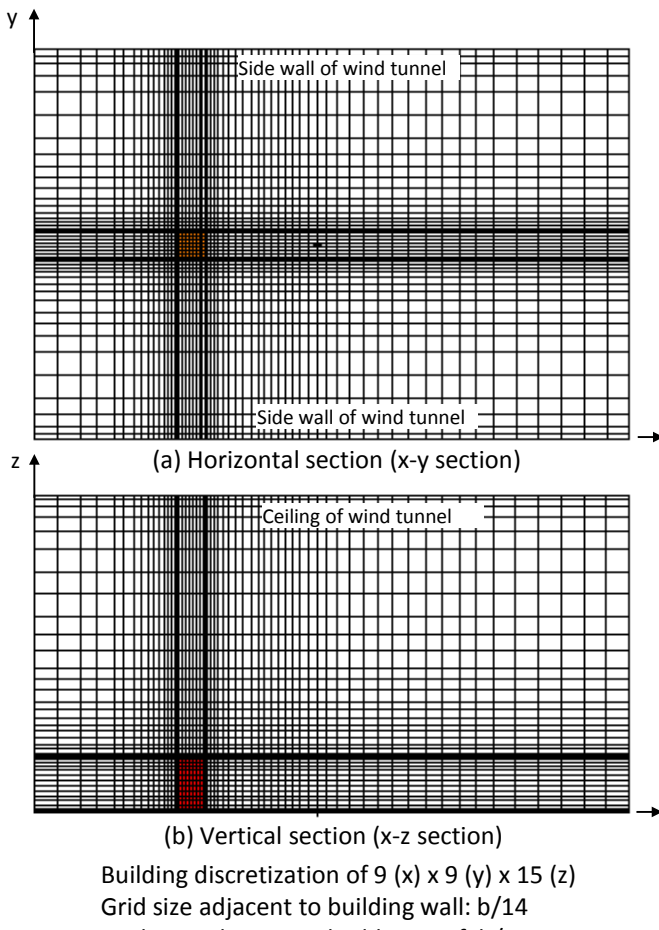


Figure 2-1-6. Computational domain and grid discretization

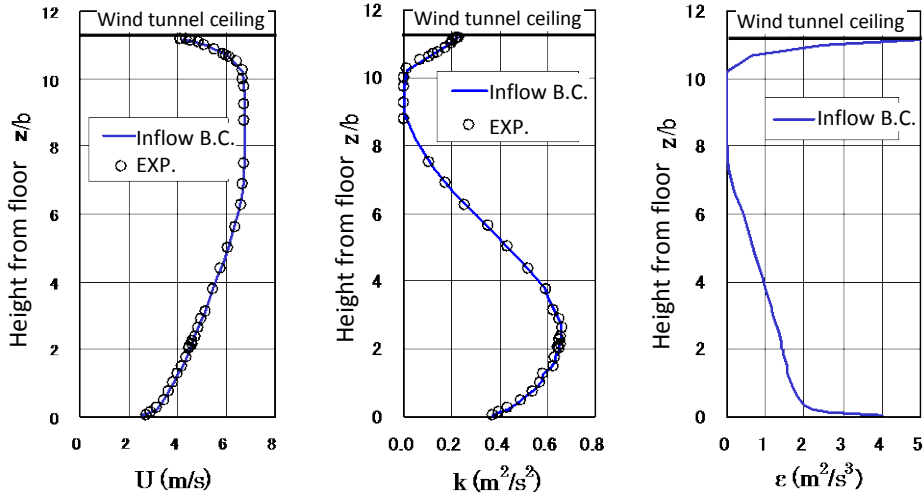


Figure 2-1-7. Inflow boundary conditions

2.1.4 Results of preliminary calculations based on standard $k-\varepsilon$ model and basic calculation conditions

Before the benchmark tests were conducted by each organization, preliminary calculations were performed using the standard $k-\varepsilon$ model and the basic calculation conditions. The distributions of the various quantities obtained are shown, and the prediction accuracy of the standard $k-\varepsilon$ model, which is widely used for practical calculations, is discussed.

2.1.4.1 Mean wind velocity distribution in vertical section

Figures 2-1-8 and 2-1-9 show the distributions of $\langle u \rangle$ and $\langle w \rangle$, respectively, in the vertical section of the center of the building. In these figures, the vertical dotted lines show the positions of each measurement line in the experiment, and the wind velocity values are plotted with these lines as the vertical axes. When a value is positive, it is plotted to the right of the measurement line, and when it is negative, it is plotted to the left.

In general, the calculated and experimental values agree well. However, close to the roof surface of the measurement line at $x/b = -0.25$ (the 3rd measurement line from the left), the experimental value of $\langle u \rangle$ is negative because of the reverse flow, although the calculation does not reproduce this negative value. Near the roof surface, the distributions of the predicted values of both $\langle u \rangle$ and $\langle w \rangle$ are more gradual than those of the experimental values. Below the measurement line at $x/b = 3.25$ (the 1st measurement line on the right), the value of the calculated $\langle u \rangle$ is lower than the experimental value.

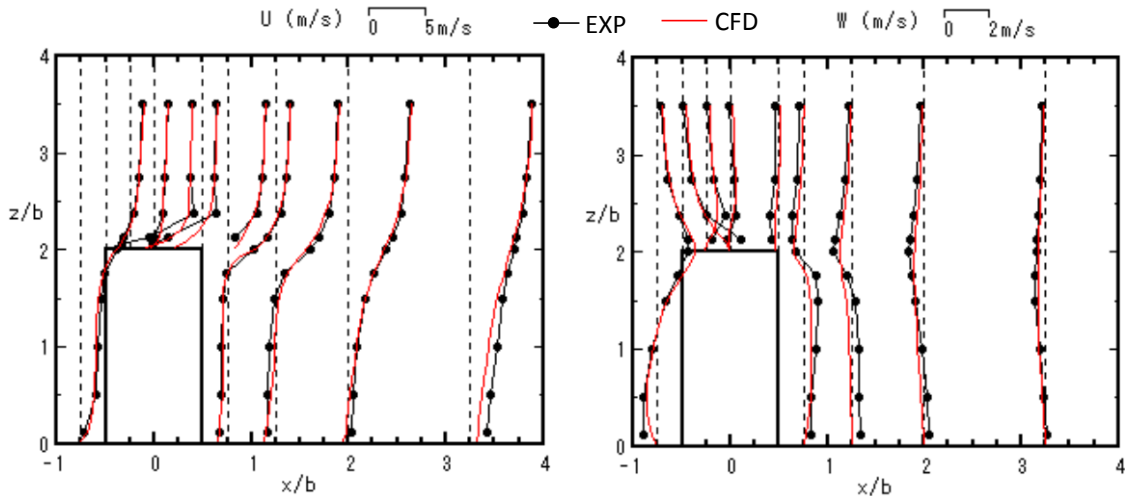


Figure 2-1-8. Distribution of $\langle u \rangle$ in vertical section in center of building ($y = 0$)

Figure 2-1-9. Distribution of $\langle w \rangle$ in vertical section in center of building ($y = 0$)

2.1.4.2 Average wind speed distribution in horizontal section

Figures 2-1-10 and 2-1-11 show the distributions of $\langle u \rangle$ and $\langle v \rangle$, respectively, in the plane near the ground surface ($z/b = 0.125$). The calculated and experimental values agree closely, other than the calculated value of $\langle u \rangle$ being lower than the experimental value in the wake region.

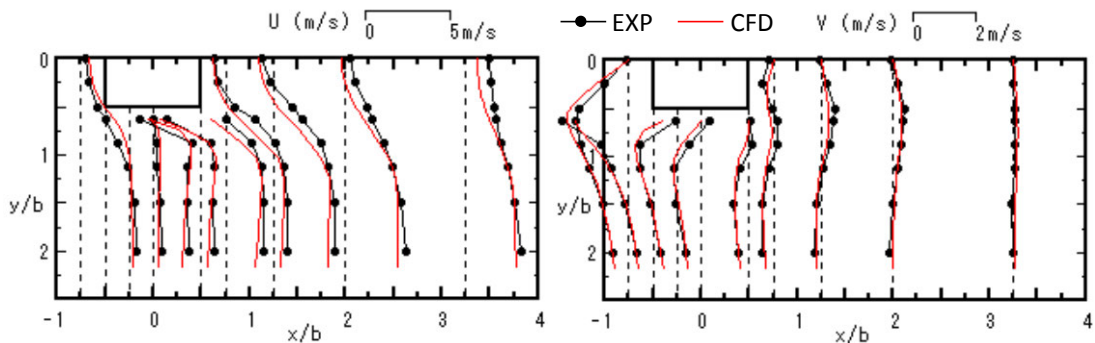


Figure 2-1-10. Distribution of $\langle u \rangle$ in horizontal section ($z/b = 0.125$)

Figure 2-1-11. Distribution of $\langle v \rangle$ in horizontal section ($z/b = 0.125$)

Figures 2-1-12 and 2-1-13 show the distributions of $\langle u \rangle$ and $\langle v \rangle$, respectively, in the plane of $z/b = 1.25$ (10/16 of the building height). In the calculation results, the distributions of both $\langle u \rangle$ and $\langle v \rangle$ near the building side surface are more gradual than in the higher section ($z/b = 0.125$), which does not correspond well with the experimental results. The reason for this is discussed later. In other regions, the calculation and experimental results are in good agreement.

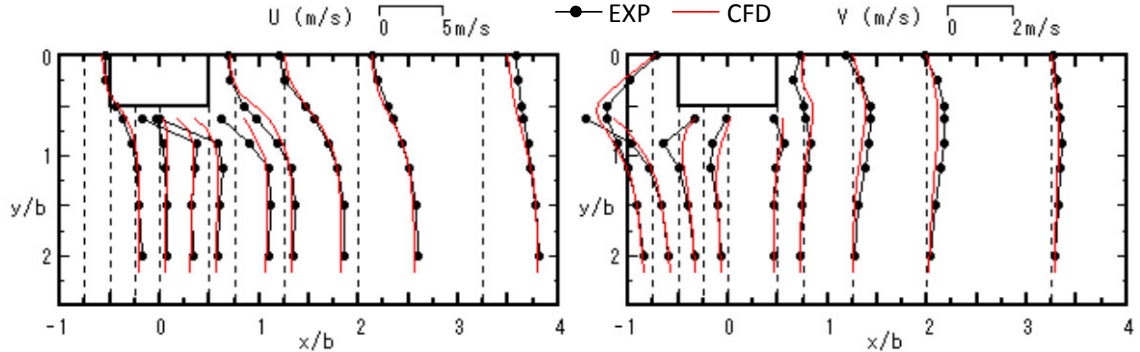


Figure 2-1-12. Distribution of $\langle u \rangle$ in horizontal section ($z/b = 1.25$)

Figure 2-1-13. Distribution of $\langle v \rangle$ in horizontal section ($z/b = 1.25$)

2.1.4.3 Distribution of turbulent kinetic energy k

Figures 2-1-14 to 2-1-16 show the distributions of the turbulent kinetic energy k in the planes of $z/b = 0.125$ and $z/b = 1.25$, respectively. As noted in previous studies, when using the standard $k-\varepsilon$ model, k is overestimated near the upwind sides of buildings and upwind corners of a roof. These tendencies are evident in the present calculation results. As a result, the turbulent diffusion was excessive, and the reverse flow on the roof was not reproduced. In addition, in the $z/b = 1.25$ plane, the velocity distribution near the side of the building was more gradual than in the experiment results. However, in the plane near the ground surface ($z/b = 0.125$), such an extreme overvaluation of k does not occur, and the steep velocity distribution near the side surface of the building is reproduced relatively well (Figures 2-1-10 and 2-1-11).

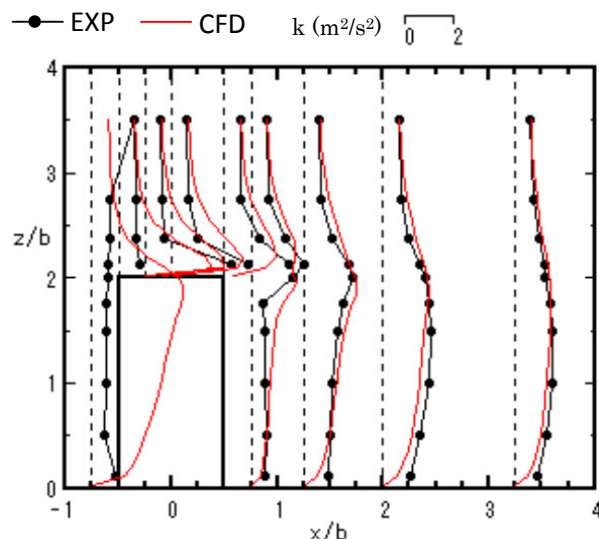


Figure 2-1-14. Distribution of k on vertical section at center of building

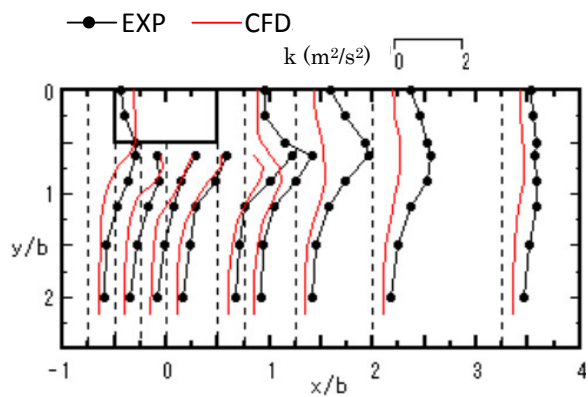


Figure 2-1-15. Distribution of k in horizontal section ($z/b = 0.125$)

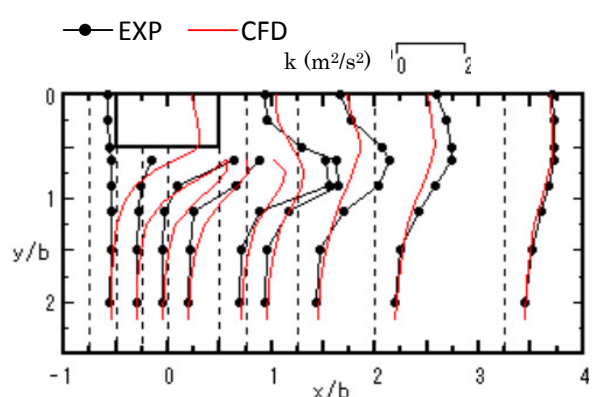


Figure 2-1-16. Distribution of k on horizontal section ($z/b = 1.25$)

2.1.4.4 Wind speed ratio

Figures 2-1-17 compares the calculated values of the wind speed ratio with the experimental values obtained by standardizing the scalar wind velocity near the ground surface ($z/b = 0.125$), based on the wind velocity at the same height without the building. For the area where the wind speed ratio is 1.0 or higher (which is important when evaluating gust wind around buildings), the ratio can be predicted with an accuracy of approximately $\pm 10\%$. However, in the low-velocity area in the wake of the building, the calculated wind speed ratios are lower than those measured in the experiment.

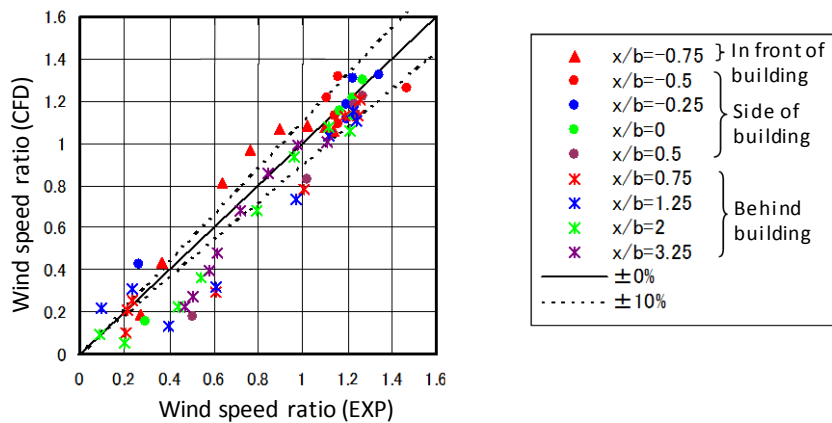


Figure 2-1-17. Wind speed ratio near ground surface

2.1.5 Impact of various calculation conditions on calculation results

The previous section described the results obtained for the basic calculation conditions. In this section, the calculation results obtained for various other calculation conditions were compared with those obtained for the basic calculation conditions. The calculation conditions were varied to investigate the suitability of the basic calculation conditions and to obtain information concerning the minimum size of the computational domain and the grid width criteria, which are needed to perform practical calculations, as well as the impact of the boundary conditions on the analysis results.

2.1.5.1 Size of computational domain

Figure 2-1-19 shows the results of the calculation for a case in which the basic domain ($21b \times 13.75b \times 11.25b$) was narrowed to form a small domain ($13.8b \times 7.56b \times 7.75b$), as shown in Figure 2-1-18, and when it was narrowed to form a very small domain ($11b \times 5.56b \times 4.35b$), as shown in Figure 2-1-19. In both cases, to conform to the calculation conditions for the upper and side surfaces, free inflow–outflow conditions were assumed (normal gradients of quantities were assumed to be 0), while the basic conditions were used for the other calculation conditions. Almost no difference was detected for the vertical section of the center of the building based on the size of the computational domain. For the narrower computational domain, on the horizontal section adjacent to the ground surface, the wind speed downwind from the side of the building tended to be a little lower, but the difference was small. In the region near the building distant from the outlet and side boundaries, even when the computational domain was narrowed to this degree, the impact was not

very large.

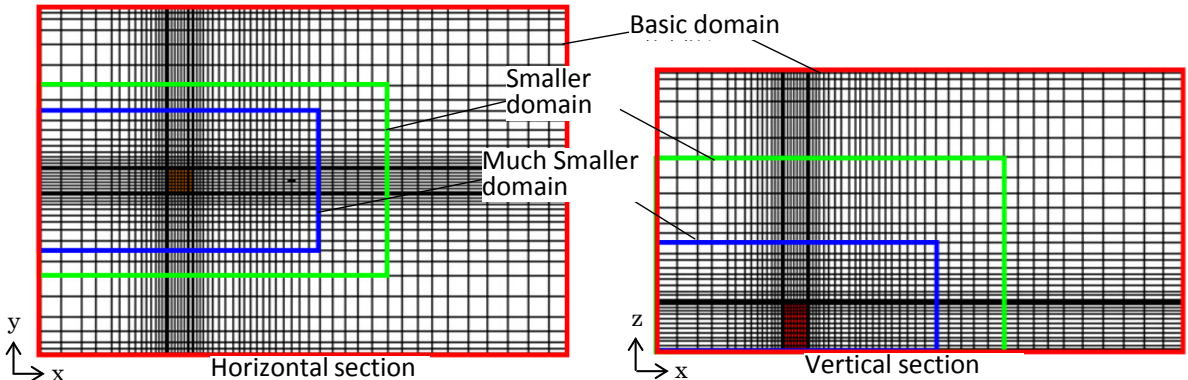


Figure 2-1-18. Computational domain

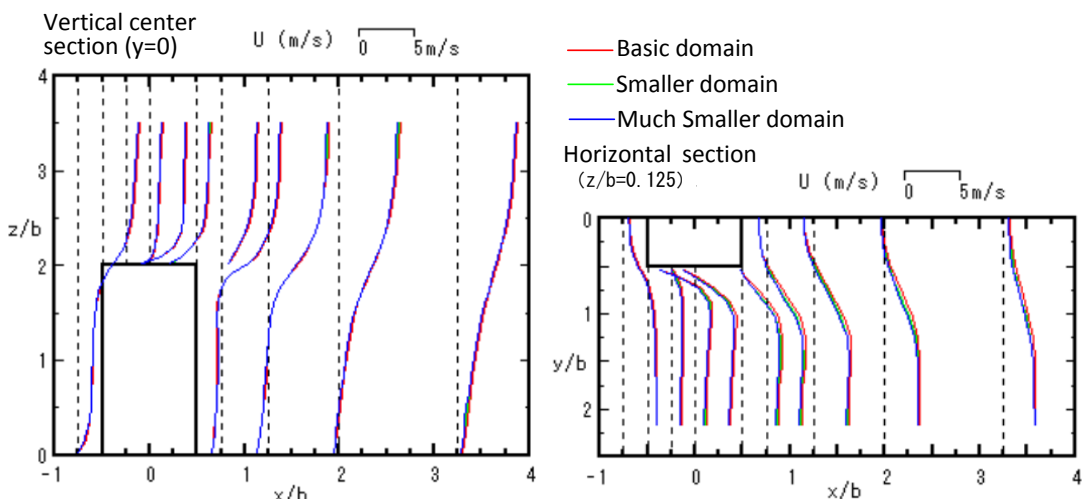


Figure 2-1-19. Impact of computational domain size on flow field around building (distribution of $\langle u \rangle$)

2.1.5.2 Grid resolution

To investigate the impact of the grid resolution, the calculations were performed for a finer grid with a resolution that was exactly 1/2 of the basic grid's resolution and a coarser grid with a width that was about double the basic grid. The basic conditions used were the same as for the other calculation conditions. The results are shown in Figure 2-1-20. The results for the basic and finer grids are almost identical, which indicates that the discretization of the basic grid is sufficient. The results for the coarser grid exhibited relatively large differences near the roof surface, but no large differences were observed near the ground surface. For reference, Figures 2-1-21 and 2-1-22 show the grid discretizations of the basic and coarser grids, respectively, near the building.

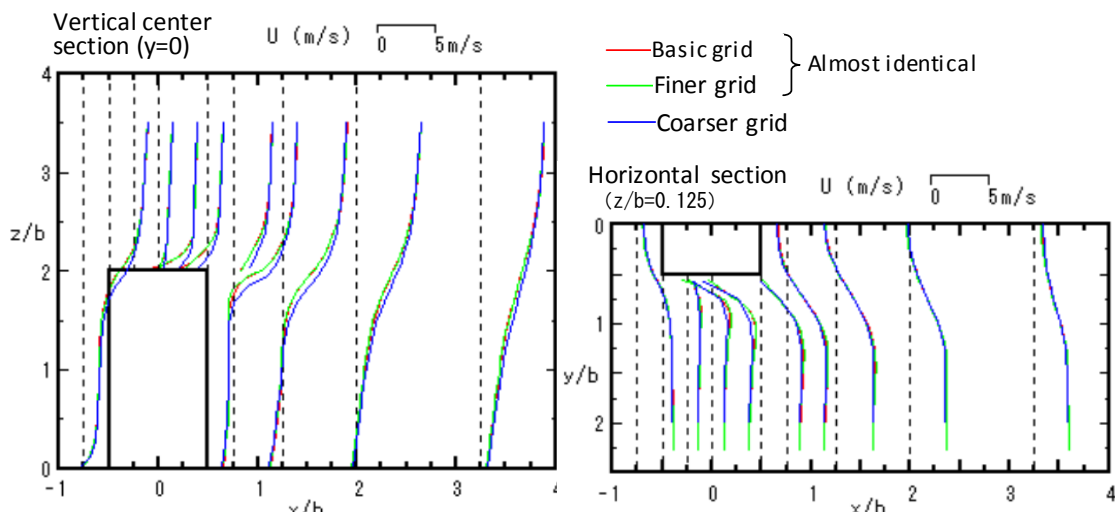


Figure 2-1-20. Impact of grid resolution on flow around building (distribution of $\langle u \rangle$)

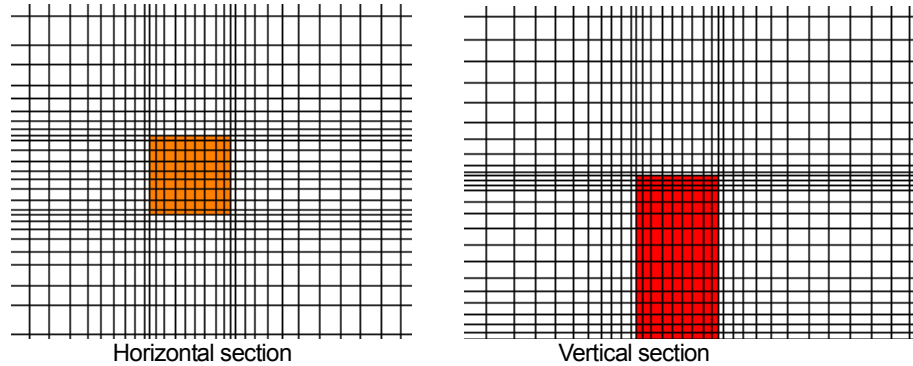


Figure 2-1-21. Basic grid

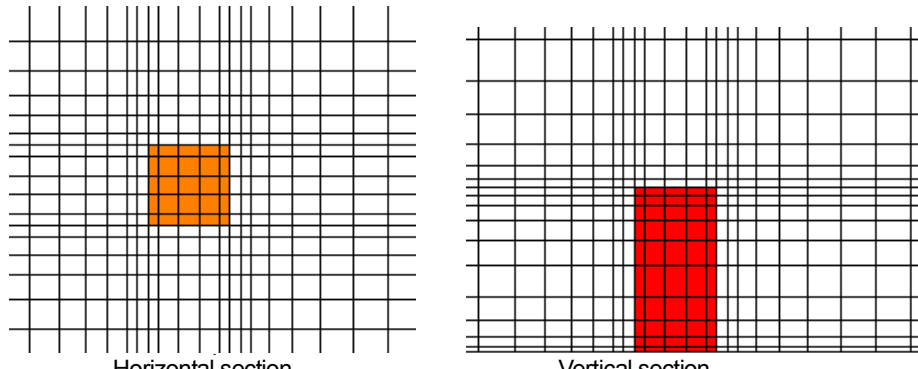


Figure 2-1-22. Coarser grid

2.1.5.3 Impact of inflow profile in upper space and upper/side surface boundary conditions

According to the basic conditions, the top and side surfaces of the computational domain were considered to be the wind tunnel walls (subject to the logarithmic law for smooth surfaces), and the velocity profile near the top surface at the inflow boundary was taken to be the velocity gradient given the effect of the wall surfaces (see Figure 2-1-7). Figure 2-1-23 shows the calculation results for $\langle u \rangle$ for a case in which these were set to be free

inflow-outflow (the normal gradients of the quantities were assumed to be 0) and zero-pressure boundaries, while the inflow profile above the height $z/b = 8$ was considered to be uniform (the values of $\langle u \rangle$, k , and ε above $z/b = 8$ were considered to be the same as at $z/b = 8$). The results for this case were almost identical to those obtained for the basic conditions. Therefore, when the computational domain is consistent with the basic conditions, the inflow profile of the upper region and the boundary conditions for the upper and side surfaces have almost no impact on the flow field around the building.

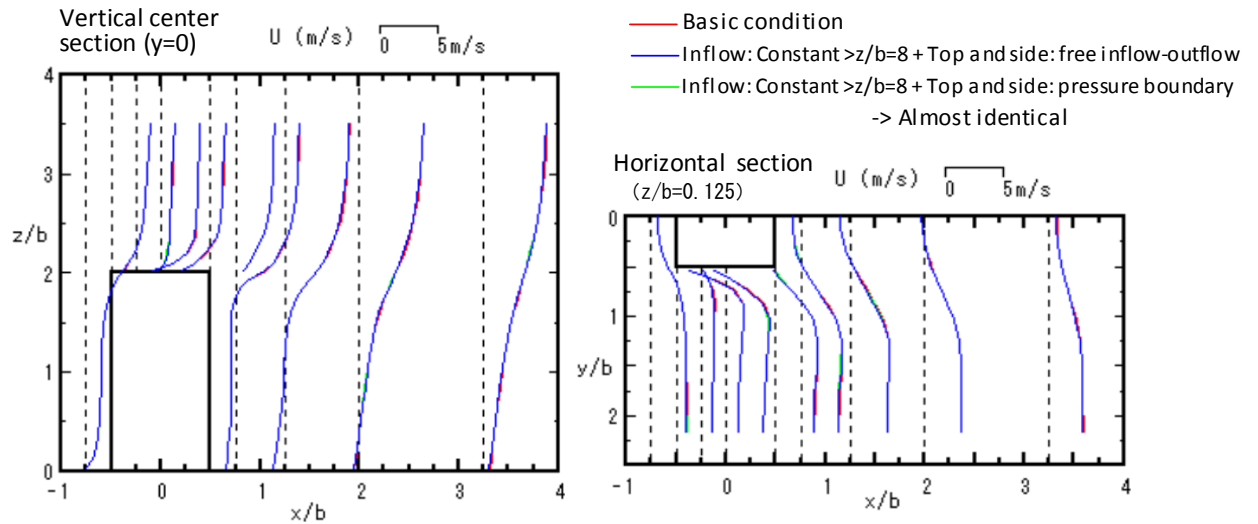


Figure 2-1-23. Impact of inflow profile of upper space and boundary conditions of the upper/side surfaces on flow field around building

2.1.5.4 k and ε of inflow

As mentioned previously, under the basic calculation conditions, the k values of the inflow are obtained by extrapolating from the experimental values, assuming that the production P_k and dissipation rate ε are balanced. The ε of the inflow is given by eq. (2.1.2).

In this case, considering that the value of $-\langle u'w' \rangle$ is usually unknown in practical calculations, ε is given by eq. (2.1.2). However, because $-\langle u'w' \rangle$ was measured in an experiment conducted by Meng and Hibi [1], the experimental value of $-\langle u'w' \rangle$ can be used to obtain ε from eq. (2.1.1). The influence of the inflow ε , which is given by equation (2.1.1), on the flow field around the building was investigated. Figure 2-1-24 shows the vertical distributions of ε according to eqs. (2.1.1) and (2.1.2).

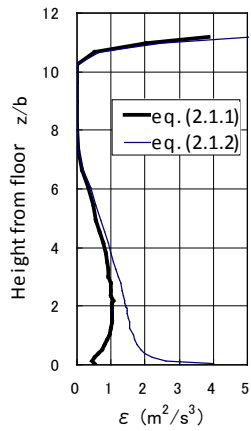


Figure 2-1-24. Vertical distributions of ε in inflow boundary conditions

The effect on the prediction results was also investigated for cases in which k and ε were given inappropriately (incorrectly). The inappropriate values of k and ε were $0.01 \text{ m}^2/\text{s}^2$ and $0.01 \text{ m}^2/\text{s}^3$, respectively, and these values were constant from bottom to top. In both cases, except for the inflow k and ε , the basic calculation conditions were used.

The results are shown in Figure 2-1-25. When ε is given by eq. (2-1-1), although the wind velocity in the wake region is slightly higher, the difference between the results obtained and those for the case of ε given by eq. (2-1-2) was small. Although the figure is omitted, even for an inflow ε given by eq. (2.1.1) using the measured $-\langle u'w' \rangle$, the ε distribution was changed to the vertical distribution given by eq. (2.1.2) after entering the computational domain. The reason for this is that the k - ε model hypothesizes the isotropy of the turbulence. Therefore, even when the inlet ε value is given by eq. (2.1.1) or eq. (2.1.2), there is little difference in the results obtained concerning the flow around the building. However, when the k and ε values are incorrect, the results vary greatly. Thus, it is important to use appropriate values for the inflow boundary. The AIJ guidelines [34] describe how the k and ε of the inflow boundary should be set for practical calculations.

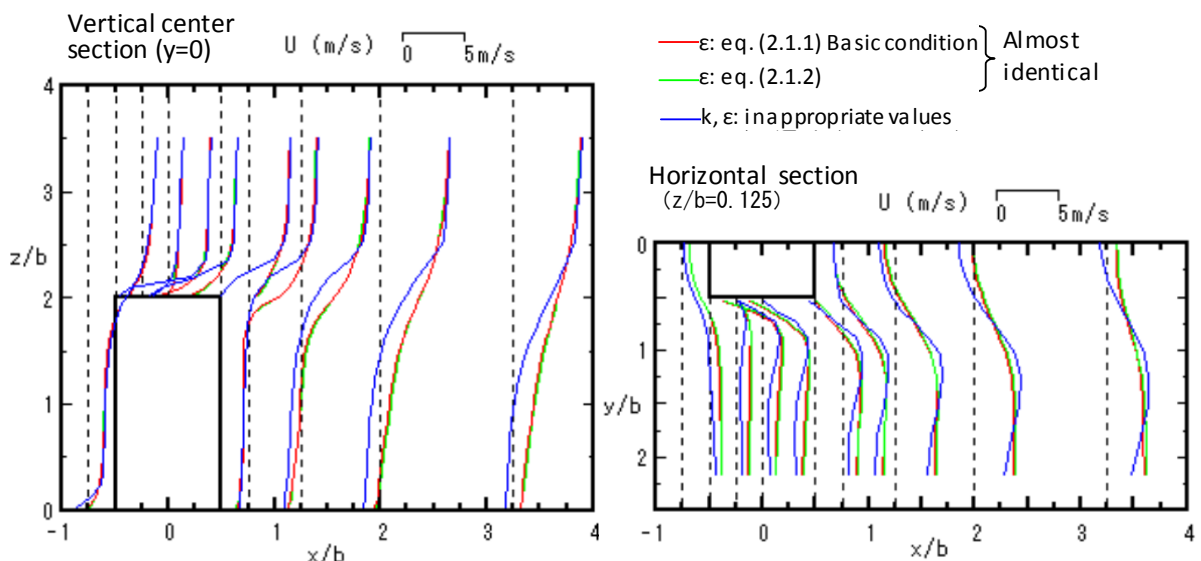


Figure 2-1-25. Effect of k and ε of inflow on flow field around building (distribution of $\langle u \rangle$)

2.1.5.5 Discretization scheme of advection term

Under the basic calculation conditions, the discretization scheme for the advection term is set to be the QUICK scheme for $\langle u \rangle$, $\langle v \rangle$, $\langle w \rangle$, k , and ε . Figure 2-1-26 shows the results for a case in which this is set to be the first-order upwind scheme for all variables. As noted by Patankar [9], in regions such as behind the building, where the wind blows diagonally toward computational cells, the results for the first-order upwind scheme have a less desirable blunt velocity distribution than the results obtained with the QUICK scheme, because of the impact of pseudo-diffusion.

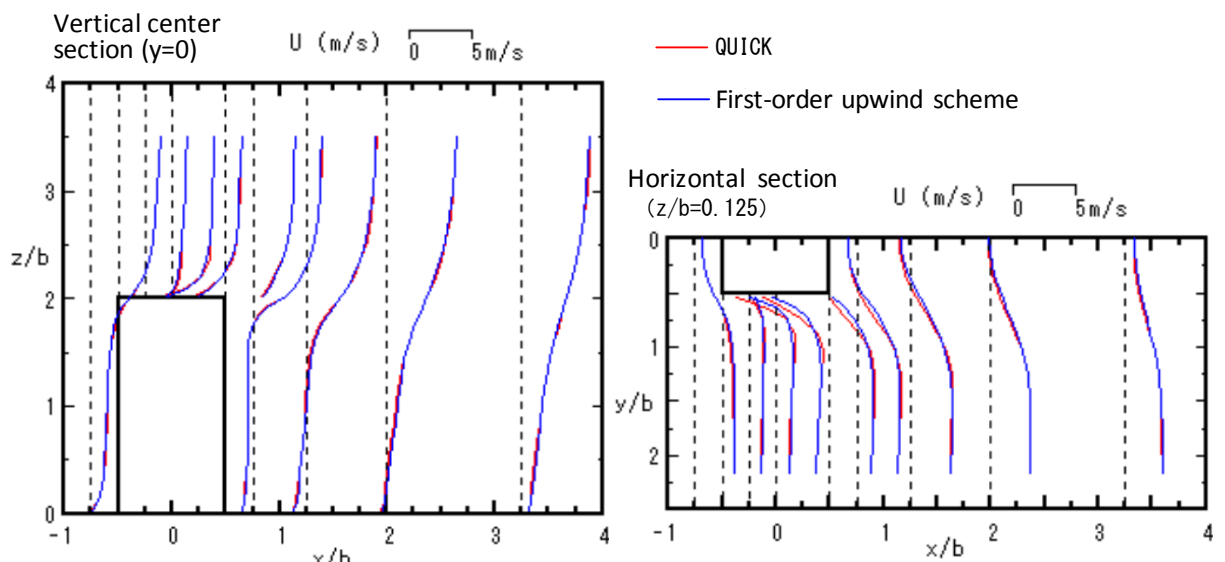


Figure 2-1-26. Impact of discretization scheme for advection term on flow field around building (distribution of $\langle u \rangle$)

2.1.5.6 Convergence conditions

In the calculations described in the previous section, it was assumed that the convergence criterion (STED represented by the following equation) was 10^{-6} , which is 100 times more strict than the default criterion (10^{-4}). It was confirmed that the solution did not change with a longer calculation time.

$$STED = \frac{\sum_{n=1}^N |\phi^{n+1} - \phi^n|}{(\phi_{\max} - \phi_{\min}) \times N} \quad (N: \text{all elements}) \quad (2.1.7)$$

Figure 2-1-27 compares the results obtained using the two convergence criteria (10^{-4} , the default value, and 10^{-6}). As the figure shows, there are small differences in the results in the wake region. This flow field is an example of a case for which there are no problems at the default value. However, when the calculation is stopped at the default value, attention should be paid to whether the convergence achieved is sufficient.

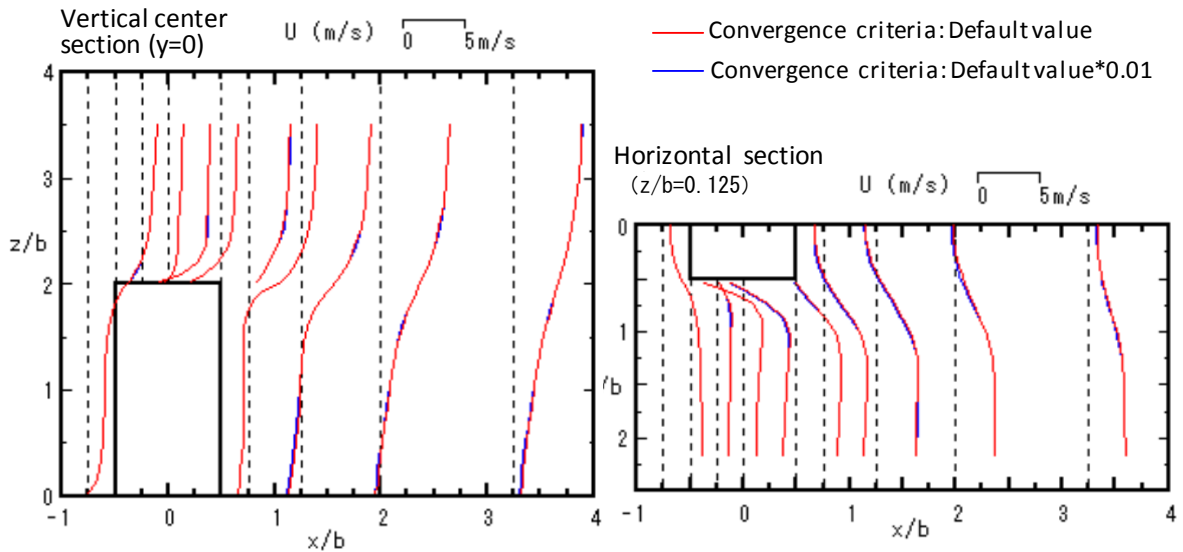


Figure 2-1-27. Case of varied convergence judgment conditions (distribution of $\langle u \rangle$)

2.1.6 Results of benchmark tests by different organizations—impact of turbulence model [39]

2.1.6.1 Calculation case table

Table 2-1-3 lists the calculation results submitted by different organizations. These calculations were mainly conducted using the $k-\epsilon$ models, including five types of modified $k-\epsilon$ models. The results obtained using the differential stress model (DSM) and large-eddy simulation (LES) with a third-order upwind scheme (see ref. [16]) are also included.

2.1.6.2 Comparison of reattachment lengths

Table 2-1-3 lists the reattachment lengths on the roofs and behind the building on the floor surfaces for all of the cases. As noted in previous research, the calculation results based on all of the standard $k-\epsilon$ models (KE1 to KE5) show no reverse flow on the roof surface, as observed in the experiment. In contrast, for the modified $k-\epsilon$ models, i.e., the modified $k-\epsilon$ model proposed by Launder and Kato (LK) [27] (LK1 to LK3), the modified $k-\epsilon$ model proposed by Murakami, Mochida and Kondo (MMK) [38] (MMK1 and MMK2), the modified $k-\epsilon$ model proposed by Durbin [26] (DBN), and the Re-Normalisation Group (RNG) $k-\epsilon$ models [24] (RNG1 and RNG2), the reverse flow on the roof was reproduced in all cases. However, the reattachment length X_R tended to be a little larger than that obtained in the experiment. With DSM, the reverse flow was strong, and the flow reattachment was not reproduced on the roof surface. In the LES case, the reverse flow was a little larger than that in the experiment. On the other hand, for all of the models, the reattachment lengths behind the building X_F were found to be higher than the experimental value, although there was a tendency for higher values to be obtained from the modified $k-\epsilon$ models than from the standard $k-\epsilon$ model.

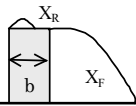


Table 2-1-3. Calculation cases and calculation conditions for a 2:1:1 building model

Organization	Software	Turbulence model	Scheme for convention terms	Computational method and time integral scheme	X_R/b	X_F/b	CASE
A	STREAM ver. 2.10	$k-\varepsilon$ (standard)	QUICK	SIMPLE, steady solution	—	2.00	KE1
		$k-\varepsilon$ (LK)			0.87	2.98	LK1
B	STAR-LT ver. 2.0	$k-\varepsilon$ (standard)	QUICK	SIMPLE, steady solution	—	2.20	KE2
C	Self-made	$k-\varepsilon$ (MMK)	QUICK	MAC with implicit scheme	0.65	2.72	MMK1
D	FLUENT ver. 5.0	$k-\varepsilon$ (standard)	Central	SIMPLE, steady solution	—	2.41	KE3
		$k-\varepsilon$ (RNG)			0.58	3.34	RNG
D	Self-made	$k-\varepsilon$ (standard)	QUICK	HSMAC, unsteady solution with implicit scheme	—	2.70	KE4
		$k-\varepsilon$ (LK)			0.58	3.19	LK2
		$k-\varepsilon$ (modified LK)			0.53	3.11	LK3
		$k-\varepsilon$ (MMK)			0.52	3.09	MMK2
		$k-\varepsilon$ (Durbin)			0.63	2.70	DBN
		DSM			>1.0	4.22	DSM
E	Self-made	$k-\varepsilon$ (standard)	QUICK	HSMAC, unsteady solution with implicit scheme	—	1.98	KE5
F	Self-made	LES	3 rd -order upwind scheme	Artificial compressibility method, explicit	0.92	2.05	LES
Experiment [1]					0.52	1.42	

2.1.6.3 Distribution of k near windward corners of building

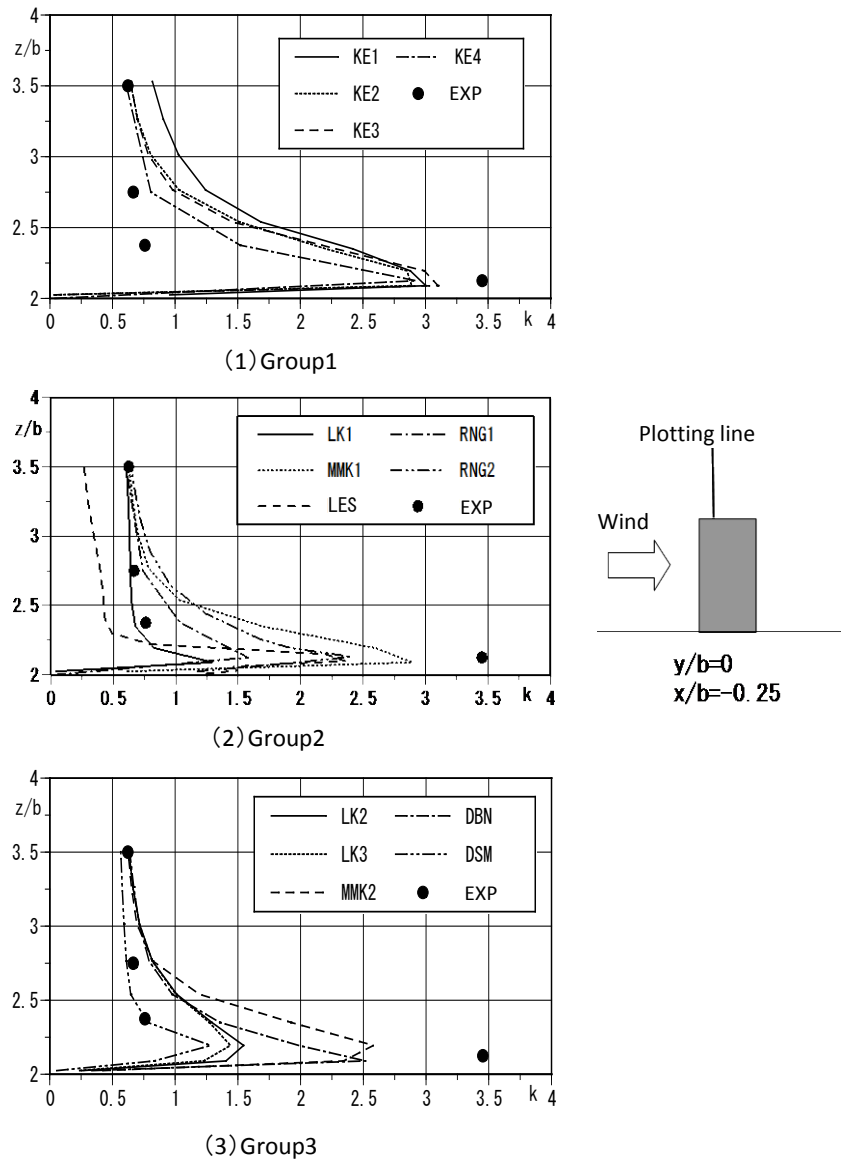
The computational cases were categorized in the following three groups, based on the CFD code and turbulence model used.

Group 1: KE1, KE2, KE3, KE4, and KE5 (standard $k-\varepsilon$)

Group 2: LK1, MMK1, LES, and RNG (modified $k-\varepsilon$ and LES)

Group 3: LK2, LK3, MMK2, DBN, and DSM (modified $k-\varepsilon$ and DSM using CFD code of organization D)

Figure 2-1-28 shows the vertical distribution of k above the roof surface at $x/b = -0.25$. As noted in previous studies, the standard $k-\varepsilon$ model causes an overestimation of k and excessive turbulent diffusion at the windward corners of a building. Thus, in the results for all of the standard $k-\varepsilon$ models (Group 1), the values of k in the region of $z/b > 2.5$ are larger than for the results of the modified $k-\varepsilon$ models and other models (Groups 2 and 3). As a result of this overestimation of k , the reverse flow on the roof surface is not reproduced by the standard $k-\varepsilon$ model. However, a comparison with the experimental values at a height of $z/b = 2.125$ shows that the modified $k-\varepsilon$ models and other models tend to produce slightly lower k values than those obtained in the experiment. This results in the reverse flow region on the roof being a little larger than suggested by the $k-\varepsilon$ model, as previously mentioned. This tendency is more obvious with DSM in Group 3. This difference in k on the roof surface also influences the k distribution in the reverse flow and the reattachment length behind the building.

Figure 2-1-28. Distribution of k on building roof surface ($x/b = -0.25$)

2.1.6.4 Vertical distribution of $\langle u \rangle$ in the wake of the building

Figure 2-1-29 shows the vertical distribution of the streamwise velocity $\langle u \rangle$ at $x/b = 2.0$ in the wake of the building. Above the building height ($z/b = 2.0$), almost all of the predicted results agree well with the experimental values. However, close to the ground surface ($z/b < 1.0$), the differences in the reattachment length behind the building, X_F , between the cases for the above-mentioned differences are large. The velocity in the reverse-flow region exhibited larger negative values for the modified $k-\varepsilon$ and other models (Groups 2 and 3) than for the standard $k-\varepsilon$ model (Group 1). The velocity distribution in this region was most accurately reproduced by LES in Group 2.

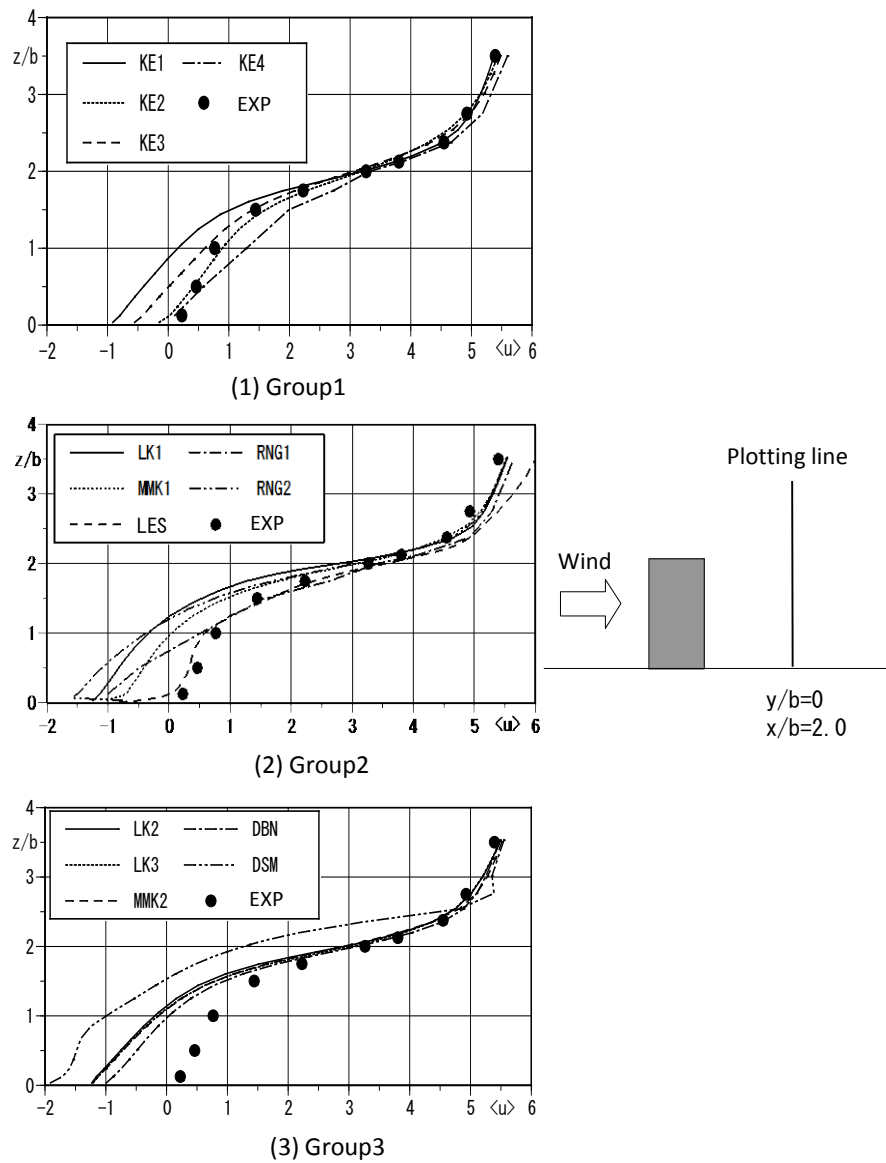


Figure 2-1-29. Distribution of streamwise velocity $\langle u \rangle$ behind building ($x/b = 2.0$)

2.1.6.5 Distribution of wind speed ratio near ground surface

Figure 2-1-30 shows the scalar velocity near the ground surface, normalized by the inflow velocity at the same height (2.75 m/s) as the wind speed ratio. Focusing on the form of the strong wind region near the building corners, the results for all cases are similar, but in a few cases, the distributions differ. Comparing the standard $k-\epsilon$ and modified $k-\epsilon$ models with the same CFD codes (for example, KE1 and LK1, KE4 and LK2, or LK2, MMK2, and DBN), the area within which the value is greater than 1.2 in the modified $k-\epsilon$ cases is a little wider behind the building and closer to the experimental results than in the standard $k-\epsilon$ model cases. In the DSM results, this area is extremely wide. Although the LES results exhibit a slight lack of symmetry because the averaging time was not sufficient, the area within which the value is greater than 1.2 agrees very well with the results of the experiment. In the region behind the building, the contour line for all RANS models extends downstream and differs greatly from the experimental results, but in the LES case, the experimental results are reproduced well.

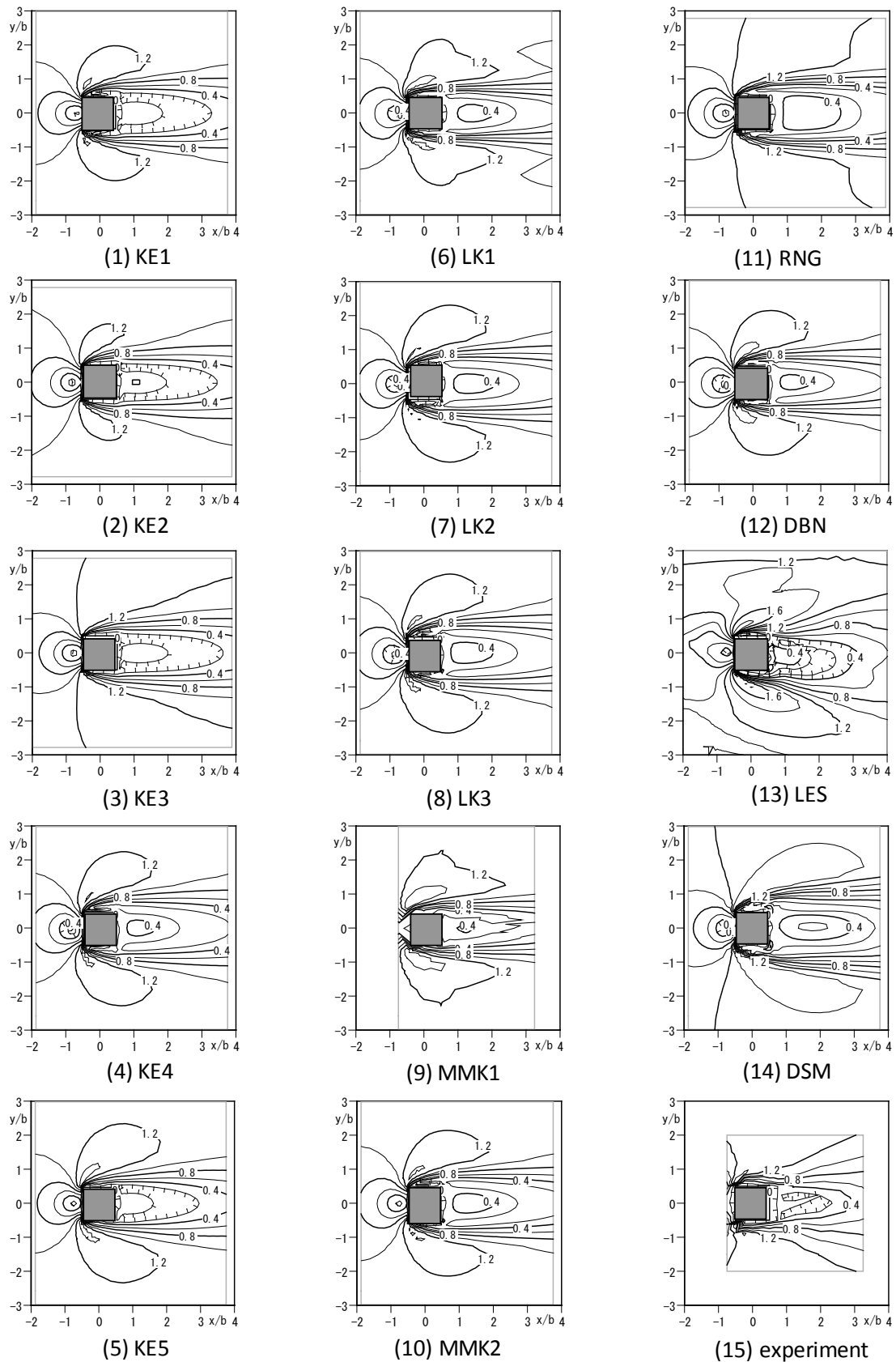


Figure 2-1-30. Comparison of wind speed increase ratios near ground surface ($z/b = 0.125$)

2.1.7 Impact of grid system

CFD calculations were performed using the unstructured grid system for the 2:1:1 building model analyzed in the previous section, and the results of the calculations were compared with the calculation results obtained using a structured grid system (basic conditions) and the experiment results. Conditions such as the computational domain, geometry and locations of the building, boundary conditions, and turbulence models were the same.

The grid was formed by tetrahedral elements automatically generated by software, and the grid density near the building was set to be continuously high. In general, when tetrahedral elements are used, if elements with sides parallel to the model surface (boundary layer elements) are placed on the boundary of a solid wall, the accuracy is improved. As shown in Figure 2-1-31, if the surface grids of the body are triangular, the boundary layer elements are triangular (prism elements).

Using the tetrahedral element density and boundary layer element density near the building as parameters, calculations were performed for the four cases listed in Table 2-1-4. The CFD code SCRYU/tetra for Windows ver. 5 from Software Cradle was used. Because its solver is based on the node-centered method, the number of control volumes was equal to the number of nodes. Figures 2-1-32 to 2-1-35 show the surface grids and the volume grid section around the building in each case.

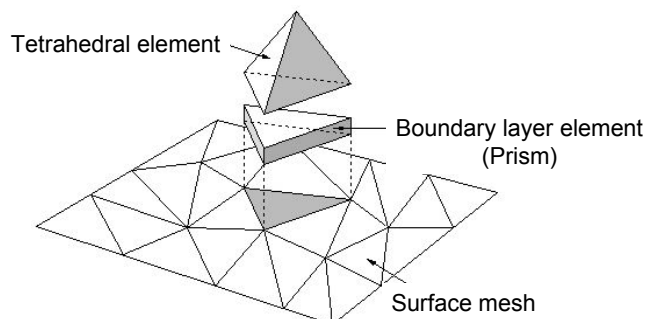


Figure 2-1-31. Boundary layer elements

Table 2-1-4. Calculation cases

		Boundary layer element (prism)	
Principal element (tetrahedral)	Width b is divided by 8 elements	One layer (identical with the first cell in the basic structured grid)	Two layers (half of the first cell in the basic structured grid)
		Case: T1P1 Elements: 136,052 Nodes: 26,611	Case: T1P2 Elements: 141,261 Nodes: 29,258
	Width b is divided by 16 elements	Case: T2P1 Elements: 358,086 Nodes: 69,286	Case: T2P2 Elements: 371,826 Nodes: 75,991

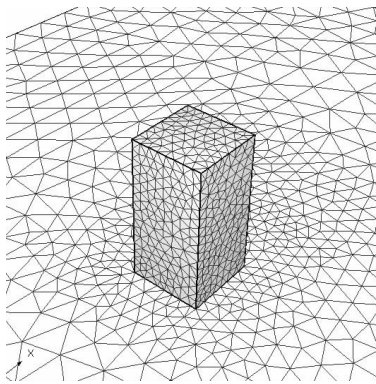


Figure 2-1-32. Surface grid (T1P1/ T1P2)

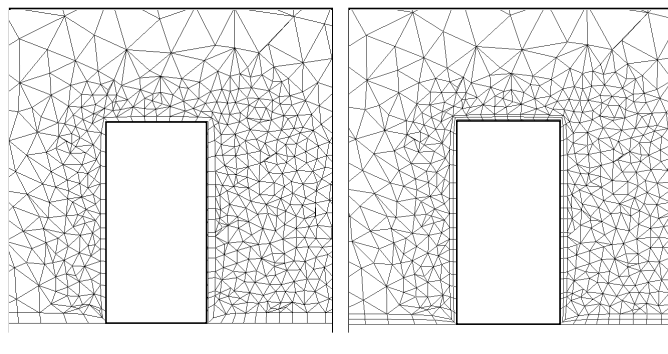


Figure 2-1-33. Volume grid sections

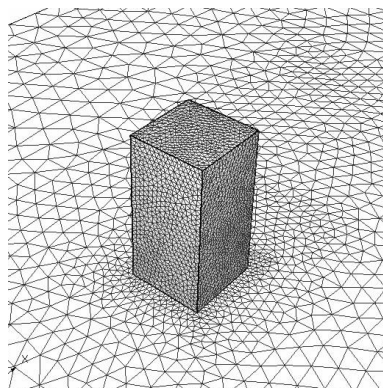


Figure 2-1-34. Surface grid (T1P1/ T1P2)

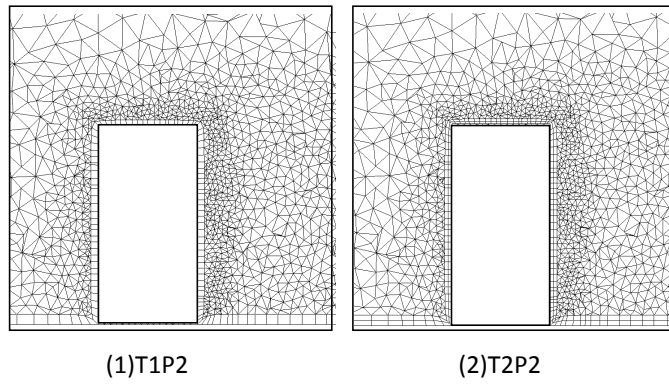
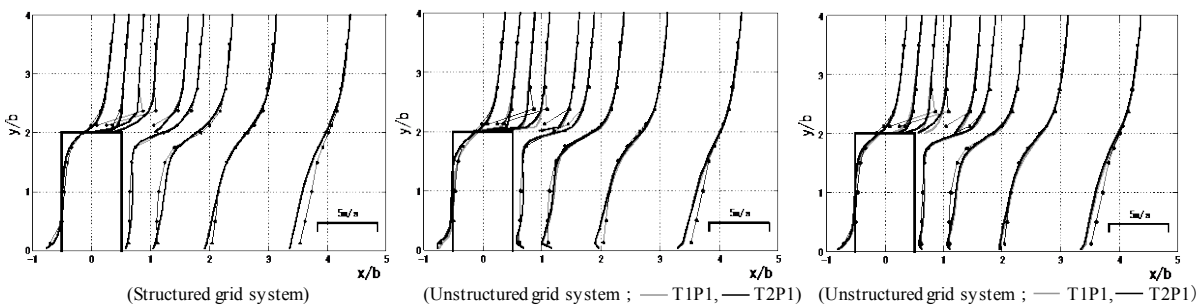


Figure 2-1-35. Volume grid sections

Figures 2-1-36 to 2-1-38 show the calculation results. Each figure shows the distribution of the streamwise velocity (the x-direction component), and ● indicates the experimental results. Overall, the accuracy obtained was similar to that obtained with the structured grid system. A comparison with the calculation results obtained using the unstructured grid system shows slight differences depending on the tetrahedral element density. The reverse flow region for the case in which thin prisms were formed in two layers corresponds a little more closely to the experimental results. Therefore, the boundary layer elements are confirmed to be effective. Because the boundary layer elements were inserted into the surface grid, the overall number of elements does not increase excessively. Accordingly, it is possible to improve the accuracy effectively by placing the boundary layer elements appropriately.

Figure 2-1-36. Vertical distribution of $\langle u \rangle$ ($y/b = 0$)

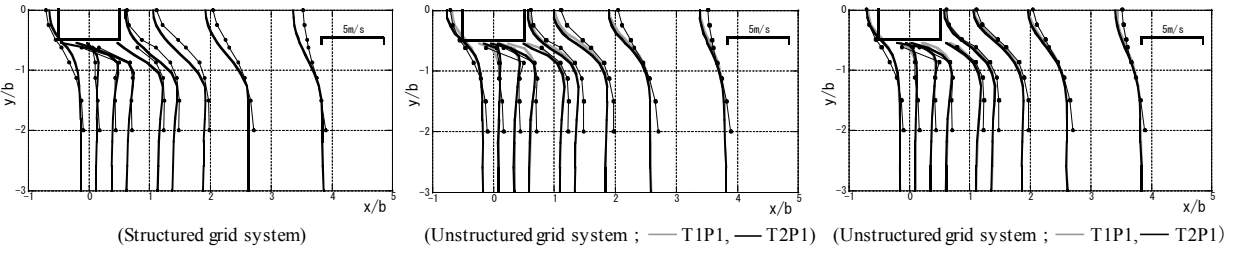


Figure 2-1-37. Horizontal distribution of $\langle u \rangle$ ($z/b = 1.25$)

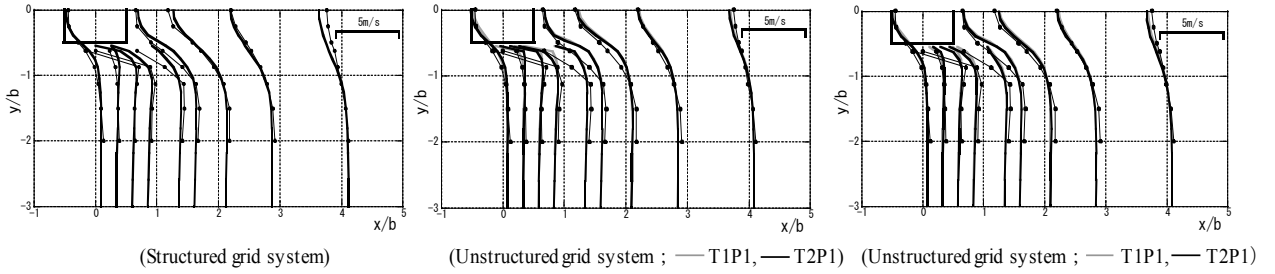


Figure 2-1-38. Horizontal distribution of $\langle u \rangle$ ($z/b = 0.125$)

2.2 Flow around a high-rise building with a 2:1:1 shape (LES)

2.2.1 Impact of inflow turbulence [40]

2.2.1.1 Introduction

In section 2-1-6, the flow around a high-rise building model placed in a boundary layer flow was analyzed using various modified $k-\epsilon$ models, and the results were compared with experiment results to assess the accuracy of the predictions obtained. The modified $k-\epsilon$ models were found to improve the prediction accuracy of the separation flow on the roof far more than the standard $k-\epsilon$ model, but all of the modified $k-\epsilon$ models tended to predict greater recirculation flow behind the building than the standard $k-\epsilon$ model. Among the modified $k-\epsilon$ models that were compared, the modified $k-\epsilon$ model proposed by Durbin [26] was found to produce results that most accurately reproduced the experimental results. This improvement was mainly achieved by Durbin's $k-\epsilon$ model by preventing overestimation of the recirculation flow behind the building more effectively than the other modified $k-\epsilon$ models and more accurately reproducing the separation flow and distribution of k at the windward corners.

On the other hand, in previous research on the flow around a cube and around a two-dimensional square cylinder, LES was clearly shown to produce more precise predictions than the $k-\epsilon$ models, DSM, and other RANS models [10-12]. However, LES requires that a physically appropriate velocity fluctuation be prepared and applied to the inflow boundary, and this requirement remains a challenge to the achievement of a practical calculation method.

This section describes how the LES method, which sets a driver region in the upstream region of the computational domain to generate inflow turbulence, was applied to flow around a 1:1:2 high-rise building model to study the reproduction of the periodic fluctuation and reattachment length behind the building by means of a comparison with experimental results and results obtained using the Durbin $k-\epsilon$ model.

2.2.1.2 Outline of numerical calculation

a) Target flow field

The target is the flow around a building with a 2:1:1 (height: width: depth) shape in the turbulent boundary layer,

described in Ref. [1] and illustrated in Figure 2-2-1.

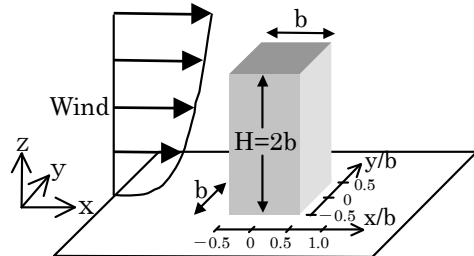


Figure 2-2-1. Outline of flow field

b) Calculation cases

Two LES calculations were conducted for the case without inflow turbulence (hereinafter referred to as LES (case 1)) and the case with inflow turbulence (hereinafter, LES (case 2)). The results obtained with Durbin's modified $k-\epsilon$ model, which achieved better agreement with the experimental results than the other RANS models, are also presented as shown in section 2.1.6.

c) Outline of calculation

- SGS model

The LES calculations were performed using the standard Smagorinsky model, with a value of 0.12 assigned to the Smagorinsky constant C_S [10].

- Computational domain

In the streamwise direction (x), the domain had a length of $10.5b$ upstream of the building ($5b$ of which is the driver part) and $15b$ downstream (Figure 2-2-2). The height (z) and width (y) were the same as for the measurement section of the wind tunnel used for the experiment ($13.75b$ (y) $\times 11.25b$ (z)).

- Grid discretization

The grid discretization was 70 (x) $\times 45$ (y) $\times 39$ (z). The smallest grid width was $0.07b$. The wall coordinates of the velocity definition point closest to the solid boundary were approximately 20 on the floor near the inflow boundary and approximately 35 on the building roof (Figure 2-2-2). Outside the driver region, the computational domain and grid discretization were identical to the computational domain of the basic conditions for the RANS model.

- Inflow boundary

The streamwise velocity $\langle u \rangle$ was obtained by extrapolation from the wind tunnel experimental values [1] (Figure 2-2-3). The inflow turbulence in LES (case 2) was generated by the method proposed by Kataoka et al. [16], which is a partial simplification of the method proposed by Lund et al. [15]. The size of the driver section used to generate the inflow turbulence is shown in Figure 2-2-2. Figure 2-2-3 shows the properties of the inflow turbulence obtained as a result. The properties of the approaching flow in the experiment were generally well reproduced.

- Ground and building wall surfaces, side surface, and upper surface boundaries

The two-layer (linear, 1/7 power law-type) model proposed by Werner and Wengle was used [13, 14, 17].

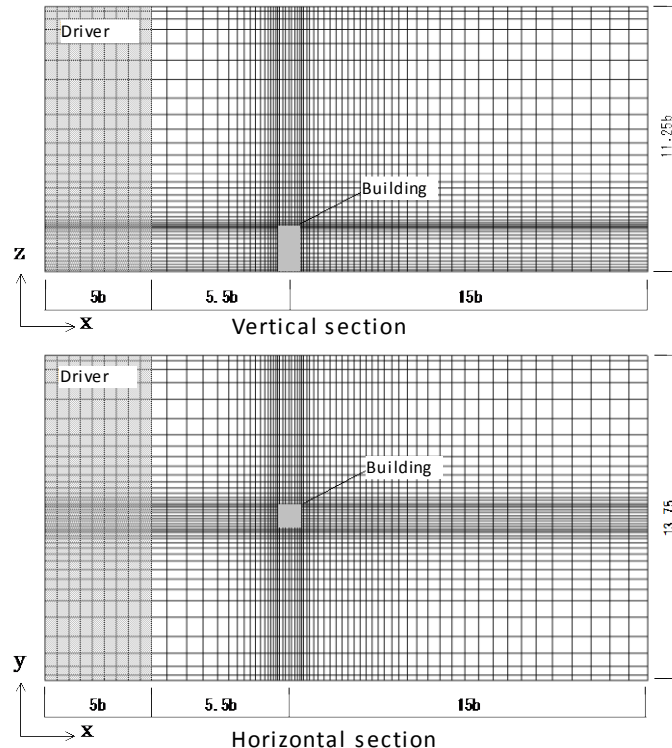


Figure 2-2-2. Computational domain and grid discretization

- Outflow boundary

The normal gradient was assumed to be zero for all quantities.

- Discretization scheme

The second-order central difference was used for the advection term. The second-order Adams–Bashforth scheme was used for the advection term, and the Crank–Nicolson scheme was used for the diffusion term.

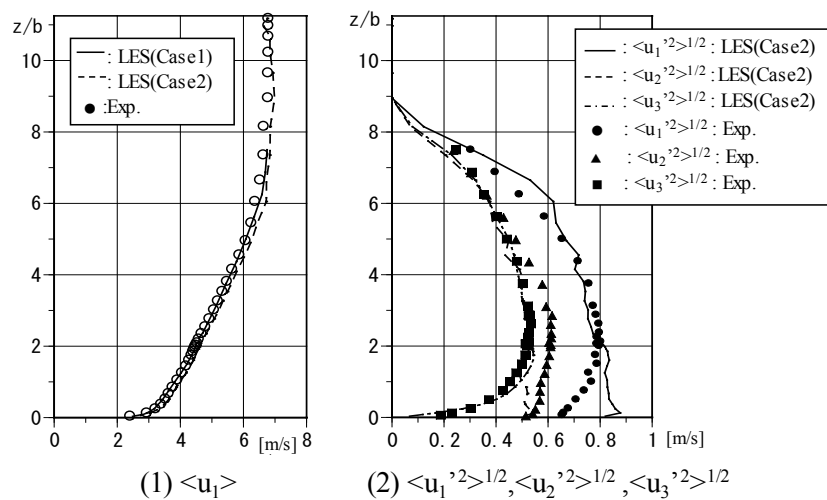


Figure 2-2-3. Inflow profiles obtained by computations at driver region in LES

- Averaged time

In both case 1 and case 2, the calculations were performed for approximately 500 dimensionless time units ($t \times$

U_H/b). The results shown below are the results obtained by averaging over 225 dimensionless time units (20 cycles of vortex shedding occurring behind the building in LES (case 1).

2.2.1.3 Results and considerations

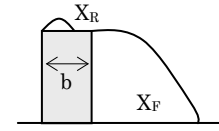
a) Reattachment distance of roof and back floor surface (Table 2-2-1)

Table 2-2-1 lists the reattachment lengths on the roof and behind the building. These reattachment lengths were calculated by linear extrapolation to obtain the reversal point of the sign of the streamwise velocity adjacent to the solid surface. LES (case 2) accurately reproduced the reattachment length on the roof (X_R), but LES (case 1), in which the inflow turbulence was not used, the estimated X_R was slightly higher than the experimental value, as in the case of the Durbin $k-\varepsilon$ model. On the other hand, the LES (case 2) results, obtained using the inflow turbulence, were very similar to those of the experiment.

In LES case 1, the reattachment length behind the building (X_F) was estimated to be smaller than that determined in the experiment, whereas in LES (case 2), it was larger. This difference greatly depends on whether the inflow turbulence was considered. However, judging based on the velocity distribution in the wake region, as shown in Figures 2-2-4 and 2-2-5, the properties of the recirculating flow behind the building determined for LES (case 2) were much closer to those determined in the experiment. In addition, in the two LES cases, the reattachment length behind the building was estimated to be much shorter than in the Durbin $k-\varepsilon$ case and approached to the experiment results.

Table 2-2-1. Reattachment distance of roof surface and wake of building

	x_R/b	x_F/b
Experiment	0.52	1.42
LES (Case 1: without inflow turbulence)	0.62	1.02
LES (Case 2: with inflow turbulence)	0.50	2.10
$k-\varepsilon$ (Durbin)	0.63	2.70



b) Comparison of wind speed distributions

- Wind speed vectors on vertical section (Figure 2-2-4)

Figure 2-2-4 shows the velocity vectors of the vertical section at the center of the building. The results for LES (case 1) show that the center of the recirculating flow behind the building is close to the back surface of the building and that the vortex is vertically lengthened. Therefore, its distribution differs from that determined in the experiment. In contrast, LES (case 2) accurately reproduces the width of the recirculation flow region and the location of the center of the vortex.

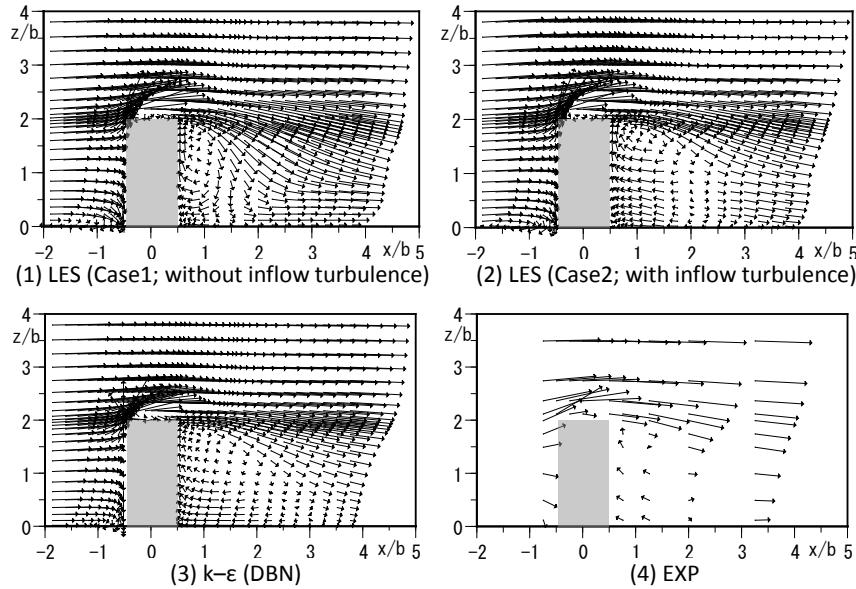


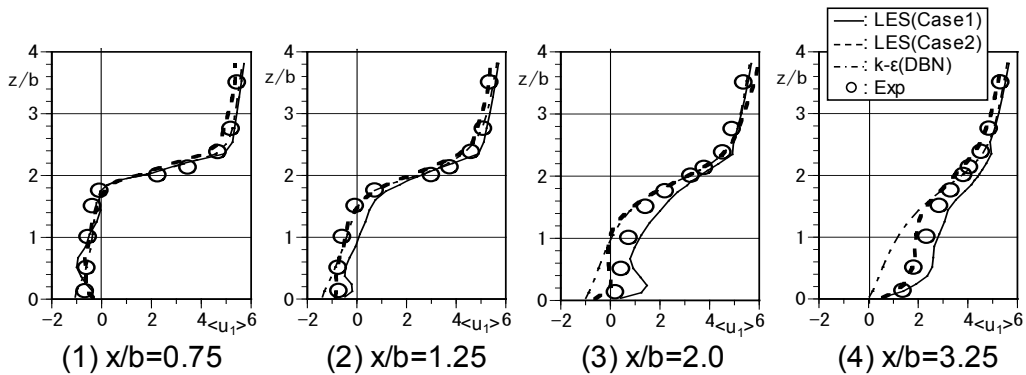
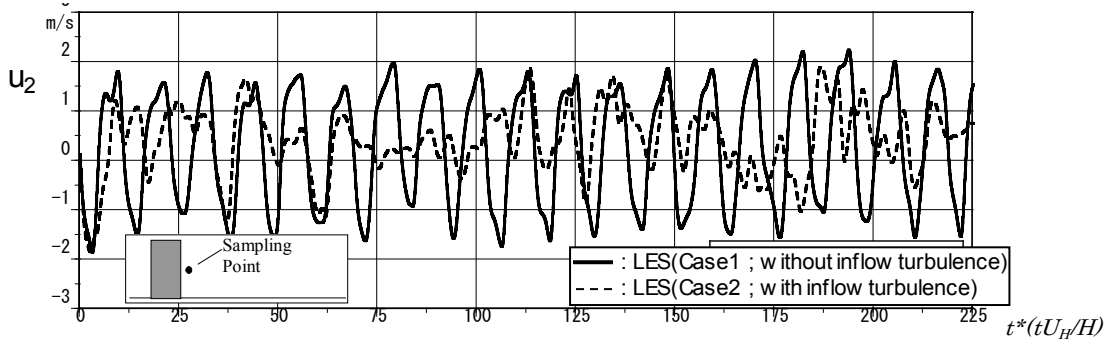
Figure 2-2-4. Distribution of time-average wind speed vector (vertical section at center of building)

- Vertical distribution of $\langle u \rangle$ in the wake of the building (Figure 2-2-5)

Figure 2-2-5 shows the vertical distribution of streamwise velocity $\langle u \rangle$ behind the building. On the line relatively close to the building ($x/b = 0.75$), all the computation results conform well to those of the experiment. However, for LES (case 1), in which the inflow turbulence was not given, the reverse flow behind the building is underestimated on the $x/b = 1.25$ and 2.0 lines. On the other hand, for LES (case 2), in which the inflow turbulence was given, the reverse flow behind the building agrees well overall with that determined in the experiment. The Durbin $k-\epsilon$ model overestimates the reverse flow region. Thus, on the $x/b = 2.0$ line, the absolute value of the velocity near the ground surface is overestimated.

- Velocity fluctuation behind the building (Figure 2-2-6)

Figure 2-2-6 shows the time history of the lateral velocity component v' inside the recirculation flow region behind the building ($x/b = 0.75, z/b = 1.0$). The location at which the velocity fluctuation was sampled is also shown in the figure. For LES (case 1), Karman vortex-type periodic fluctuations are clearly observed, with approximately 11 in the dimensionless cycle ($t \times U_H/b$). For LES (case 2), although periodic fluctuation is tentatively observed, the peak is small, and the wave form is not very clear. In other words, in LES (case 1), in which the inflow turbulence was not given to the approaching flow, the periodic fluctuation due to vortex shedding appears more strongly. As a result, the momentum transfer in the lateral direction in the recirculating flow behind the building is overestimated, and the development of the recirculation flow in the streamwise direction is suppressed in LES (case 1). Thus, the distribution properties are different from those of the experiment, as shown in Figures 2-2-4 and 2-2-5. Although velocity fluctuation measurement results are not provided in Refs. [1] and [2], judging from the comparison of the velocity distributions, it is assumed that the velocity fluctuation in LES (case 2) is similar to that in the experiment. Moreover, with the Durbin $k-\epsilon$ model, although an unsteady calculation was performed using the highly simplified Marker and Cell (HSMAC) method, no periodic fluctuations were reproduced. Thus, in the case of the Durbin $k-\epsilon$ model, the momentum transfer in the lateral direction was underestimated. As a result, the reattachment length behind the building was longer than that in the experiment.

Figure 2-2-5. Vertical distribution of $\langle u \rangle$ in wake of buildingFigure 2-2-6. Time series fluctuation of speed component v' in wake of the building in the LES cases at $x/b = 0.75$ and $z/b = 1.0$

c) Comparison of turbulent energy k (Figures 2-2-7, 2-2-8)

Figure 2-2-7 shows the distribution of the turbulent kinetic energy k in the section at the center of the building. Only the grid-scale (GS) component was calculated for k , without the subgrid-scale (SGS) component. As revealed by the previously discussed velocity fluctuations behind the building (Figure 2-2-6), in LES (case 1), the velocity fluctuation in the lateral direction was reproduced extremely strongly. Therefore, a high peak in the k value is observed in the recirculating flow region behind the building. On the other hand, in LES (case 2), the peak value is small, and the overall distribution properties are close to those in the experiment. In the case of the Durbin $k-\epsilon$ model, the value of k in the recirculating flow region is much smaller than that indicated in the LES and experimental results. This corresponds to the fact that the above-mentioned periodic fluctuation is not reproduced in the Durbin $k-\epsilon$ model.

Figure 2-2-8 shows the horizontal distribution of k near the ground surface (height $z/b = 0.125$). As with the vertical section, in LES (case 1), an extremely strong peak is observed in the wake of the building. In LES (case 2), on the other hand, two peaks are observed in the wakes of both sides of the building, and the results correspond well with those of the experiment. In the case of the Durbin $k-\epsilon$ model, no such peak is clearly observed behind the building.

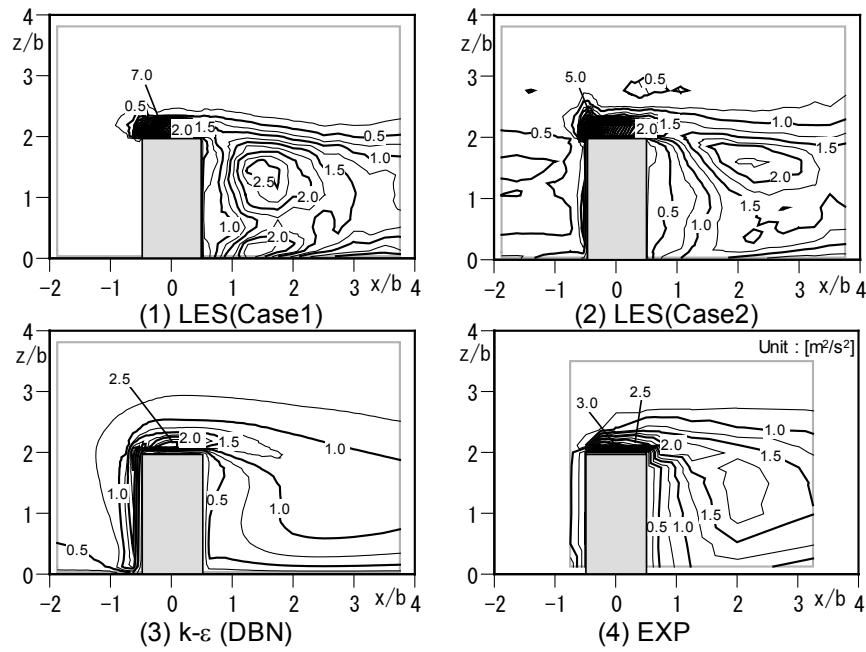


Figure 2-2-7. Distribution of turbulent energy k (vertical section in center of building)

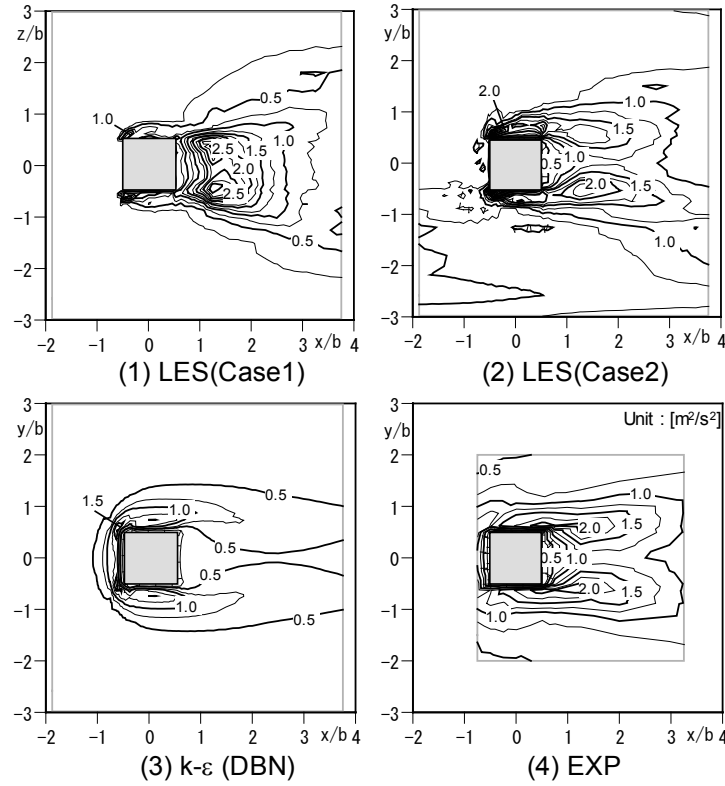


Figure 2-2-8. Distribution of turbulent energy k (horizontal section at height $z/b = 0.125$)

d) Comparison of normal stress (Figure 2-2-9)

The vertical distributions of the normal stress behind the building ($x/b = 0.5$) are shown in Figure 2-2-9. Only the GS component was calculated in the LES results that do not include the SGS component. In the experiment, the lateral component ($\langle v'^2 \rangle / 2k$) is larger than the other components in the region below the building height ($z/b = 2$) because of the impact of the periodic fluctuation caused by the above-mentioned vortex shedding. In the LES (case 1)

results, $\langle v'^2 \rangle / 2k$ is greatly overestimated in comparison with the experimental results and LES (case 2) results. This difference corresponds to the time history of the velocity and the distribution of k discussed above. In LES (case 2), on the other hand, the distribution properties of each component of the normal stress in the recirculating flow region behind the building agree closely with the results of the experiment. In the case of the Durbin $k-\epsilon$ model, although the region where the ‘realizability’ constraint is not satisfied (the region where $\langle u_a'^2 \rangle / 2k < 0$ and $\langle u_a'^2 \rangle / 2k > 1$), which appears in the standard $k-\epsilon$ model and the LK-type modified $k-\epsilon$ model, is not observed, and the anisotropy of the normal stress in the wake of the building in the LES cases and the experiment is not adequately reproduced. In addition, in LES (case 1), a peak value is observed in the distribution of $\langle w'^2 \rangle / 2k$ at the upper region, but no such peak value is seen in the experimental results. This peak is presumed to be caused by numerical oscillation resulting from turbulence not being applied to the inflow velocity in LES (case 1). This problem was also resolved in LES (case 2).

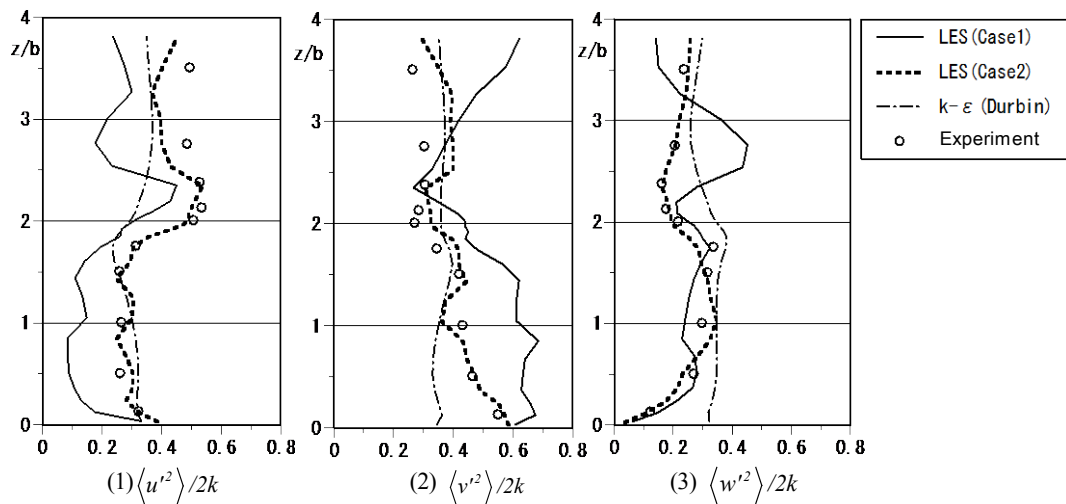


Figure 2-2-9. Vertical distribution of normal stresses behind building

2.2.1.4 Summary

An LES computation that simultaneously produced the appropriate inflow turbulence was applied to the flow around a 1:1:2 high-rise building model placed in a turbulent boundary layer flow. The results were compared with experimental results and the results obtained with the Durbin-type $k-\epsilon$ model to assess their prediction accuracy. The following results were obtained:

- In both LES (case 1) and LES (case 2), the overestimation of the reattachment length behind the building seen in the case of the Durbin $k-\epsilon$ model was improved. This is assumed to be because the periodic fluctuation in the wake of the building due to vortex shedding was reproduced and because the momentum diffusion in the recirculating flow region behind the building was more accurately predicted.
- In the case of the LES (case 1), in which the inflow turbulence was not given to the approaching flow, the vortex shedding in the wake of the building was overestimated, and the lateral fluctuation in this region was overestimated. This suppressed the development of the recirculating flow in the streamwise direction behind the building. Therefore, the velocity distributions differ from those obtained in the experiment.
- In LES (case 2), in which the inflow turbulence was provided, the size of the recirculating flow in the wake, the distribution of k , and the normal stress in the experiment were accurately predicted, and the effectiveness of the LES (case 2) modeling approach was confirmed.

2.2.2 Impact of Smagorinsky constant [18, 20]

2.2.2.1 Introduction

The LES calculation provided the appropriate inflow turbulence clearly and accurately predicted the velocity and turbulence distributions around a building, as shown in the previous section. This section addresses the impact of the value of the Smagorinsky constant C_S on the prediction results. In the LES computation, the computational domain is divided into the driver part used to generate turbulence and the main calculation part used to calculate the flow around the building. The method proposed by Kataoka et al. [16] for determining the input turbulence, which is a simplification of the method proposed by Lund et al. [15], was used, in the same manner as described in the previous section.

2.2.2.2 Outline of numerical calculation

a) Target flow field

The target was the flow around a high-rise building model with a 1:1:2 shape. The experiment was performed at the National Institute for Environmental Studies [2]. It should be noted that the experiment was conducted by a different organization from that which performed the experiment described in the previous sections, although the building shape was exactly the same.

b) Grid discretization and generation method of inflow turbulence

The driver part was set on the upwind side to generate inflow turbulence, and the main calculation part was set on the downwind side to calculate the flow around the building, as shown in Figure 2-2-10. The computational domain was discretized as a $76 (x \text{ direction}) \times 46 (y \text{ direction}) \times 46 (z \text{ direction})$ mesh. The driver part occupied a region with dimensions of $15 (x \text{ direction}) \times 46 (y \text{ direction}) \times 46 (z \text{ direction})$ on the upwind side.

The outflow and inflow boundary conditions were set for each of the two regions (the driver part and the main calculation part). The two regions were thus separated numerically, and the driver part was not affected by the main calculation part on the downwind side.

As a result of this separation of the domain, a smaller Smagorinsky constant C_S could be set for the driver part to prompt turbulence development, and a larger C_S could be set for the main calculation part to restrict numerical diffusion. Hereinafter, the Smagorinsky constant C_S for the driver part is referred to as C_{S1} , and the C_S for the main calculation part is referred to as C_{S2} .

Turbulent fluctuations at the extraction surface were multiplied by the damping coefficient and then injected into the Inlet I (Figure 2-2-10). At the same time, the generated turbulence was injected into the Inlet II, without use of the damping coefficient. The damping coefficient was set so that its value was 1.0 below $9b$, attenuated rapidly toward the upper boundary, and was zero at the upper boundary surface (see the broken line on the label of Figure 2-2-11 (b)). This was done because the boundary condition requires that the velocity at the upper boundary surface be constant. For details of the turbulence generation method, see ref. [18].

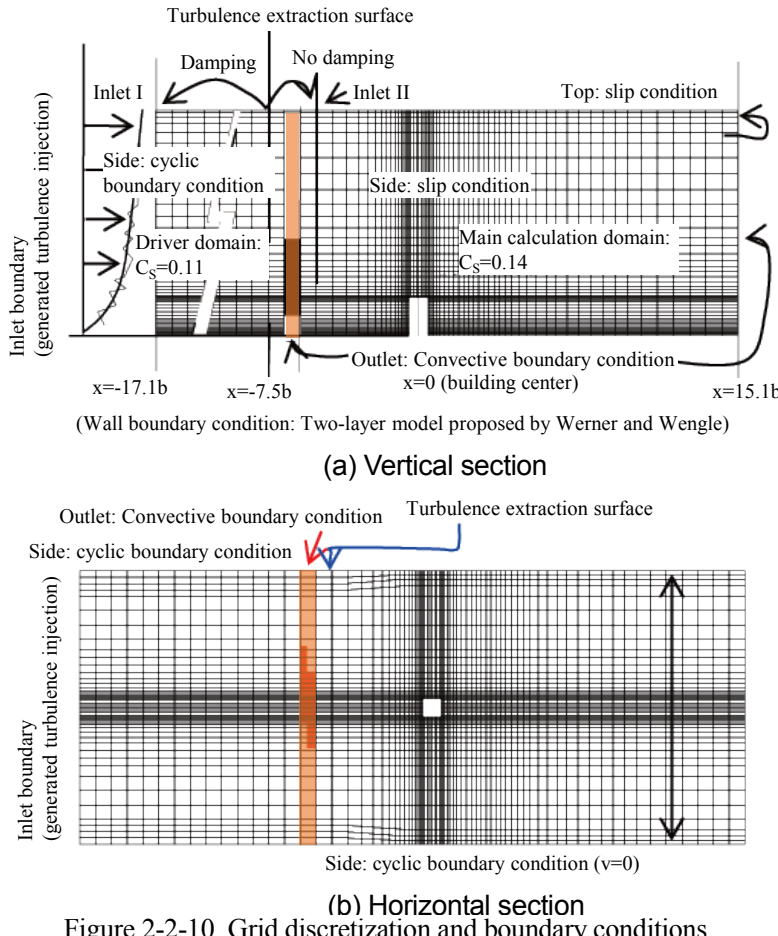


Figure 2-2-10. Grid discretization and boundary conditions

c) Outline of calculation

The SGS model used for the calculation was the standard Smagorinsky model. In the computational domain, the calculation was performed by dividing the region into two parts, as shown in Figure 2-2-10. The minimum grid width was $\Delta z = 0.035b$ on the ground surface and $\Delta z = 0.05b$ on the roof surface of the building. The calculations were conducted for the two cases, as described later in Table 2-2-2. The time interval was $\Delta t = 0.01b / \langle u(2b) \rangle [s]$. The generated inflow turbulence was injected into the inflow boundary surface (Inlet I and Inlet II of Figure 2-2-10(a)).

The vertical profile of the mean streamwise velocity at the inflow boundary was obtained by extrapolating the wind tunnel experiment value [2]. The abstracted turbulence was added to this to obtain the time history of the fluctuating velocity. The horizontal and vertical components of the mean velocity were set to zero, without using the experimental results. The convection boundary conditions were set for the two outflow surfaces of the driver and main calculation parts. The zero-gradient condition of the streamwise velocity was not used for the outflow boundary conditions because it attenuates the turbulence.

The linear power law-type two-layer model proposed by Werner and Wengle [17] was applied to the ground and building wall surfaces. On the upper surface, slip conditions, in which the normal gradient of the tangential velocity component is set to zero, were applied. On the side boundaries of the driver part, cyclic boundary conditions were applied to prompt the development of the horizontal direction turbulence v' . On the horizontal side of the main calculation part, slip conditions were applied based on the results of the wind tunnel experiment.

For the numerical calculations, the self-developed CFD [19] was improved so that v_{SGS} in the diffusion term on the

boundary surface of a control volume was calculated based on a definitional equation without interpolation, to reduce excessive numerical diffusion near the building.

d) Calculation cases

The two cases listed in Table 2-2-2 were calculated. In case 2, different Smagorinsky constants were set for the two regions: in the driver part, the development of turbulence was encouraged by setting a smaller Smagorinsky constant $C_{S1} = 0.11$, while in the main calculation part, numerical diffusion was restricted by setting a higher value $C_{S2} = 0.14$. In case 1, the wall coordinate of node 1 on the ground surface had values of 22 (Inlet I) to 39 (extraction surface), with values of 10–26 on the roof of the building. In case 2, these values were 22 (Inlet I) to 41 (extraction surface) and 12–24 on the roof of the building.

Table 2-2-2. Calculation cases

	C_{S1}	C_{S2}
Case 1	0.12	0.12
Case 2	0.11	0.14

2.2.2.3 Distribution of inflow turbulence

a) Distribution of statistical values of inflow turbulence

Figures 2-2-11 (case 1) and 2-2-12 (case 2) show the distributions of the statistical values along the vertical center section ($y=0$) of the abstraction location of the turbulent fluctuations (u' , v' , w') of the generated inflow turbulence ($u = \langle u \rangle + u'$, $v = \langle v \rangle + v'$, $w = \langle w \rangle + w'$). The time-averaged streamwise velocity $\langle u \rangle$ almost agreed with the experimental results in both cases. The turbulent fluctuation of the streamwise velocity component u'_{rms} also almost agreed with the experiment results in both cases, but the statistical values were lower than the experimental values near the height $z = b$. In case 1 (Smagorinsky constant of the driver part $C_{S1} = 0.12$), the values of the turbulent fluctuation of the lateral velocity component v'_{rms} and the vertical component w'_{rms} were lower than the experimental values. In case 2, for which the Smagorinsky constant C_S of the driver part was set lower to prompt the development of turbulence ($C_{S1} = 0.11$), the values of v'_{rms} and w'_{rms} were larger and closer to the experimental values.

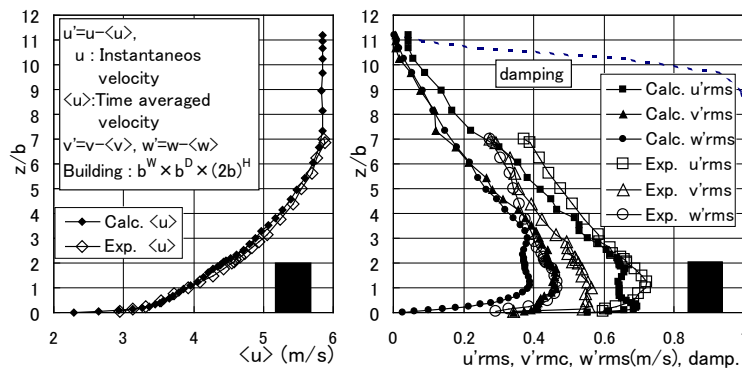


Figure 2-2-11. Comparison of calculated (generated) values and experimental values of inflow turbulence (case 1; $C_{S1} = 0.12$, $C_{S2} = 0.12$, average time = $1742.5b/u$ ($2b$))

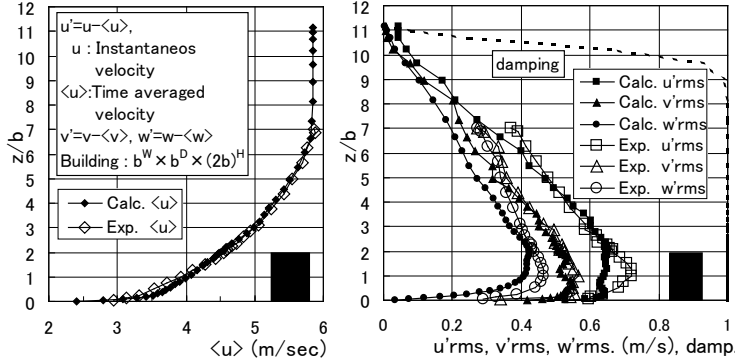


Figure 2-2-12. Comparison of calculated (production) values and experimental values of inflow turbulence (case 2; $C_{s1} = 0.11$, $C_{s2} = 0.14$, average time = $2047.5b/u$ ($2b$))

b) Distribution of power spectrum of inflow turbulence

The number of grid divisions in the streamwise direction (x) between the abstraction location and the injection location of the turbulence in the driver part was 12, and the length of the driver part in the streamwise direction (x) was $L_x = 9.6b$. The spatial intervals were equal intervals of $\Delta x = 0.8b$. The power spectrum at point (1) ($z = b$) in Figure 2-2-10(a) was examined, and the velocity at this height was almost $<u(z = b)> = 0.86<u(2b)>$ ($<u(2b)> = 4.55$ [m/s] at the inflow in the experimental value). At the turbulence abstraction location and injection location of the driver part (Inlet I), cyclic boundary conditions were imposed on the turbulent fluctuation. Thus, a wave with the frequency of $f_D = \frac{<u(z)>}{L_x}$, which is determined from the velocity and length in the streamwise direction, develops well.

The frequency can be made dimensionless by normalizing it with respect to the building width b and velocity $u(z)$. This is the same concept as that on which the Strouhal number is based:

$${}^b f_D = f_D \frac{b}{<u(z)>} = \frac{b}{L_x} = \frac{1}{9.6} = 0.104 \quad (2.1.3)$$

This frequency develops in the power spectrum of the inflow turbulence. Waves with integral multiple frequencies of this are also produced. Moreover, waves with different frequencies are also produced by the advection term of the N-S equation.

If the maximum dimensionless frequency can be resolved (generated) with $2\Delta x$ in the grid of the driver part, this frequency can be made dimensionless by normalization with respect to the building width b and average velocity, as shown in eq. (2.1.4). This is the highest frequency that can be developed in the driver part.

$${}^b f_{2\Delta x} = \frac{<u(z)>}{2\Delta x} \times \frac{b}{<u(z)>} = \frac{b}{2\Delta x} = \frac{1}{2 \times 0.8} = 0.625 \quad (2.1.4)$$

Therefore, in the driver part, velocity fluctuation occurs in the range of the dimensionless frequency ${}^b f_D = 0.104$ –0.625. In fact, fluctuation occurs in the range of ${}^b f_D = 0.1$ –0.2, as shown below.

With respect to the time series data, a value obtained by time-averaging ten steps of the calculation is considered to be one step of the time series data. Therefore, the sampling interval of the time series data is $\Delta \tau = 10\Delta t = 0.1b / <u(2b)> [s]$. Based on a frequency that is dimensionless with respect to the building width b and velocity $<u(b)>$, the frequency range that can be used for spectrum analysis is expressed by eqs. (2.1.5) and (2.1.6) for a number of time series data points N .

$${}^b f_{Samp} = \frac{1}{N \Delta \tau'} \sim \frac{1}{2 \Delta \tau'} \quad (2.1.5)$$

$$\Delta \tau' = \Delta \tau \frac{\langle u(b) \rangle}{b} = 0.1 \frac{\langle u(b) \rangle}{\langle u(2b) \rangle} = 0.1 \times 0.86 = 0.086 \quad (2.1.6)$$

Figure 2-2-13 shows the power spectrum distribution of the fluctuating component of the driver part (point 1 in Figure 2-2-10(a)) in case 1 ($C_{s1} = C_{s2} = 0.12$). The power spectrum was calculated using Maximum Entropy Method (MEM) [21]. The number of data points N is 5,880 steps. The dimensionless frequency range that can be calculated with the sampling interval is ${}^b f_{Samp} = 1/(5880 \times 0.086)$ to $1/(2 \times 0.086) = 0.002$ to 5.8. The sampling interval provides adequate resolution for the limit, ${}^b f_D = 0.104$ to 0.625, according to the spatial intervals and length of the driver part. In addition, the frequency axis (x-axis) is made nondimensional by normalization with respect to the building width b and velocity $\langle u(b) \rangle$. The peak frequencies are shown in the figure. In all three directions, the power is concentrated in the dimensionless frequency range of 0.1–0.2.

The power spectrum of u' (Figure 2-2-13(a)) shows a high power value between the frequency ${}^b f_D$ (eq. (2.1.3)), determined from the driver part length, and a frequency twice as high. Higher frequencies do not develop under the effects of the eddy viscosity coefficient of the sub-grid scale, ν_{SGS} . The large power is extended in the low-frequency area. The power spectrums of v' (Figure 2-2-13(b)) and w' (Figure 2-2-13(c)) feature sharp peaks. The decay of the power spectrum in three components is significant in the high-frequency region.

Figure 2-2-14 shows the power spectrum distribution of the fluctuating component of the driver part (point 1 in Figure 2-2-10(a)) of case 2 ($C_{s1} = 11$, $C_{s2} = 0.14$). The number of data points N is 20,835 steps. The dimensionless frequency that can be calculated with the sampling interval is ${}^b f_{Samp} = 1/(20835 \times 0.086)$ to $1/(2 \times 0.086) = 0.00056$ to 5.8. The power spectrum of u' (Figure 2-2-14(a)) features a width a little broader than that of case 1 (Figure 2-2-13(a)). The power spectra of v' (Figure 2-2-14(b)) and w' (Figure 2-2-14(c)) feature low peaks and broad widths. The power of the three velocity components extends to the high-frequency side more than in case 1. This is presumed to be the result of the small attenuation of the power on the high-frequency side, due to the smaller value of C_s . This indicates that in both cases, the Smagorinsky constant C_s has a considerable impact on the power spectrum distribution.

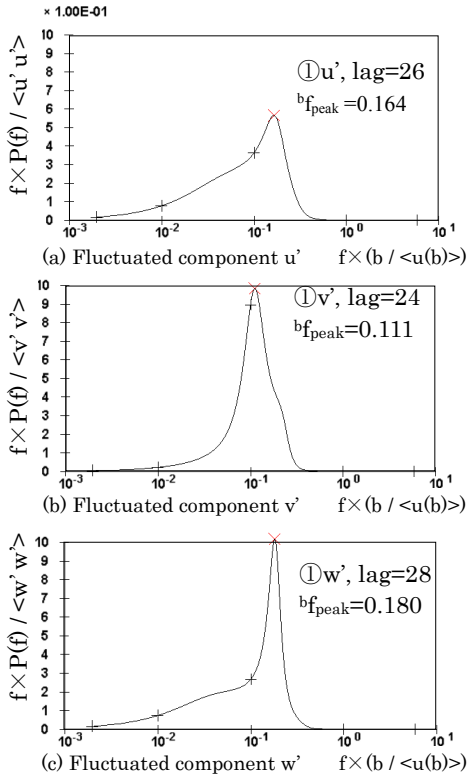


Figure 2-2-13. Power spectrum of inflow turbulence
(Case 1, point 1 ($x = -7.5b$, $y = 0$, $z = b$)
(driver region)) ($N = 5,880$)

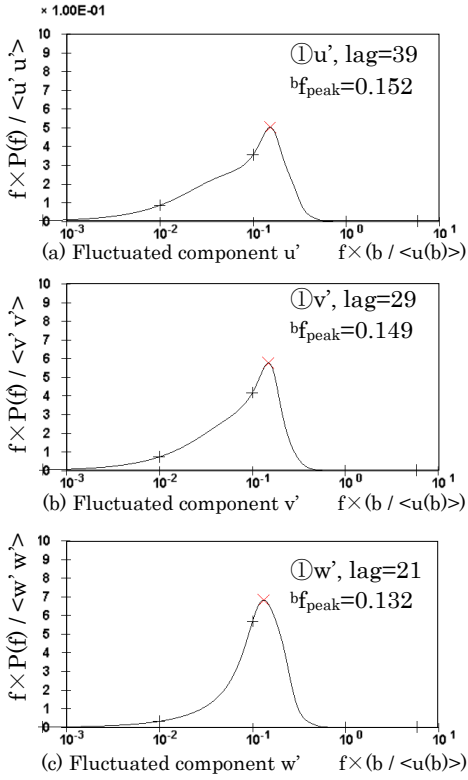


Figure 2-2-14. Power spectrum of inflow turbulence
(Case 2, point 1 ($x = -7.5b$, $y = 0$, $z = b$)
(driver region)) ($N = 20,835$)

2.2.2.4 Comparison of calculation results with experiment results around building

Because of limited space, only the results for case 2 are shown. For the results for case 1, see ref. [18].

a) Comparison of statistical values of case 2 with experimental results on vertical center section

Figure 2-2-15 shows a comparison of the calculation result for case 2 ($C_{s1} = 0.11$, $C_{s2} = 0.14$) and the experimental result. Figure 2-2-15(a) shows a comparison of the time-averaged streamwise velocities $\langle u \rangle$. The calculation results almost agree with the experiment. However, there is a large deficit in $\langle u \rangle$ of the calculation results than in the experimental results from the top surface to the wake of the building. In addition, in the wake of the building, the recovery of $\langle u \rangle$ in the calculation results occurs in more downwind region and the recirculating flow region behind the building is larger in the calculation results than the experimental results. In other words, the reattachment length behind the building is longer in the calculation results than in the experimental results, although the results are much closer than for the $k-\epsilon$ model described in the previous section. Figure 2-2-15(b) shows the time-averaged lateral velocity $\langle v \rangle$ in the vertical central section, where $\langle v \rangle$ of the calculation results is almost zero. Figure 2-2-15(c) compares the time-averaged vertical velocity $\langle w \rangle$ in the vertical central section. It shows very good agreement between the calculation results and experimental results, but it shows a slight disagreement with the experimental results near the building height. Figure 2-2-15(d) compares the turbulent kinetic energy k in the vertical central section. Here, the three components of the velocity fluctuations, which were used to calculate k , are the sum of the GS and SGS components. However, the SGS component was so small that it could be ignored. On the measurement line

in front of the building at $x = -0.75b$, the results for case 2 agree almost perfectly with the experimental results, as a result of setting $C_{s2} = 0.14$, which restricted excessive turbulent diffusion in this region. On the roof surface, the calculation results are much larger than the experimental results. In the recirculating flow region behind the building, the turbulent kinetic energy k is smaller than in the case of the experiment. This suggests that the momentum diffusion caused by the periodic motion due to the Karman vortex in the horizontal direction behind the building is smaller than in the experimental results. Figures 2-2-15(e) to (g) shows that the distribution of the three components of the velocity fluctuation u'_{rms} is overestimated from the roof surface to the wake region. On the other hand, v'_{rms} and w'_{rms} are underestimated in the recirculating flow region behind the building. These constitute the distribution of the turbulent kinetic energy k . Figure 2-2-15(h) shows the distributions of the Reynolds shear stress $\langle u'w' \rangle$. In other words, from the roof surface to the wake region, in the range within which the u'_{rms} component (Figure 2-2-15e) is overestimated, a large Reynolds shear stress $\langle u'w' \rangle$ is observed. This is consistent with the large velocity deficit in the time-averaged streamwise velocity $\langle u \rangle$ at this location.

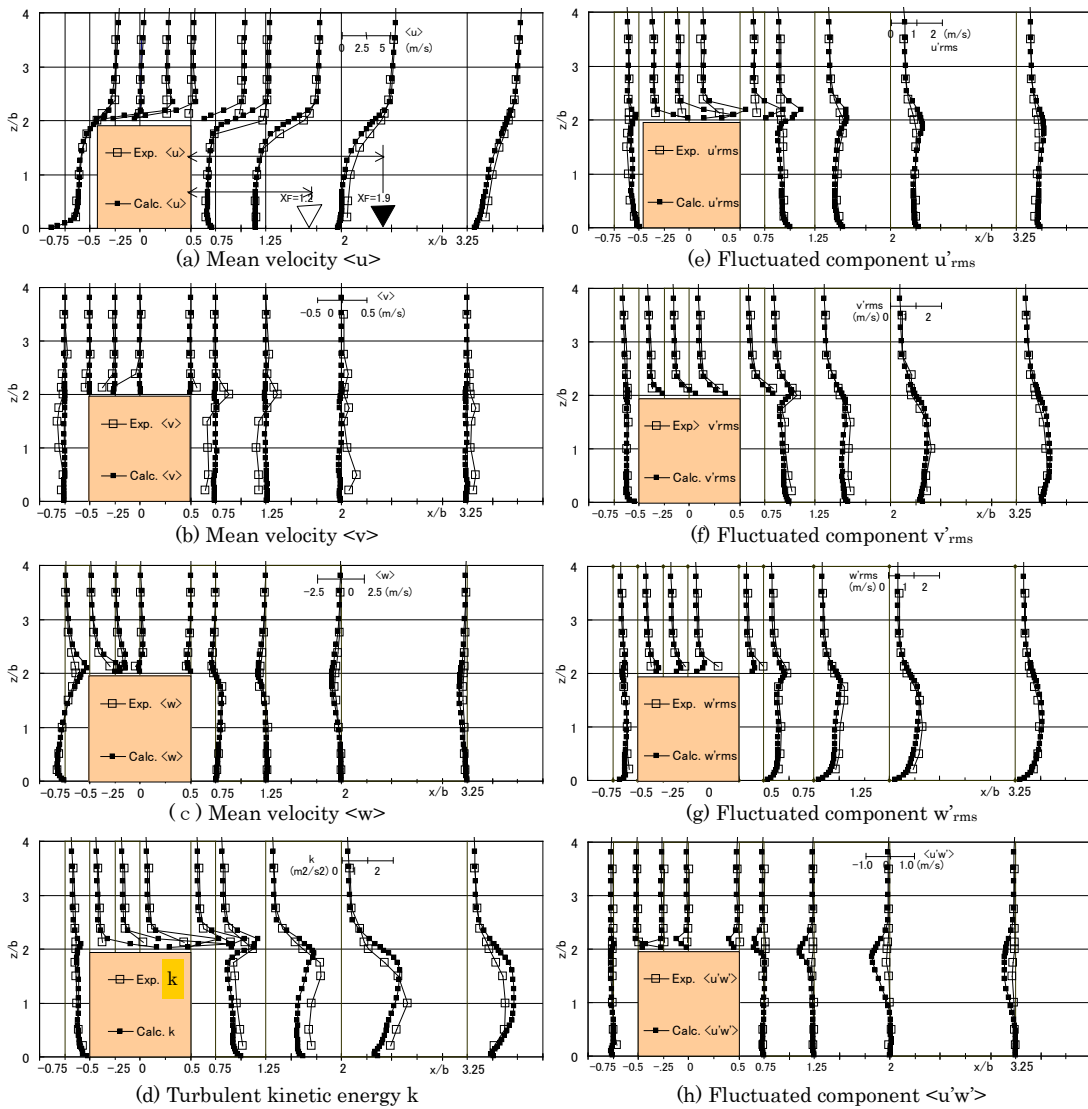


Figure 2-2-15. Comparison of calculation results (case 2 ($C_{s1} = 0.11$, $C_{s2} = 0.14$)) and experiment results (vertical center section, $y = 0$)

b) Distribution of power spectrum of wind speed in wake of building

Figures 2-2-16 and 2-2-17 show the distribution of the power spectrum of the velocity fluctuation behind the building (point 2 in Figure 2-2-10). Figure 2-2-16 shows the power spectrum for case 1 ($C_{s1} = C_{s2} = 0.12$). The shape of the power spectrum of the u' component in Figure 2-2-16(a) is gently distributed, and it shows high power from 0.1 to 0.3 in the dimensionless frequency normalized with respect to the building width b and velocity (Strouhal number). The power extends to the higher frequency because the grid width is narrower than that of the driver part. Figure 2-2-16(b) shows the power spectrum of the v' component. The power spectrum has a sharp peak, and its peak frequency is $^b f_{peak} = 0.125$ in the Strouhal number. This is close to the Strouhal number in the wake of the building, and it shows that Karman vortex-type periodic fluctuation occurs in the wake of the building. Figure 2-2-16(c) shows the power spectrum of the w' component, and it has a blunt peak. Figure 2-2-17 shows the power spectrum for case 2 ($C_{s1} = 0.11$, $C_{s2} = 0.14$). The power spectrum of the u' component in Figure 2-2-17(a) has a flat distribution at about $^b f_{peak} = 0.138$. Figure 2-2-17(b) shows the power spectrum of the v' component. It shows a sharper and higher peak than in case 1. The peak frequency is $^b f_{peak} = 0.126$ in the Strouhal number. This too is close to the Strouhal number in the wake of the building. Figure 2-2-17(c) shows the power spectrum of the w' component, and it has a blunt peak. A comparison of Figures 2-2-16(b) and 2-2-17(b) shows that the Karman vortex-type periodic motion behind the building has more power for case 2 than for case 1. This indicates that the larger Smagorinsky constant $C_{s2} = 0.14$ reduce the numerical diffusion near the building slightly.

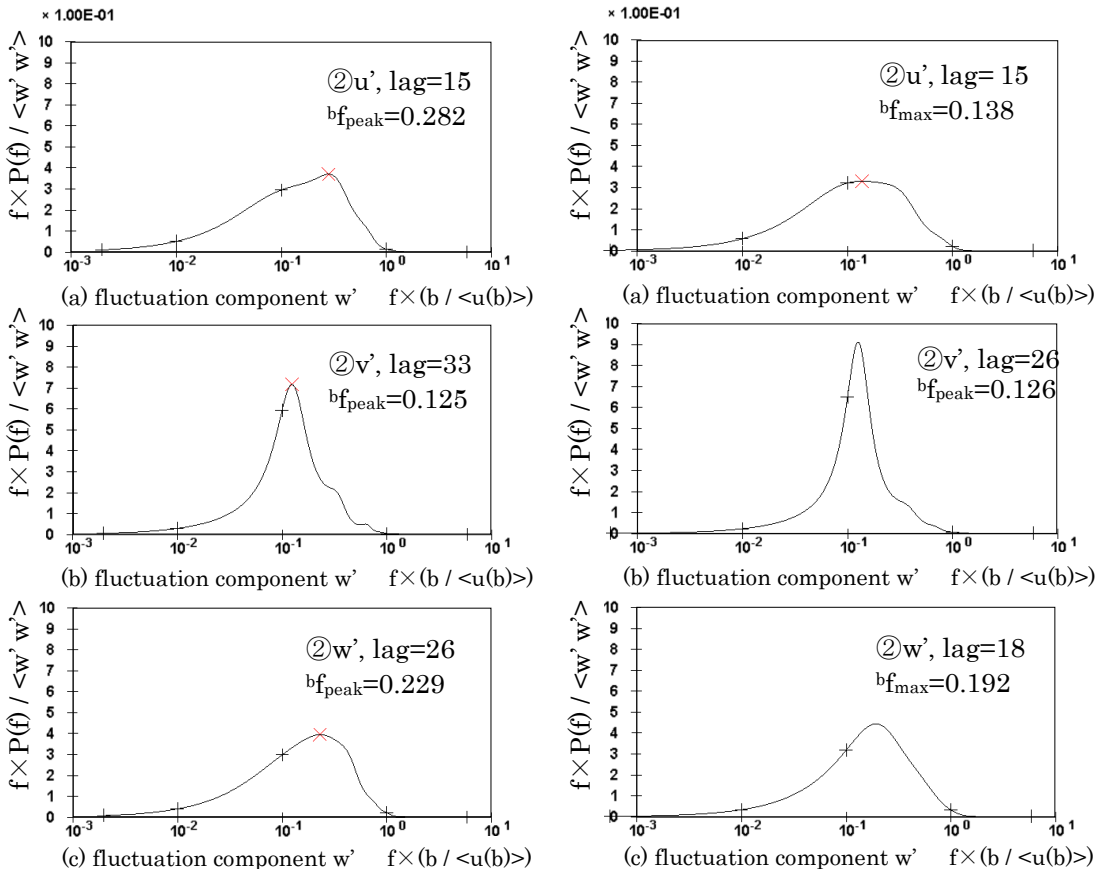


Figure 2-2-16. Power spectrum of wind speed in wake of building (case 1, point [2] ($x = 1.48b, y = 0, z = b$) (wake vergion) (time series data number = 5880)

Figure 2-2-17. Power spectrum of wind speed in wake of building (case 2, point [2] ($x = 1.48b, y = 0, z = b$) (wake vergion) (time series data number = 20835)

c) Considerations for the calculation results around building

By improving the calculation method for v_{SGS} [18] and setting a higher C_s value, the distributions of the turbulent fluctuations were made to agree almost perfectly with the experimental results for the front of the building. It was also confirmed that, as shown in Figures 2-2-16(b) and 2-2-17(b), Karman vortex-type periodic fluctuation occurs in the wake of the building. However, the turbulent fluctuation was overestimated near the roof surface and sides of the building. The gradients of Reynolds shear stress $\frac{\partial \langle u'w' \rangle}{\partial z}$ (on the roof) and $\frac{\partial \langle u'v' \rangle}{\partial y}$ (side surfaces of the building; see ref. [18]) are also overestimated. This is a result of insufficient suppression of the turbulent fluctuation in this region. Because v_{SGS} is small, the momentum energy transport from the grid scale to the sub-grid scale ($v_{SGS} |\bar{S}|^2$) is underestimated, and the GS components of u'_{rms} and v'_{rms} are too large. As a result, the overestimated Reynolds shear stress balanced with the time-averaged velocity distribution where $\langle u \rangle$ was defective. In addition, the overestimated fluctuation along the roof and side surfaces of the building weakens the Karman vortex-type periodic fluctuation and the mixing in the lateral direction behind the building. This is why the recovery of the velocity occurred too far downwind and the reattachment length behind the building was still overestimated.

2.2.2.5 Summary

- With respect to the inflow turbulence generation, it was confirmed that applying the inflow velocity profile from the experiment can reproduce a roughly similar distribution for the velocity fluctuations. It was also confirmed that it is possible to make this distribution resemble that obtained from the experiment more closely by modifying the value of C_s .
- With respect to the flow field around the building, it was shown that very good prediction accuracy could be obtained using the inflow turbulence obtained by this method.
- The overestimation of the turbulence in front of the building was improved by modifying the method for calculating v_{SGS} and using a larger value for the Smagorinsky constant C_s .
- The reattachment length behind the building was still slightly overestimated. Thus, it is necessary to improve the prediction methods used, including a method for changing the Smagorinsky constant dynamically.

2.3 Flow around a high-rise building with a 4:4:1 shape [41]

2.3.1 Outline of object flow field

In this section, the flow around a building model with a 4:4:1 (height: width: depth) shape in a boundary layer flow is analyzed (Figure 2-3-1). To obtain validation data for the CFD prediction results, measurements were performed using the wind tunnel at the Niigata Institute of Technology. The model had the dimensions $b = 0.05$ m (b : building width) and $H = 0.2$ m ($= 4.0b$) (H : building height). The average inflow velocity at the building height $\langle u_H \rangle$ was 5.1 m/s. The Re number, based on $\langle u_H \rangle$ and H , was 72,000. The time-averaged and fluctuated

wind velocity was measured using a split fiber probe in each of the three directions.

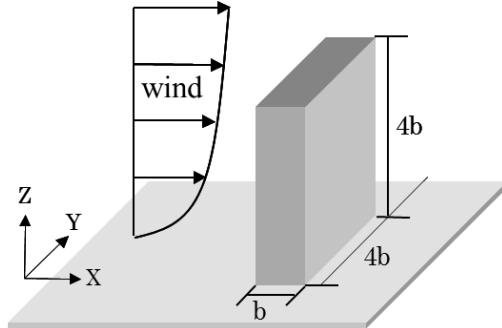


Figure 2-3-1. Flow field analyzed

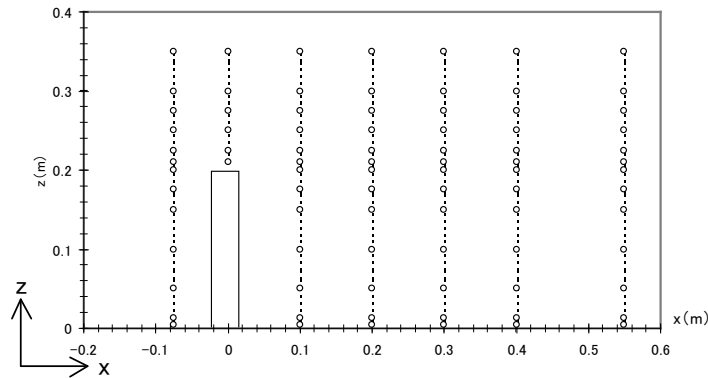


Figure 2-3-2. Measurement points in vertical cross section ($y = 0$)

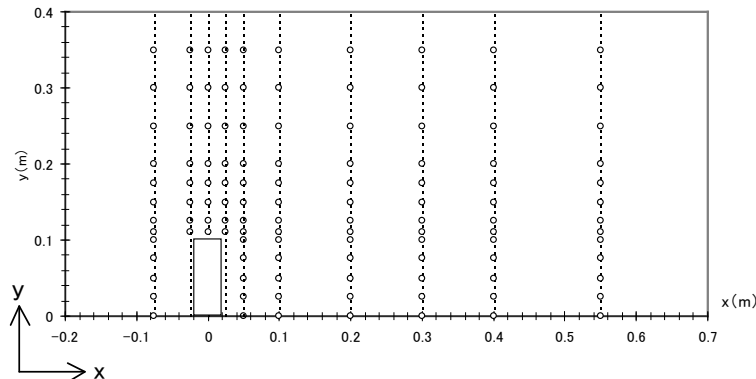


Figure 2-3-3. Measurement points on horizontal surface ($z = 0.0125$ m)

2.3.2 Effects of various boundary conditions (study of benchmark basic calculation conditions)

2.3.2.1 Comparison cases

Based on the previously presented results for the 2:1:1 building model, the basic calculation conditions of the benchmark test were set as listed in Table 2-3-1. The basic conditions in Table 2-3-1 were considered to represent case 1. The calculation cases are listed in Table 2-3-2. Cases 2 and 3 had different computational domains: $20.5b$ (x) \times $14.0b$ (y) \times $12.1b$ (z) and $20.5b$ (x) \times $9.2b$ (y) \times $8.5b$ (z), respectively. Cases 4 and 5 had different grid discretizations: 134 (x) \times 80 (y) \times 122 (z) and 34 (x) \times 20 (y) \times 31 (z), respectively. Preliminary calculations were conducted to study

the effects of these conditions on the calculation results. The commercial software STREAM for Windows ver. 4.0 was used with the standard $k-\varepsilon$ model as the turbulence model for all cases considered.

For the 2:1:1 building model, a simple boundary layer flow without a building was analyzed. The method for setting the ground surface boundary conditions was studied to maintain the vertical profiles of the velocity and the turbulent kinetic energy from the inlet boundary to the outlet boundary. Based on the results, the z_0 -type logarithmic law was used for the ground surface boundary conditions in this benchmark test. The u^* value was estimated using the following equation, based on the value of k ($0.344 \text{ m}^2/\text{s}^2$) from the experimental measuring point ($z = 0.003 \text{ m}$) closest to the wall surface.

$$u^* = C\mu^{1/4}k^{1/2} = 0.09^{1/4} \times 0.34^{1/2} = 0.32 \text{ m/s} \quad (2.3.1)$$

Substituting this u^* value and the wind velocity at this height $\langle u \rangle = 2.8 \text{ m/s}$ into the logarithmic law including z_0 , a value of $z_0 = 9.6 \times 10^{-5} [\text{m}]$ is obtained.

Table 2-3-1. Basic calculation conditions

Computational domain	The computational domain covers $33b$ in the streamwise (x) direction, $36b$ in the lateral (y) direction, and $36b$ in the vertical (z) direction. These dimensions correspond to the size of wind tunnel.
Inflow boundary	Interpolated values of $\langle u(z) \rangle$ and $k(z)$ from the experimental results are imposed. The vertical profile of the mean velocity $\langle u(z) \rangle$ approximately obeys a power law expressed as in the experiment. The value of ε is obtained from the relation $P_k = \varepsilon$
Lateral and upper surfaces of the computational domain	The normal velocity components defined at the boundary and the normal gradients of the tangential velocity components (k and ε) are set to zero.
Downstream boundary	A zero-gradient condition is used.
Ground surface boundary	The velocity boundary condition uses a logarithmic law of a form that contains the roughness length z_0 ($z_0 = 9.6 \times 10^{-5} [\text{m}]$).
Building surface boundary	The generalized log law for a smooth wall is adopted.
Grid discretization	The computational domain is discretized into $67(x) \times 40(y) \times 61(z)$ in the case of half domain. The grid width adjacent to ground surface is set to $0.008 [\text{m}] (= 0.16b)$. z^+ estimated as u^* of the inflow profile is approximately 85. The grid width adjacent to the corner of the building is set to $0.005 [\text{m}] (= 0.1b)$.
Discretization scheme for convection terms	The QUICK scheme is applied to all convection terms.
Other conditions	The commonly used methods for each organization are adopted for the numerical conditions without further specification.

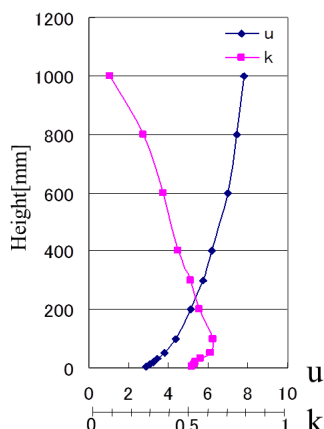


Figure 2-3-4. Inflow boundary conditions

Table 2-3-2. Calculation cases for investigating basic conditions

Computational domain	Grid discretization	Side and upper boundaries	Note
Case 1	Large	Basic	Blockage ratio: 1.2%
Case 2	Narrow 1	Basic	Blockage ratio: 4.7%
Case 3	Narrow 2	Basic	Blockage ratio: 10.2%
Case 4	Large	Fine	1/2 of the basic grid
Case 5	Large	Coarse	Double the basic grid

a) Impact of computational domain (Cases 2 and 3)

Under the basic conditions, the height and width of the computational domain are considered to be identical to the section of the wind tunnel used for the experiment. Cases 2 and 3 are the cases for which the computational domains are narrowed and the side and upper surfaces are considered to be free inflow–outflow boundaries.

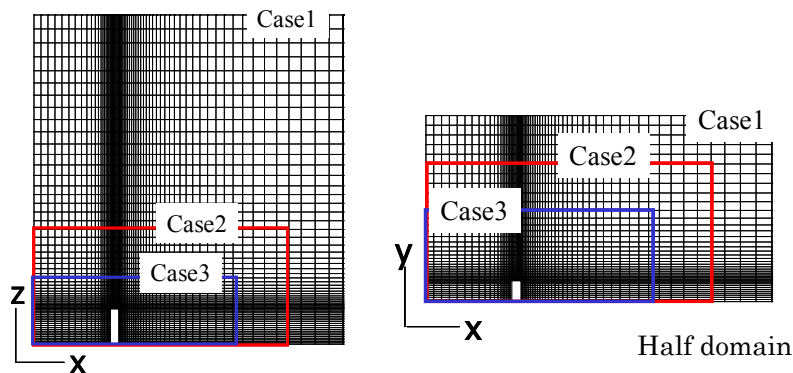


Figure 2-3-5. Computational domain and grid arrangement

b) Effect of grid discretization

With the computational domain considered equal to the basic conditions, the case that considered the width of all the grids to be 1/2 of the basic conditions (case 4) and the case that considered the width of all the grids to be double the basic conditions were compared.

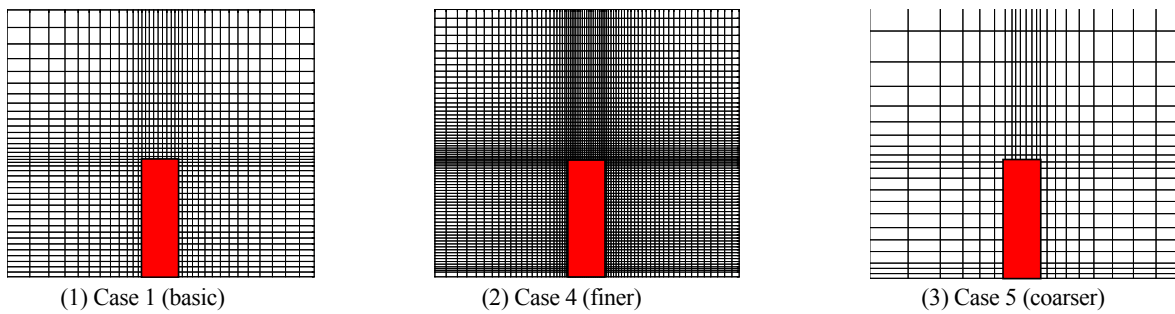


Figure 2-3-6. Comparison of grid discretizations (only grids near building are shown)

2.3.2.2 Analysis results

Figures 2-3-7 to 2-3-14 show the calculated results. In the cases compared in this study, as long as free inflow–outflow boundary conditions are used for the upper and side surfaces of the computational domain, the impact of the computational domain on the results is relatively small. However, as seen in the comparison of the

horizontal distributions of $\langle u \rangle$ on the measurement line in the wake region, in Case 3, in which the computational domain is the smallest, the reverse flow behind the building is overestimated, and the agreement with the experimental results is slightly worse (Figure 2-3-9).

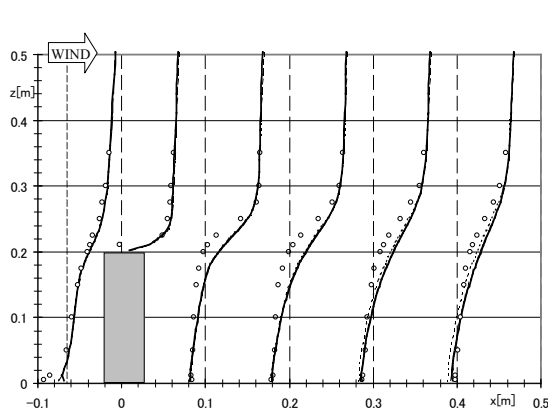


Figure 2-3-7. Vertical distribution of $\langle u \rangle$ (building center section)

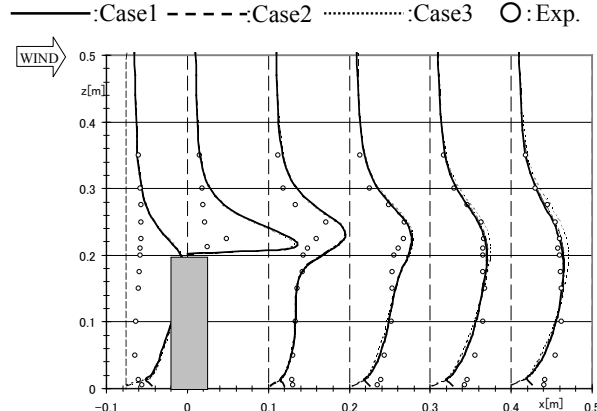


Figure 2-3-8. Vertical distribution of k (building center section)

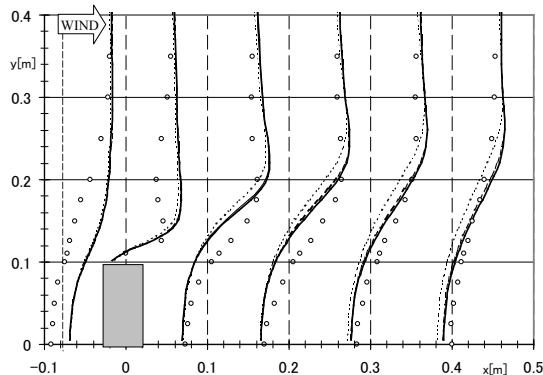


Figure 2-3-9. Horizontal distribution of $\langle u \rangle$ ($Z = 0.0125$ m)

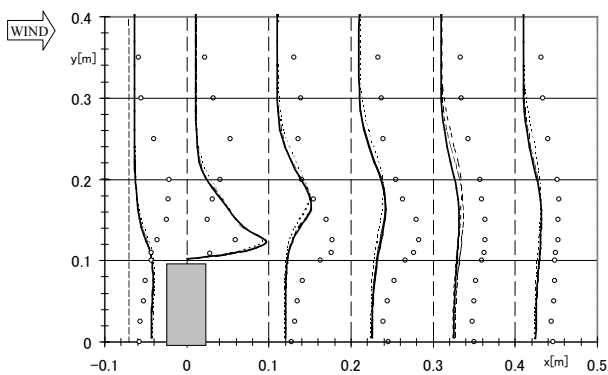


Figure 2-3-10. Horizontal distribution of k ($Z = 0.0125$ m)

In case 5, in which the grids are twice as coarse, there is a tendency for the peak of k to be blunt near the windward corner of the building. However, in Figure 2-3-12, the impact on the velocity distribution is very small (Figures 2-3-11, 2-3-13). With respect to discrepancies with the experimental results, it is noted that the overestimation of k at the windward corners of the building and the overestimation of the recirculating flow behind the building are caused by shortcomings of the standard $k-\epsilon$ model and the RANS (Reynolds-averaged Navier-Stokes) modeling approach. This tendency corresponds to the results presented in section 2.1. Based on these results, benchmark tests were performed under the conditions listed in Table 2-3-1.

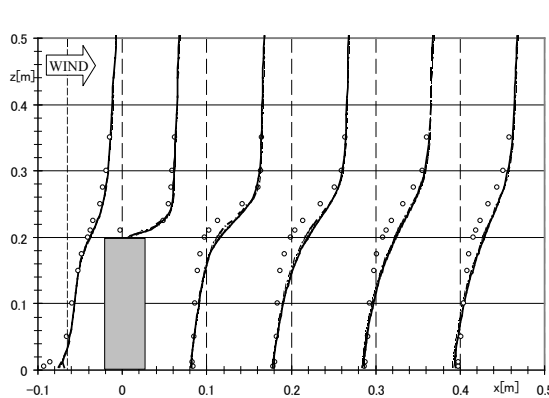


Figure 2-3-11. Vertical distribution of $\langle u \rangle$
(building center section)

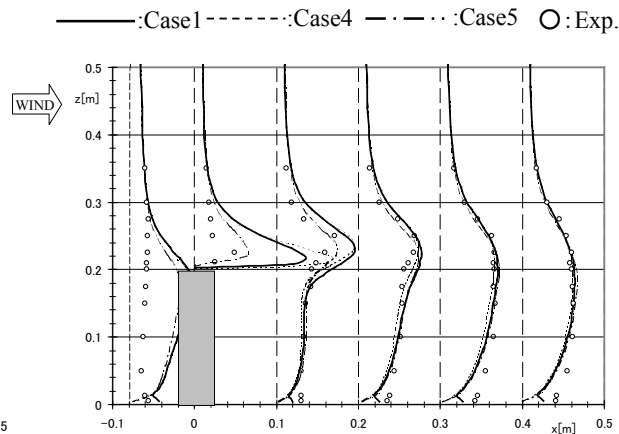


Figure 2-3-12. Vertical distribution of k
(building center section)

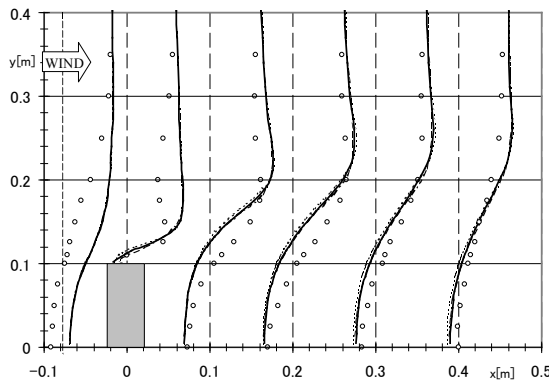


Figure 2-3-13. Horizontal distribution of $\langle u \rangle$
($Z = 0.0125$ m)

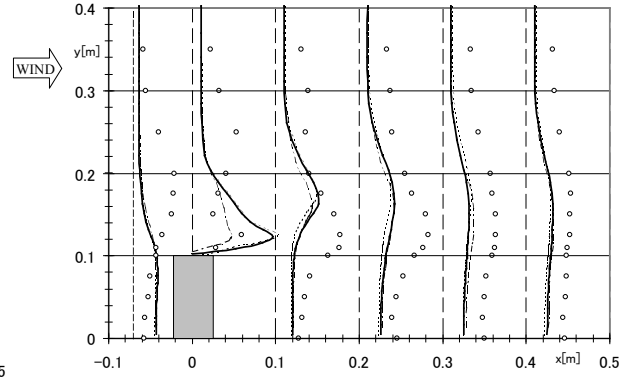


Figure 2-3-14. Horizontal distribution of k
($Z = 0.0125$ m)

2.3.3 Results of benchmark tests by several organizations—mainly the effect of the turbulence model

2.3.3.1 Calculation cases

Table 2-3-3 lists the calculation results submitted by different organizations. The specified calculation conditions all conform to the basic conditions, and only the differences between the turbulence models were studied. The LES calculation was performed using a third-order upwind scheme for the convection term, without using an SGS model. The LES used a multi-block structure grid with a total grid number of 502,127. The minimum grid width was $0.3 \times 10^{-3} b$, with a value of $1.6 \times 10^{-4} b$ on the building surface. Details of the analysis method are given in refs. [16] and [22]. For the low-Re-type $k-\epsilon$ model, the finer grid, in which the wall coordinate at the velocity definition point adjacent to the building surface was approximately 3 near the corner, was used, and the grid discretization was 147 (x) $\times 84$ (y) $\times 134$ (z).

2.3.3.2 Comparison of reattachment lengths behind the building (Table 2-3-3)

A list of the reattachment lengths behind the building X_F is given in Table 2-3-3. The values of X_F were obtained by linear interpolation of the location of the reversal point for the sign of the streamwise velocity $\langle u \rangle$ at a height of 0.0125 m. In all the calculation results, as in the case for the 2:1:1 building, the reattachment length behind the

building was greater than that in the experiment results. The reason is assumed as follows. In the case of the RANS model, although the unsteady calculation was performed, the periodic fluctuation behind the building was not reproduced. Therefore, the momentum diffusion in the wake of the building was underestimated, and the recirculating flow behind the building became large. As discussed in the 2:1:1 building case, even for the results of the same standard $k-\varepsilon$ model, the results were a bit different depending on the CFD code used. To explain these differences, it is necessary to make a more detailed comparison of the calculation conditions, such as the convergence judgment condition and the boundary conditions of k and ε for the solid surface, which are not specified by the basic conditions. In a comparison conducted with the same code, excluding the Durbin model (C2), almost all of the modified $k-\varepsilon$ models tended to estimate the reattachment lengths as being greater than the lengths estimated by the standard $k-\varepsilon$ models. This point is also consistent with the results described in Section 2.1. The LES results conformed very closely to those of the experiment, although the analysis conditions were different from those of the other calculations.

Table 2-3-3. Calculation conditions and calculation cases

Organization	Software	Turbulence model	Scheme for advection terms	Computational method and time integral scheme	$X_F[m]$	CASE			
A	FLUENT ver.6.0	$k-\varepsilon$ (standard)	QUICK	SIMPLE, steady solution	0.54	A1			
		$k-\varepsilon$ (RNG) [23]			0.62	A2			
		$k-\varepsilon$ (Realizable) [24]			0.68	A3			
B	STAR-CD ver.3.15	$k-\varepsilon$ (standard)	QUICK	SIMPLE, steady solution	0.58	B1			
		$k-\varepsilon$ (non-linear)Shih [25]			0.66	B2			
C	Self-made A	$k-\varepsilon$ (standard)	QUICK	HSMAC, solution with implicit scheme	0.50	C1			
		Durbin $k-\varepsilon$ [26]			0.46	C2			
D	STREAM for Windows ver.4	$k-\varepsilon$ (standard)	QUICK	SIMPLE, steady solution	0.46	D1			
		$k-\varepsilon$ (LK) [27]			0.66	D2			
		$k-\varepsilon$ RNG [24]			0.67	D3			
		Low-Reynolds-number $k-\varepsilon$ (ANK model) [28]			0.68	D4			
E	Self-made B	$k-\varepsilon$ (standard)	QUICK	Artificial compressibility method, explicit	0.58	E1			
		$k-\varepsilon$ (Mixed time scale) [29]			0.59	E2			
LES (3rd-order upwind scheme used for discretizing the convection term) [16]					0.38	LES			
Experiment					0.38				

2.3.3.3 Contours of wind speed ratio near ground surface (Figure 2-3-15)

Figure 2-3-15 shows the contours of the wind speed ratio, which is defined as the ratio of the scalar velocity near the ground surface ($z = 0.0125 \text{ m} = H/16$) to the inflow wind velocity at the same height (3.11 m/s). All of the calculation results estimate the overall wind speed as being larger than in the experiment results.

a) Comparison between standard $k-\varepsilon$ models (Figure 2-3-15 (1) to (5))

All the calculation results show almost identical distributions, with no differences depending on the code used. However, focusing on the region enclosed by the contour line of 1.2 near the side of the building, the distributions are slightly different in size.

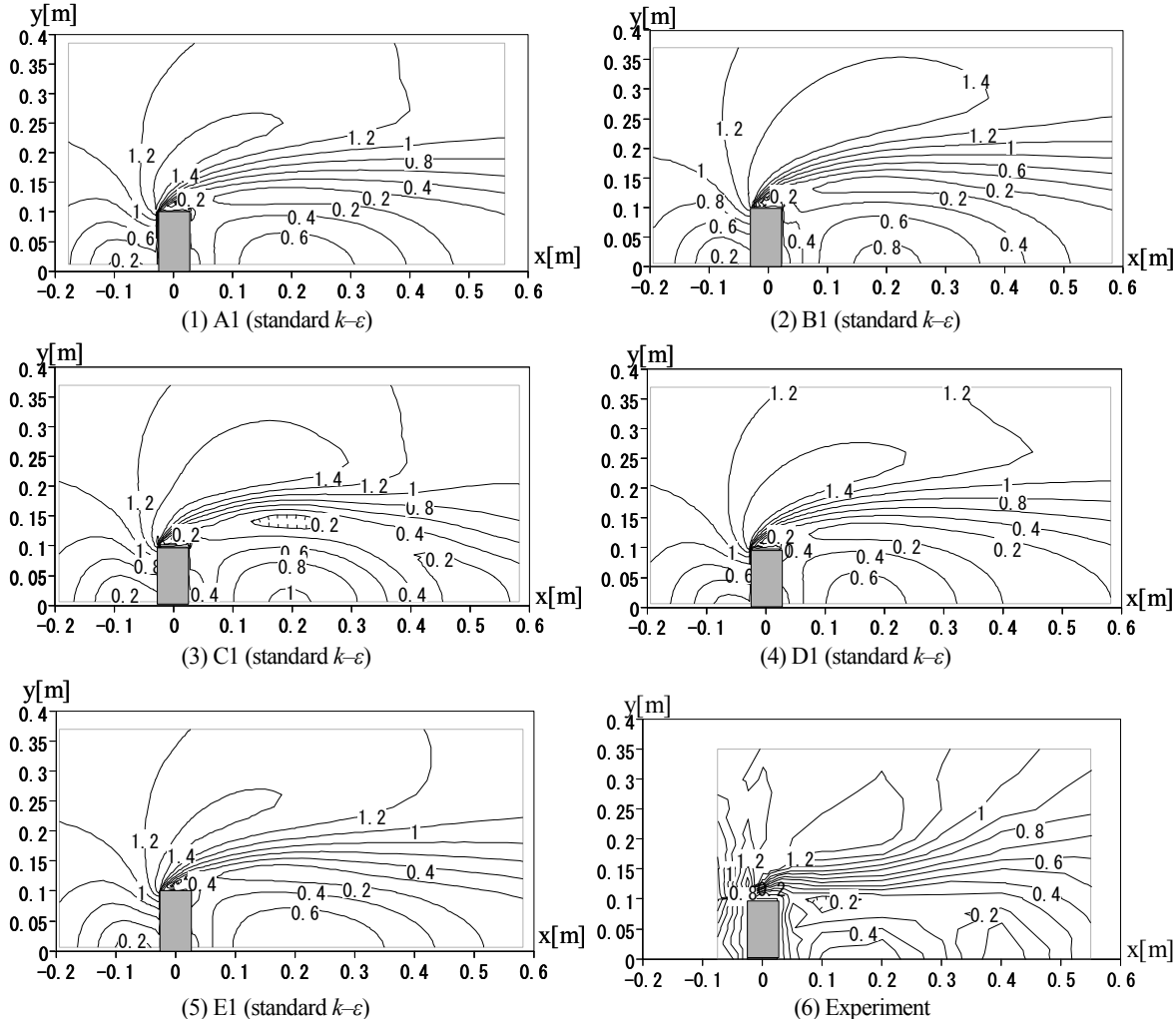


Figure 2-3-15. Comparison of standard $k-\varepsilon$ models (wind speed ratio near ground surface ($z = 0.0125 \text{ m}$))

b) Comparison of standard $k-\varepsilon$ model with modified $k-\varepsilon$ models (Figure 2-3-16)

When a comparison is performed with different turbulence models in the same code, the modified $k-\varepsilon$ models, excluding the Durbin model (C2) and ANK model (D4), predicted the region enclosed by the contour line of 1.4 to be larger at the side of the building than did the standard $k-\varepsilon$ model (A1->A2-A3, B1->B2, D1->D2-D3, E1->E2). In the LES results (Figure 2-3-16 (14)), the distributions are very similar to those of the experiment.

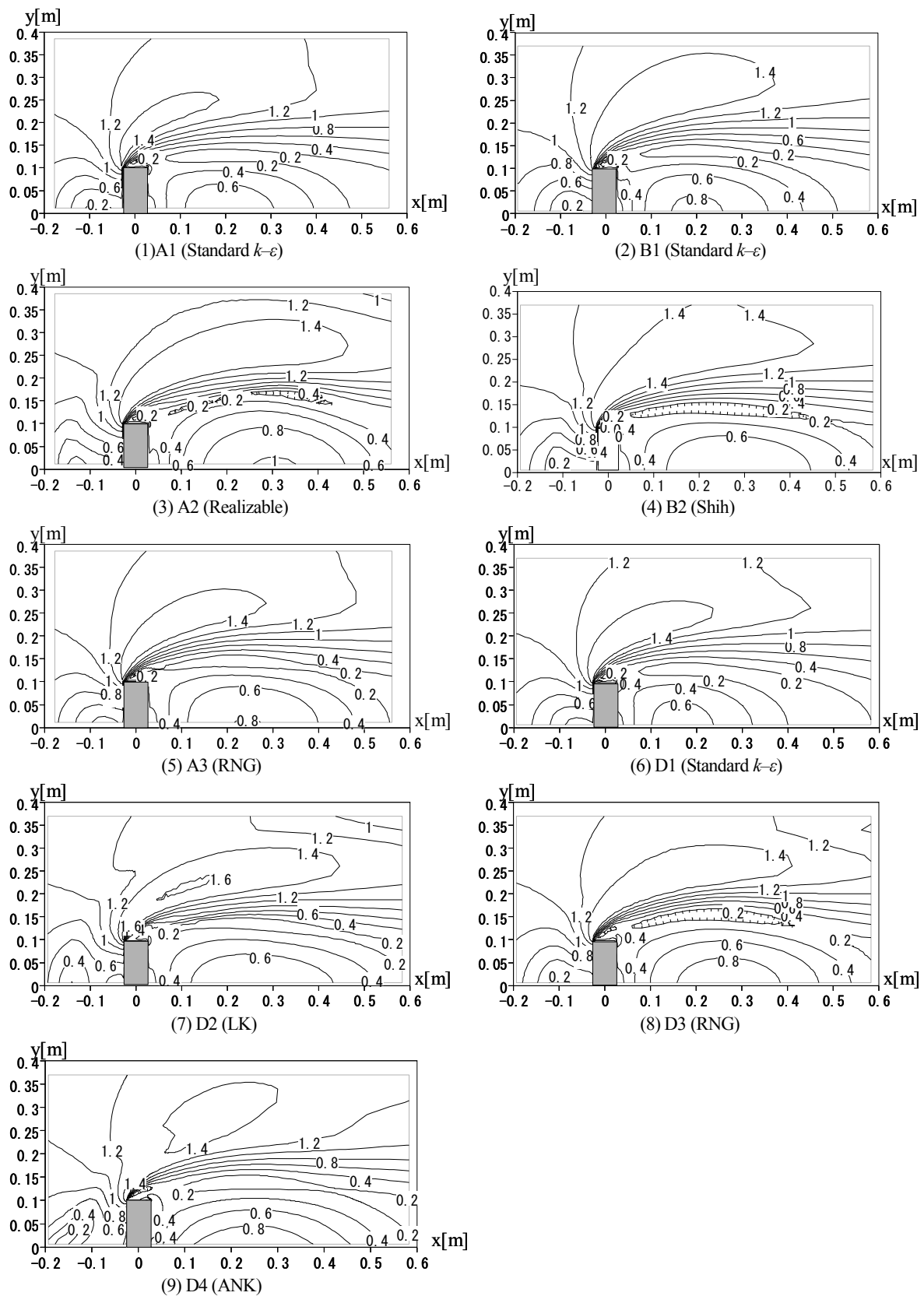


Figure 2-3-16 (1). Comparison of standard $k-\varepsilon$ models with modified $k-\varepsilon$ models (wind speed ratio near ground surface ($z = 0.0125$ m))

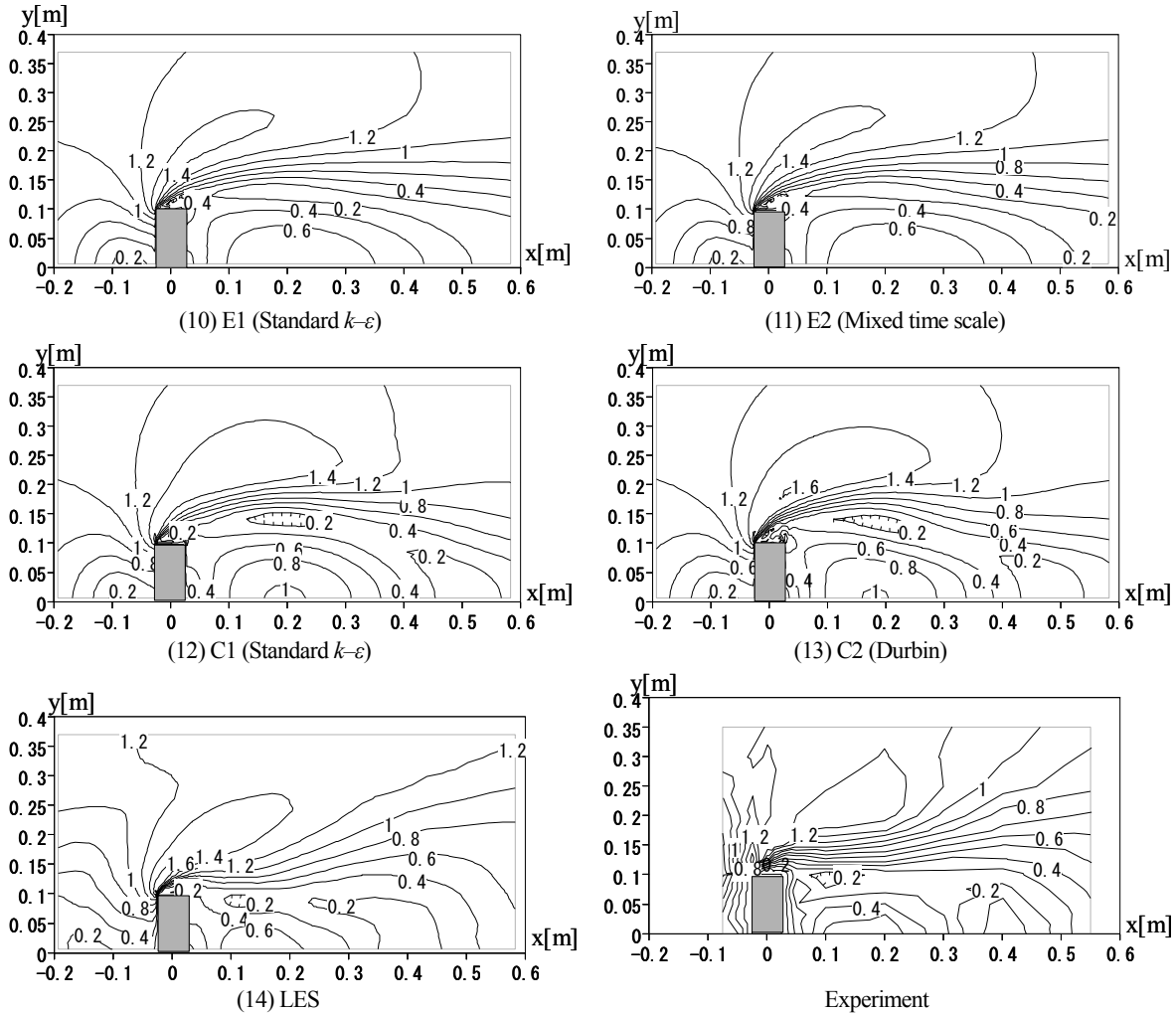


Figure 2-3-16(2). Comparison of standard $k-\varepsilon$ models with modified $k-\varepsilon$ models (wind speed increase ratio near ground surface ($z = 0.0125$ m))

2.3.3.4 Comparison of wind speed ratios at each measuring point

Figure 2-3-17 compares the experimental and calculated values of the wind speed ratios shown in Figure 2-3-15 and 2-3-16 for each measuring point. Overall, the tendency seen in the wind tunnel experiment was reproduced in the calculation results. However, in the region where the wind speed ratio exceeds 1.0, the calculated values tend to be larger than the experimental values. In the region with a relatively small wind speed ratio (<1.0), there is a wide range between the models. In the case of the modified $k-\varepsilon$ models in particular, the correspondence with the experimental values is poor. As explained above, this is because the reverse flow behind the building estimated by the modified $k-\varepsilon$ model is larger than that estimated by the standard $k-\varepsilon$ model. Focusing on strong wind regions where the wind speed ratio exceeds 1.0, no significant differences are observed in the comparison of the standard $k-\varepsilon$ and modified $k-\varepsilon$ models using the same CFD code. LES slightly overestimates the overall velocity value, but it corresponds more closely to the experimental results than the values estimated by the $k-\varepsilon$ models.

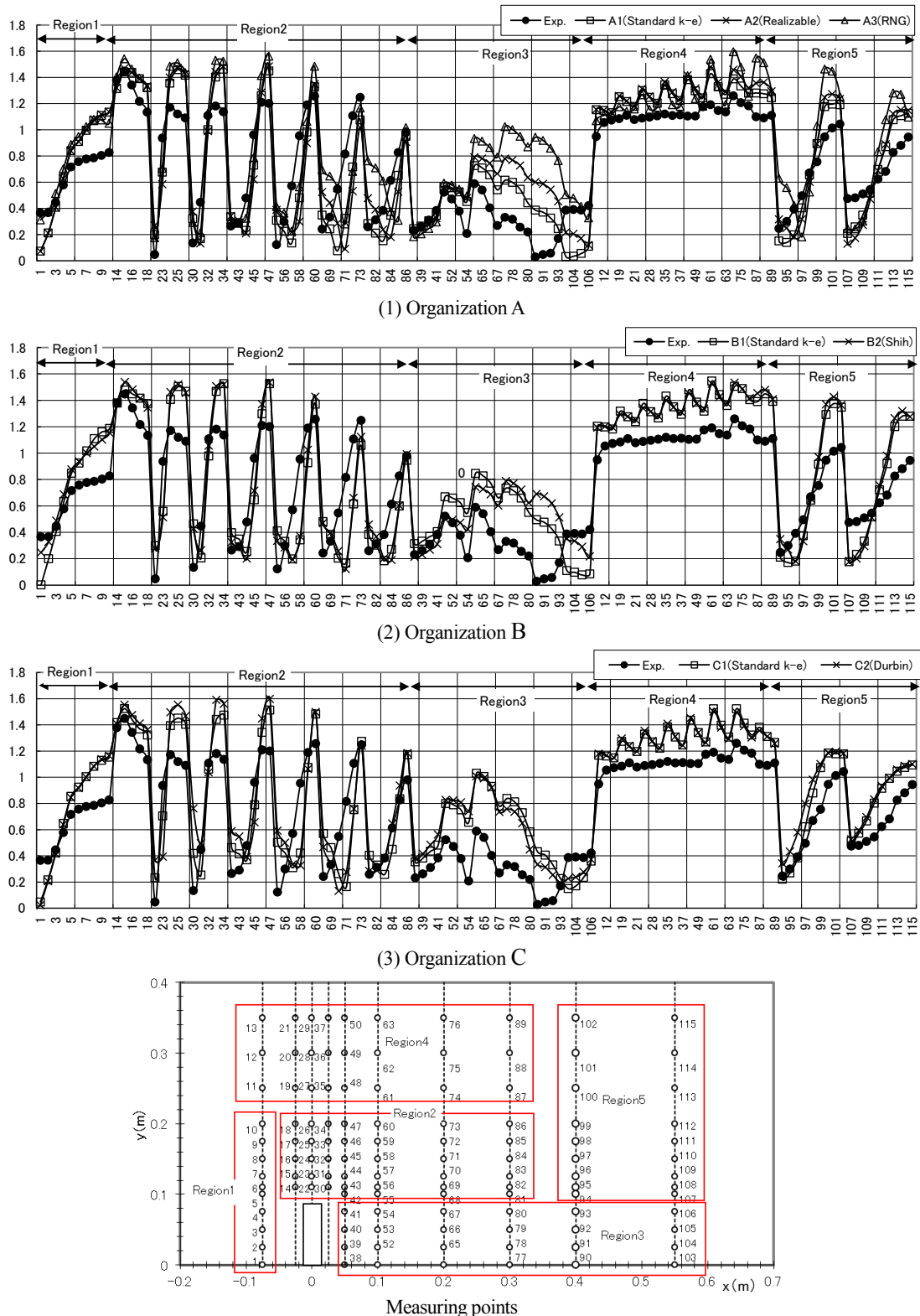


Figure 2-3-17(1). Comparison of wind speed ratios at each measuring point

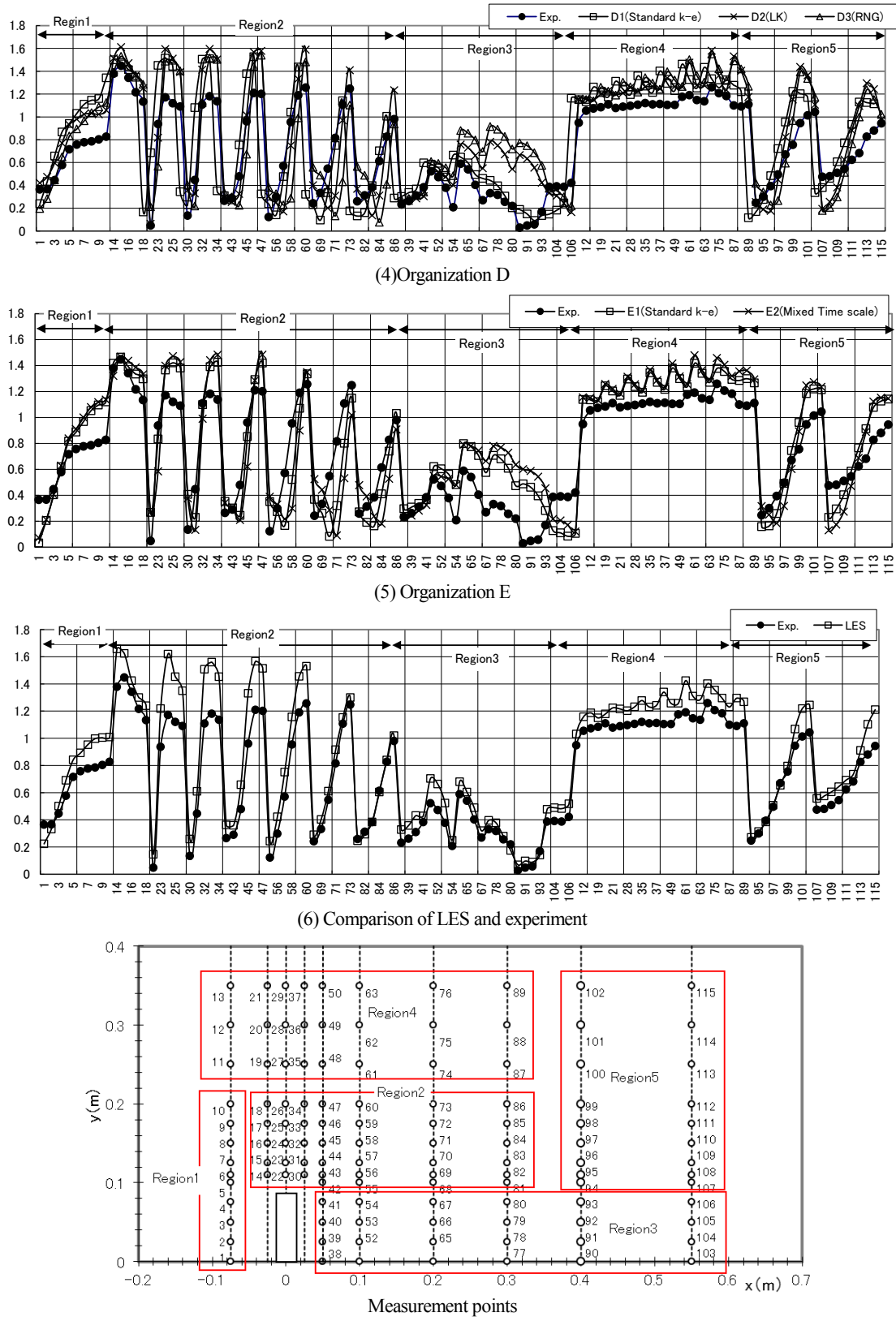


Figure 2-3-17(2). Comparison of wind speed ratios at each measurement point

2.3.3.5 Comparison between CFD codes

Figure 2-3-18 shows comparisons of the wind speed ratios obtained with the different CFD codes shown in Figures 2-3-15 and 2-3-16 using scatter plots. The turbulence models are all the standard $k-\varepsilon$ models. The correlation coefficients are 0.9 or higher. These comparisons suggest that if the basic calculation conditions, such as those used in the present study, are the same, very high correlations between the calculation results for different CFD codes can be obtained.

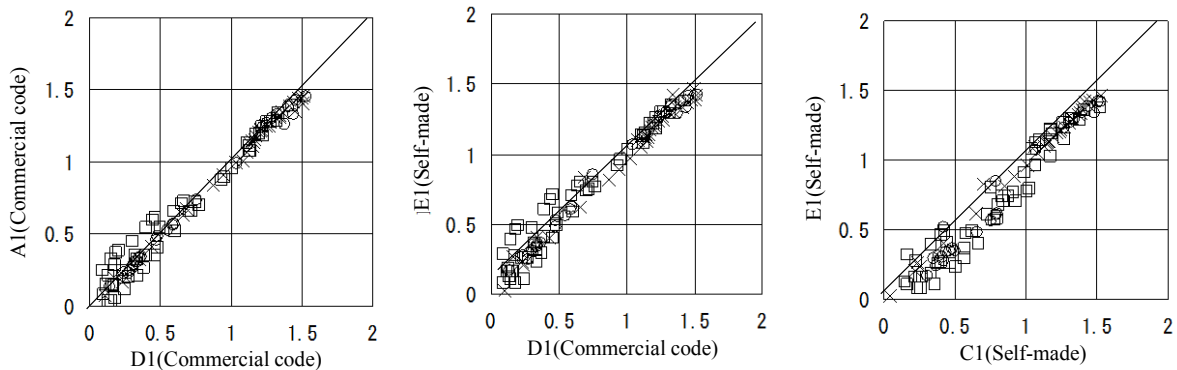


Figure 2-3-18. Correlation of normalized velocity values predicted by different codes (standard $k-\varepsilon$)

2.3.3.6 Comparison of velocity components on side surfaces of building

Figure 2-3-19 shows the velocity components and scalar velocity on the side of the building in the calculation results obtained by organization D. The values are normalized by the inflow velocity at the same height (3.11 m/s). The scalar velocity of the experiment shows a peak at approximately $y = 0.15$, and the values decrease slightly further from the building side (Figure 2-1-19 (1)). For all the models, the peak value is higher than the experimental value, and the velocities are overestimated. In the experiment, the $\langle u \rangle$ component has a peak near $y = 0.15$, like the scalar velocity, but the value increases with the distance from the building and then decreases again. This tendency is not completely reproduced by the standard $k-\varepsilon$ model, but it is reproduced by all the modified $k-\varepsilon$ models. The distribution of D2 (LK) is closest to that obtained in the experiment. On the other hand, the $\langle v \rangle$ component exhibits trends similar to those of the $\langle u \rangle$ component for all the models, but the peak values differ from those in the experiment. For the modified $k-\varepsilon$ models, the locations of the peak values are a little far from the building. Thus, they correspond closely with the results of the experiment below approximately $y = 0.20$. For the $\langle w \rangle$ component, the descending flow, which is observed below $y = 0.20$ in the experiment, is not reproduced by the standard $k-\varepsilon$ model. However, in the case of the modified $k-\varepsilon$ models, the descending flow is accurately reproduced, and the D3 (RNG) and D4 (ANK) results correspond particularly well with the experimental results. As demonstrated here, when the scalar velocity is compared, the differences between the modified $k-\varepsilon$ models and standard $k-\varepsilon$ model are relatively small. However, a detailed comparison confirms that the modified $k-\varepsilon$ models more accurately reproduce the structure of the flow field of the strong wind region.

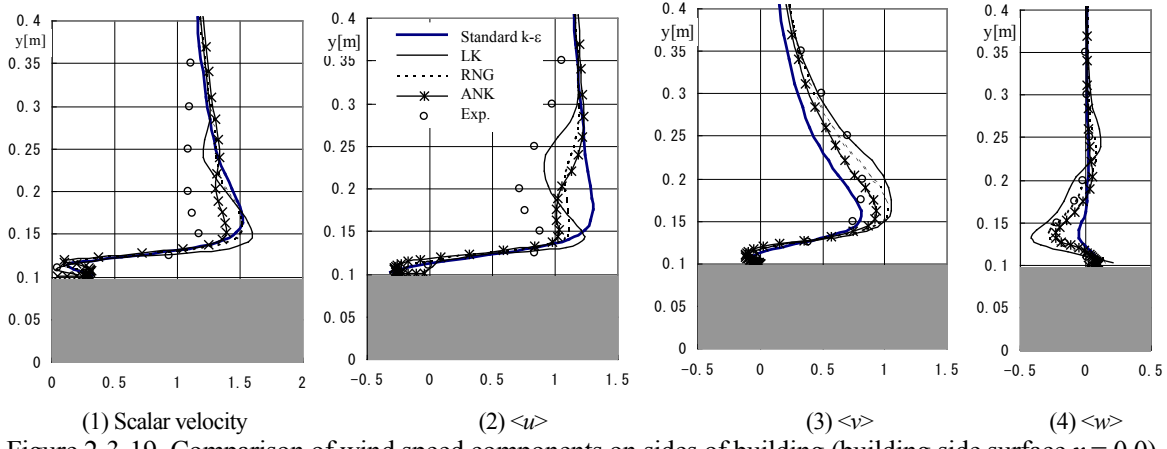


Figure 2-3-19. Comparison of wind speed components on sides of building (building side surface $x = 0.0$)

2.3.4 Summary of the analysis of flow around a high-rise building with a 4:4:1 shape

- A benchmark test was performed to analyze the flow around a 4:4:1 building model placed in a boundary layer flow, with conformance to the basic calculation conditions, such as the grid discretization and the computational domain, to the greatest extent possible.
- Variation of the grid discretization and boundary conditions showed that the effects of these conditions were small and that the basic conditions proposed in this study were appropriate.
- When the basic conditions were used, the calculation results obtained using different CFD codes were highly correlated.
- The modified $k-\epsilon$ models more accurately reproduced the structure of the flow field of the strong wind region at the side surfaces of the building than the standard $k-\epsilon$ model. However, there were still problems with the reproducibility of the recirculating flow region behind the building, as illustrated in the case of the 2:1:1 building.
- In the case of LES, the prediction accuracy was far greater than for all of the $k-\epsilon$ models that were compared.

2.4 Summary of the benchmark tests of flow around a single-building model

- If the modified $k-\epsilon$ models such as Launder & Kato (LK) model are used, the reverse flow on the roof is well reproduced and the prediction accuracy of the separation region near the ground surface is somewhat improved. However, in the wake region of the building, the reattachment length tends to be longer and the correspondence with the experiment becomes worse than in the standard $k-\epsilon$ model case.
- The calculation results obtained with a finer grid that was 1/2 of the basic calculation grid width conformed almost perfectly with the results obtained with the basic grid. Therefore, the grid discretizing level used in the basic grid is sufficient.
- Even if the basic domain ($21b \times 13.75b \times 11.25b$ in the 2:1:1 building case) is narrowed ($13.8b \times 7.56b \times 7.75b$ in the 2:1:1 building case), the results are almost unchanged.
- If inappropriate inflow values are given for k and ϵ , the calculation results can vary greatly. Thus, it is important to base the calculations on appropriate values.
- If the first-order upwind scheme is used for the advection term, the velocity distribution is predicted inaccurately because of pseudo-diffusion in regions where the wind flows into the cells diagonally, such as the separation

region. Therefore, the use of this scheme is not recommended.

- A benchmark test performed with equivalent calculation conditions yielded small differences in the calculation results using three commercial CFD codes and two self-developed CFD codes.
- LES greatly improves the prediction accuracy of the flow field behind the building. This is assumed to be a result of the ability of LES to reproduce periodic fluctuations behind the building. In addition, it is very important for the LES analysis to be conducted using an appropriate value for the inflow turbulence.

3. Benchmark tests of flow around building group models

3.1 Flow around a simple building group model

3.1.1 Introduction

The previous chapter dealt with single building models. In this chapter, building group models consisting of nine cuboids are considered as a test case in which the central building height and wind direction are changed.

3.1.2 Outline of wind tunnel experiment [4]

A wind tunnel experiment was performed using the Gettigen-type wind tunnel (measurement section: $1.8\text{ m} \times 3.0\text{ m}$) at the technical center of the Fujita Corporation. The focus of the experiment was on the flow around a building group consisting of a total of nine cuboid buildings installed in a boundary layer flow (one central building and eight surrounding buildings) (see Figure 3-1-1). The building model was a cuboid with a side length D of 0.2 m. The average velocity of the approaching flow at building height D was set to $U_H = 3.65\text{ m/s}$. The Re number based on U_H and D was 52,000.

Table 3-1-1 lists the cases investigated. Three shapes were used for the central building: [no building], $[D(x) \times D(y) \times D(z)]$, and $[D(x) \times D(y) \times 2D(z)]$. Three wind directions were used for each case: 0° , 22.5° , and 45° . The wind speeds at the measurement points shown in Figure 3-1-1 (a total of 120 points, measurement height: $0.1D$) were measured by thermistor anemometry (with a sampling interval of 1 Hz and a sampling time of 30 s). The exponent of the vertical profile of the approaching flow was approximately 0.28, and the turbulence intensity at height D was approximately 0.2.

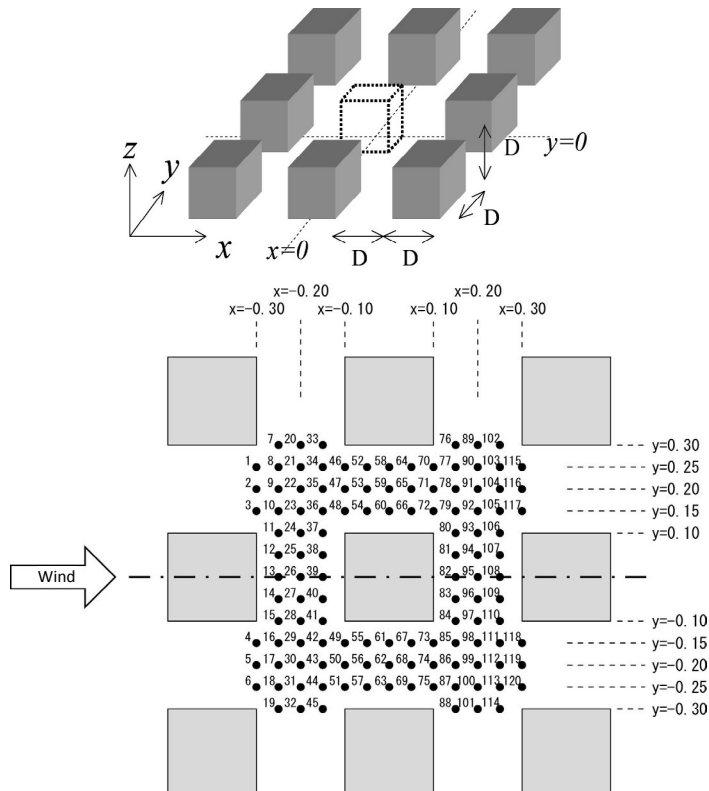


Figure 3-1-1. Simple city block model and measuring points

Table 3-1-1. Computed cases

No.	Center building	Wind direction
1	No building	0°
2	No building	22.5°
3	No building	45°
4	D x D x D	0°
5	D x D x D	22.5°
6	D x D x D	45°
7	2D x D x D	0°
8	2D x D x D	22.5°
9	2D x D x D	45°

3.1.3 Calculation conditions

3.1.3.1 Computational domain

For a wind direction of 0°, the computational domain of the basic conditions has the same cross section as the experimental wind tunnel in the vertical (z) and lateral (y) directions. The distance from the top of the building to the top boundary was 1.6 m (= 8.0D) in the vertical direction (z). The distance from the side of the building to the side boundary was 1.0 m (= 5.0D) in the lateral direction (y). (In the case of steady-state analysis, the computational domain can be narrowed by half because of symmetry about the central axis of the building). The distance (x) from the windward surface of the building to the inflow boundary was 0.5 m (= 2.5D) on the windward side, and that from the downwind side of the building to the outflow boundary was 1.0 m (= 5.0D) on the downwind side in the streamwise direction.

For wind directions of 22.5° and 45°, the ratio of the projected area of the buildings to the cross section of the computational domain normal to the flow direction was set to be almost identical to that in the case of the wind direction of 0°.

3.1.3.2 Inflow boundary

Figure 3-1-2 shows the inflow boundary conditions. The time-averaged velocity $\langle u_1 \rangle$ and turbulent kinetic energy k were set to be in agreement with the wind tunnel experiment values (k was estimated from the measurement results for the turbulence intensity in the x direction), and ε was calculated by assuming that $P_k = \varepsilon$ for the inflow boundary condition.

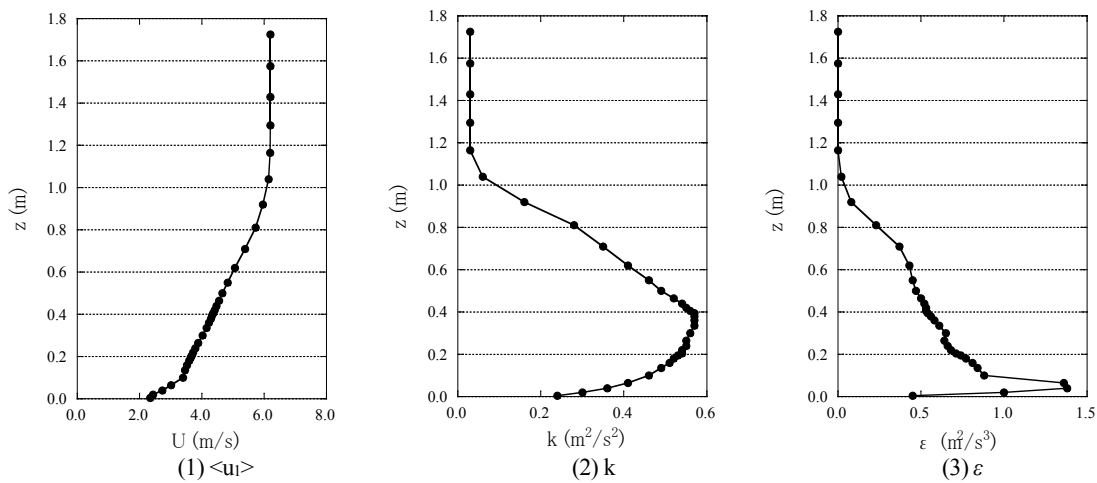


Figure 3-1-2. Inflow boundary conditions

3.1.3.3 Ground surface speed boundary

The z_0 type logarithmic law ($z_0 = 4.5 \times 10^{-4}$ [m]) was used.

3.1.3.4 Grid discretization

The grid for the basic condition was $68(x) \times 72(y) \times 34(z)$. The width of the first cell on the floor surface was 0.01 m (= 0.05D), and the grid width on the building wall surface was also 0.01 m (= 0.05D). For reference, Figure 3-1-3 shows the computational domain and grid discretization used by organization D.

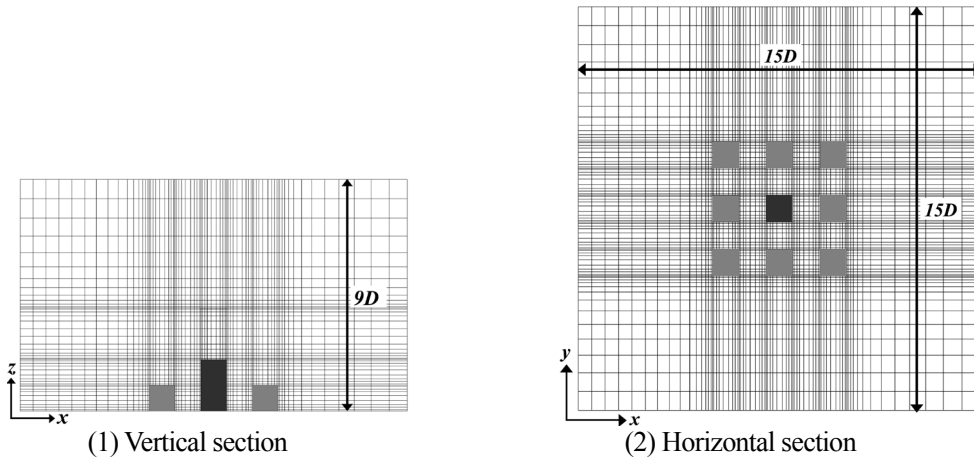


Figure 3-1-3. Example of computational domain and grid discretization (organization D)

3.1.4 Analysis results

Table 3-1-2 lists the analysis cases for the CFD simulations conducted. The turbulence model used was the standard $k-\varepsilon$ model, except for the nonlinear modified $k-\varepsilon$ model of Shih et al. [25], used by organization B. Figure 3-1-4 shows the contours of the wind speed ratio around the central building obtained in the wind tunnel experiment. The wind speed ratio used here is the velocity increase ratio obtained by standardizing the wind speeds at each measurement point by the inflow velocity at the same height ($z = 0.1D$). Figure 3-1-5 shows the contours of the wind speed ratio for the numerical simulation conducted by organization A. In general, the predicted velocities were lower than that measured in the experiment.

Table 3-1-2. Analysis cases

Organization	Software	Wind direction	Turbulence model
A	Self-made	0°	Standard $k-\varepsilon$
		22.5°	Standard $k-\varepsilon$
		45°	Standard $k-\varepsilon$
B	STAR-CD	0°	Standard $k-\varepsilon$
		0°	Modified $k-\varepsilon$
C	STREAM	0°	Standard $k-\varepsilon$
		22.5°	Standard $k-\varepsilon$
		45°	Standard $k-\varepsilon$
D	FLUENT	0°	Standard $k-\varepsilon$
		22.5°	Standard $k-\varepsilon$
		45°	Standard $k-\varepsilon$

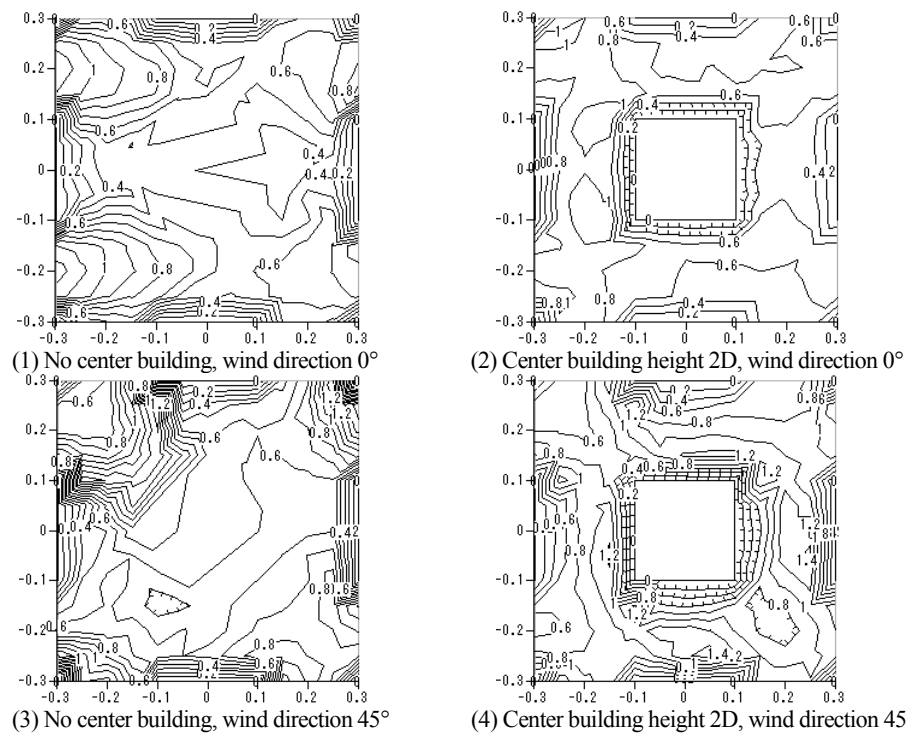


Figure 3-1-4. Contours of wind speed ratio around center building (wind tunnel experiment)

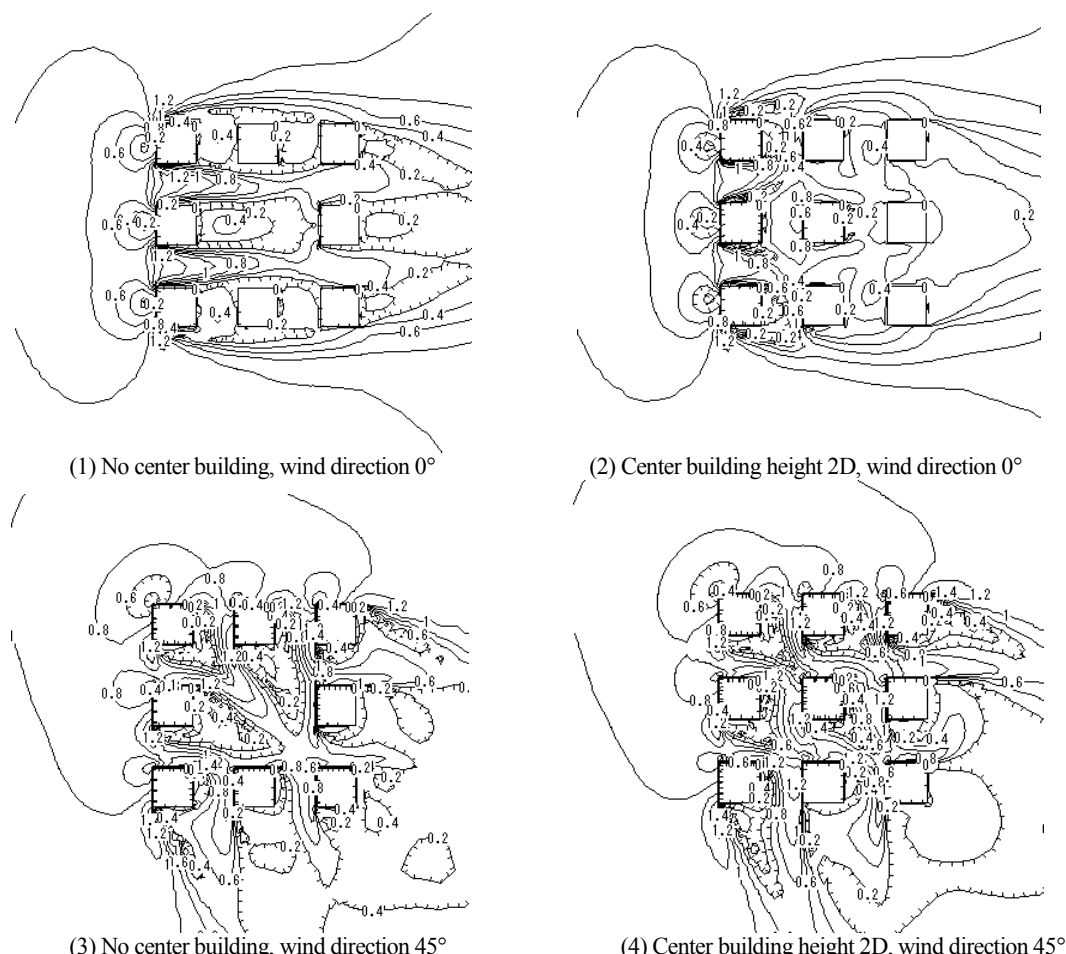


Figure 3-1-5. Contours of wind speed ratio around building group (CFD, organization A)

3.1.4.1 Effect of height of central building

Figure 3-1-6 shows the correlation between the experimental and calculation results obtained by organization A in the case of a wind direction of 0° , along with a comparison of the wind speed ratios obtained for each measurement point obtained. The correlation coefficient and the standard error are denoted as C.C. and S.E., respectively. Overall, the calculated wind velocity ratios are lower than those obtained in the wind tunnel experiment. This tendency is remarkable in the case in which the central building height is $2D$. Even if the center building height is varied, the correlation coefficient does not change very much, but there is a tendency for the standard error to be larger for a greater center building height.

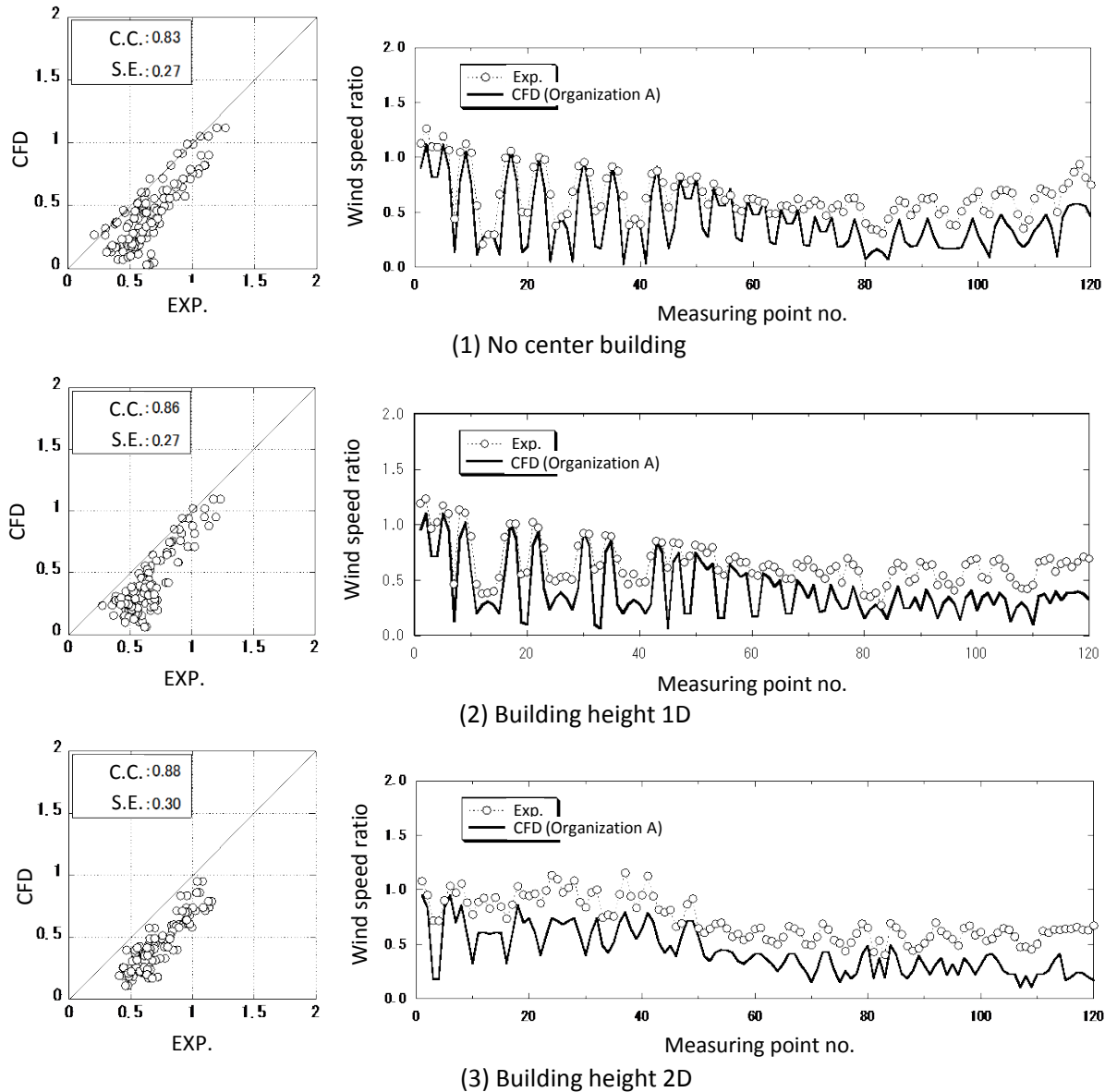


Figure 3-1-6. Correlation of experimental and calculation results and comparison of wind speed ratios at each measurement point (impact of center building height)

3.1.4.2 Effect of wind direction

Figure 3-1-7 shows a comparison between the experimental results and calculation results for organization A for wind directions of 0° , 22.5° , and 45° for the case in which the central building height is $2D$. As the wind direction increases, the large wind velocity region is well reproduced and the correlation improves. The other organizations obtained similar results. This is a result of the shortcoming of the standard $k-\epsilon$ model described earlier becoming inconspicuous because the separation flow at the windward corners weakens for a wind direction of 45° .

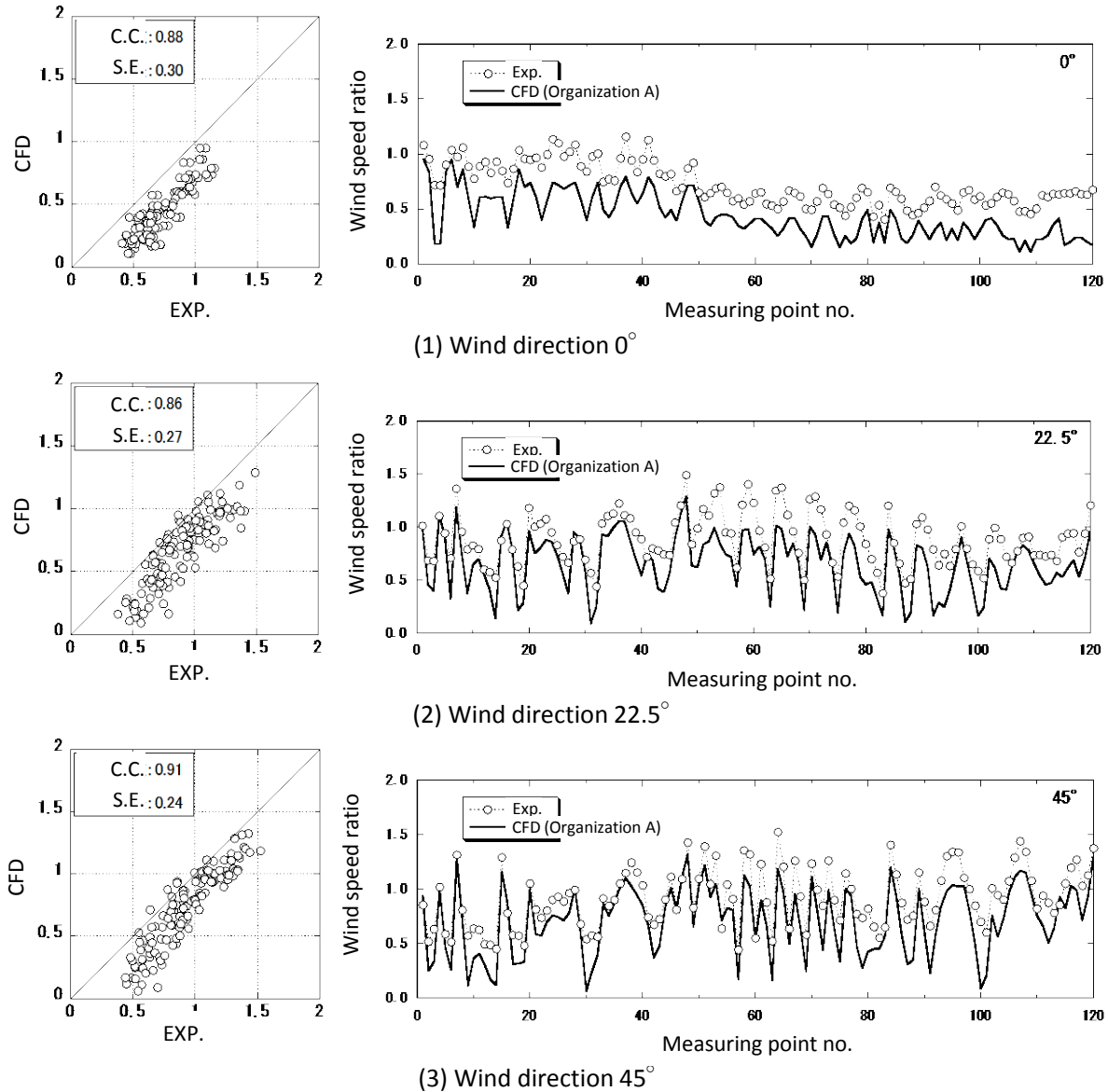


Figure 3-1-7. Correlation of experimental and calculation results and comparison of wind speed ratios at each measurement point (effect of wind direction)

3.1.4.3 Effect of turbulence model

Figure 3-1-8 shows a comparison of the wind speed ratios according to the experiment and the calculation results obtained by organization B using two different turbulence models, i.e., the standard $k-\epsilon$ model and Shih's modified $k-\epsilon$ model, for the case in which the center building height is $2D$ and the wind direction is 0° . The modified $k-\epsilon$ model more accurately reproduces the wind tunnel experiment results in the high-velocity region, but its impact was very limited.

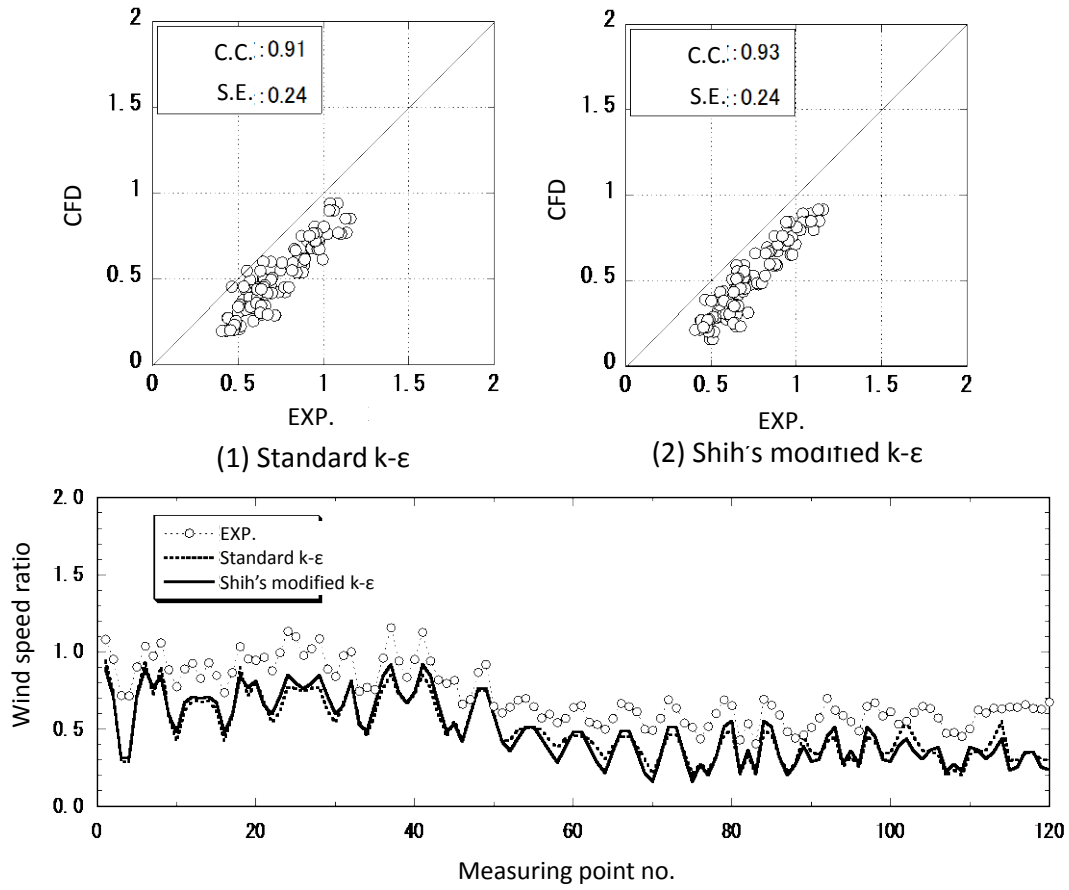


Figure 3-1-8. Correlation of experimental and calculation results and comparison of wind speed ratios at measurement points (effect of turbulence model)

3.1.4.4 Correction of calculated results

The value measured with a thermistor anemometer in a wind tunnel experiment is the average of the instantaneous values of the scalar velocity. The time-averaged scalar velocity is expressed as shown in eq. (3.1.1). The instantaneous values are represented by u , v , and w ; the average values are represented by $\langle u \rangle$, $\langle v \rangle$, and $\langle w \rangle$; the fluctuating values are represented by $u' = u - \langle u \rangle$, $v' = v - \langle v \rangle$, and $w' = w - \langle w \rangle$; and the turbulent kinetic energy is represented by k :

$$\begin{aligned} \langle (u^2 + v^2 + w^2)^{1/2} \rangle &= \langle \{(\langle u \rangle + u')^2 + (\langle v \rangle + v')^2 + (\langle w \rangle + w')^2\}^{1/2} \rangle \\ &= \langle (\langle u \rangle^2 + \langle v \rangle^2 + \langle w \rangle^2 + u'^2 + v'^2 + w'^2)^{1/2} \rangle \\ &= (\underbrace{\langle u \rangle^2 + \langle v \rangle^2 + \langle w \rangle^2 + 2k}_{})^{1/2} \end{aligned} \quad (3.1.1)$$

On the other hand, the time-averaged scalar velocity obtained from a steady-state RANS model, such as the $k-\epsilon$ model, is the scalar velocity obtained from the time-averaged velocities of each component, i.e.:

$$\langle u^2 + v^2 + w^2 \rangle^{1/2} \quad (3.1.2)$$

Eq. (3.1.2) corresponds to the underlined part of eq. (3.1.1). This means that the value within $()^{1/2}$ is $2k$ lower than in eq. (3.1.2). This difference causes a large discrepancy in the region with a low mean velocity and large turbulent fluctuation. Thus, utilizing the average value of the velocity components and k obtained by CFD, the average value of the scalar velocity is corrected using eq. (3.1.1). An improvement in the correspondence with the experimental results in the flow region in the wake of the building is expected.

Figure 3-1-9 shows a comparison between the experiment and corrected calculation results obtained by organization B for the case in which the center building height is $2D$, the wind direction is 0° , and the standard $k-\varepsilon$ model is used. This is one method of accurately comparing the experimental results obtained by measurement using a thermistor anemometer (the averaged value of the instantaneous scalar velocity) and the CFD results (the scalar velocity obtained from the averaged vector components). In general, the calculated values increase after correction, and the correspondence with the experimental values is improved.

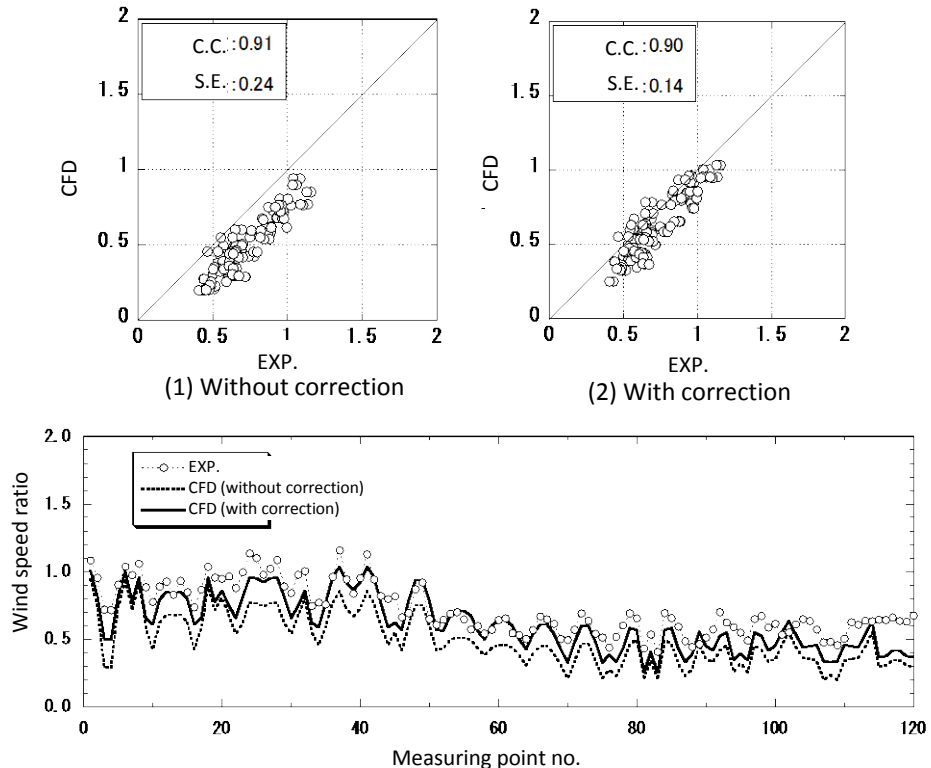
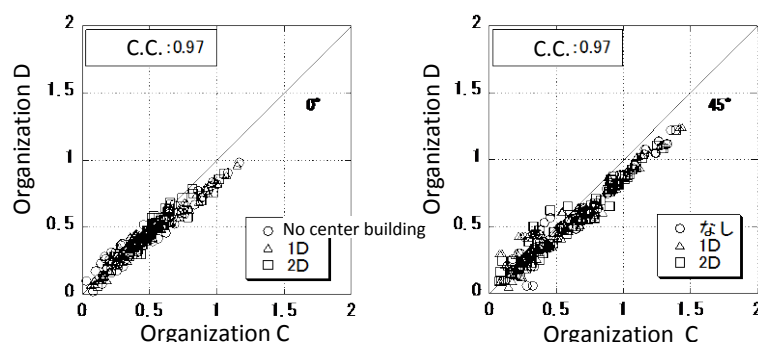


Figure 3-1-9. Correlation of experimental and calculation values and comparison of wind speed ratios at each measurement point (corrected calculation values)

3.1.4.5 Comparison of calculation results by different codes

Figure 3-1-10 shows the correlations between the calculations obtained for the cases of wind directions of 0° and 45° by organizations C and D. Both sets of results correspond well for both wind directions and all center building heights. This confirms that if the analysis conditions conform to those used in this study, a high correlation between the results obtained using different codes can be expected.



3.1.4.6 Effect of calculation grid

Figure 3-1-11 shows the correlation of the results obtained by organization C for the basic and finer grids for the case of a center building of height 2D and a wind direction of 0° . The two sets of calculation results are almost identical and confirm that the grid size used in this study is appropriate. In the high-velocity region, the velocities obtained using the finer grid are slightly higher and a bit closer to the wind tunnel experiment values.

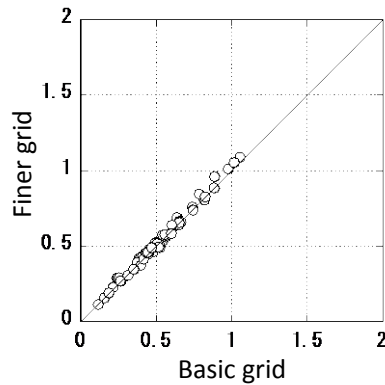


Figure 3-1-11. Impact of calculation grid

3.1.4.7 Overview of correlation coefficients and standard errors

Table 3-1-3 lists the correlation coefficients and standard errors of the results obtained by this benchmark test.

Table 3-1-3. Comparison of correlation coefficients (C.C.) and standard errors (S.E.)

Organization	Software	Wind direction	Turbulence model	No center building		Center building 1D		Center building 2D	
				C.C.	S.E.	C.C.	S.E.	C.C.	S.E.
A	Self-made	0°	Standard $k-\epsilon$	0.83	0.27	0.86	0.27	0.88	0.30
		22.5°	Standard $k-\epsilon$	0.89	0.23	0.89	0.24	0.86	0.27
		45°	Standard $k-\epsilon$	0.91	0.22	0.87	0.29	0.91	0.24
B	STAR-CD	0°	Standard $k-\epsilon$	0.87	0.23	0.85	0.24	0.91	0.24
		0°	Modified $k-\epsilon$	0.90	0.20	0.90	0.22	0.93	0.24
C	STREAM	0°	Standard $k-\epsilon$	0.85	0.22	0.85	0.22	0.76	0.23
		22.5°	Standard $k-\epsilon$	0.90	0.22	0.91	0.24	0.77	0.30
		45°	Standard $k-\epsilon$	0.92	0.22	0.90	0.30	0.93	0.26
D	FLUENT	0°	Standard $k-\epsilon$	0.90	0.23	0.86	0.24	0.83	0.26
		22.5°	Standard $k-\epsilon$	0.90	0.25	0.91	0.27	0.83	0.32
		45°	Standard $k-\epsilon$	0.94	0.25	0.88	0.35	0.91	0.33

3.1.5 Summary of the analysis of flow around a simple building group model

A benchmark test of a simple building group model was performed. The following information was obtained:

- The correlation coefficients of the wind speed ratio between the wind tunnel experiment and the calculation results ranged from 0.8 to 0.9.
 - The CFD calculations tended to underestimate the velocity. However, further investigation is necessary to identify a method for comparing the calculation results obtained by steady RANS with the experimental values obtained using thermistor anemometers.

- Using the modified $k-\varepsilon$ model improved the prediction accuracy in the high-velocity region, but its effect is limited.
- When analysis conditions conforming to those used in this study were used, the calculation results obtained using different codes were highly correlated.

3.2 Flow around a high-rise building in a multi-block model [43]

3.2.1 Outline of wind tunnel experiment

A wind tunnel experiment was conducted at the Niigata Institute of Technology. The model is illustrated in Figure 3-2-1 and Photo 3-2-1.

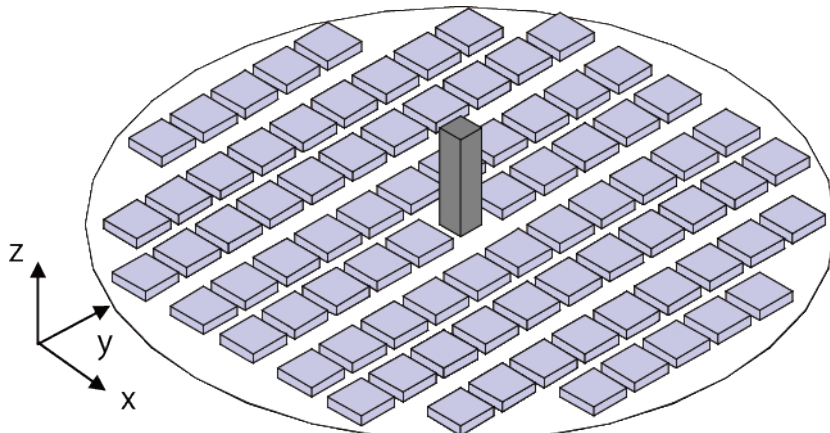


Figure 3-2-1. Outline of target model

The target model consisted of uniformly arranged city blocks with a plane shape of $40 \text{ m} \times 40 \text{ m}$, a 10-m height, and a $25 \text{ m} \times 25 \text{ m} \times 100 \text{ m}$ (1:1:4) high-rise building in the central block. Each block was composed of two 10-m-wide roads and roads of 20 m and 30 m. The scale of the multi-block model was 1/400. The inflow velocity at the central building height H , U_H , was 6.61 m/s.

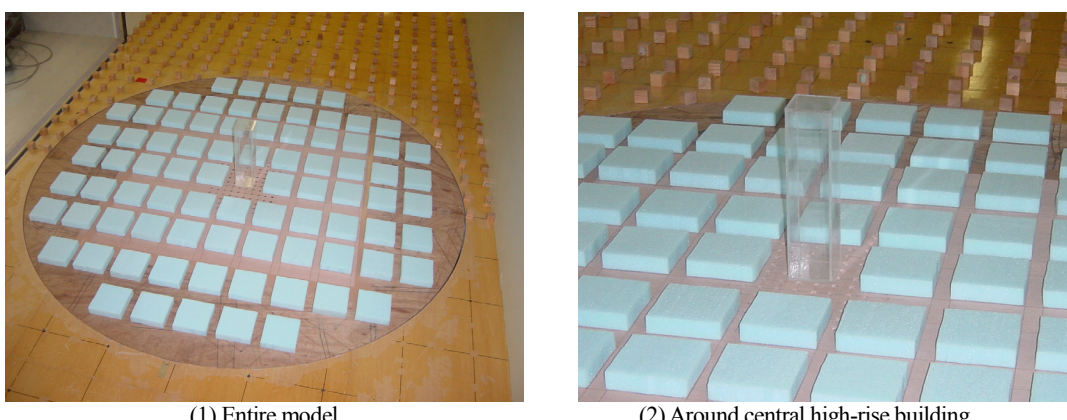


Photo 3-2-1. Target model

Measurements were performed for three wind directions (0° , 22.5° , 45°) using a thermistor anemometer (EXP_T). Measurements were also performed for the wind direction of 0° using a split fiber probe for each component (EXP_S). All measurement were obtained at a height 2 m above the ground in actual scale.

Table 3-2-1. Experimental cases

Case	Anemometer	Wind direction
EXP_T	Thermistor anemometer	0, 22.5, 45°
EXP_S	Split fiber probe	0°

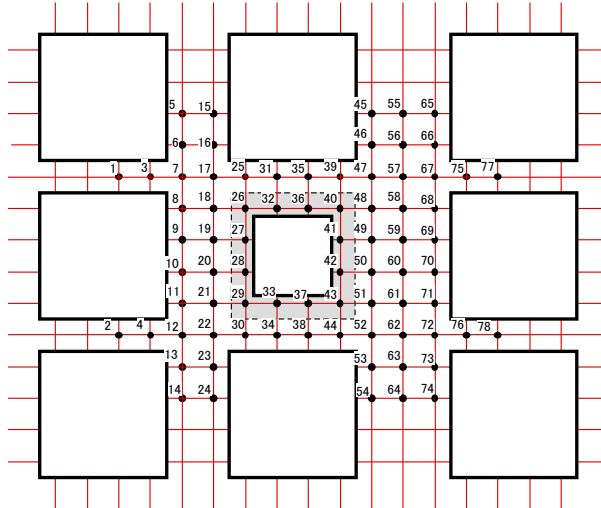


Figure 3-2-2. Measurement points

3.2.2 Results of wind tunnel experiments

Figure 3.2.3 shows the horizontal distribution of the wind velocity vectors obtained using the split fiber probe for the wind direction of 0° (EXP_S). The distribution reveals that a strong wind flow blows from the side of the central high-rise building into the wake of the building. On the road upwind of the building, the wind direction becomes opposite that of the incoming flow because of the influence of the central building.

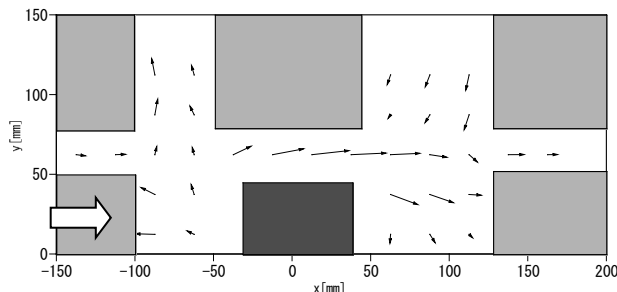


Figure 3-2-3. Horizontal distribution of velocity vectors obtained by EXP_S (wind direction 0°)

Figure 3.2.4(1) shows the results of a comparison of the scalar velocity values obtained for the three wind speed components measured using the split fiber probe (EXP_S) with the values measured using the thermistor anemometer for the wind direction of 0° (EXP_T). The EXP_T values are slightly higher in the low-velocity region in particular. This is assumed to be a result of the fact that when using a thermistor anemometer, the wind speed fluctuation component is also included in the average value of the scalar velocity, as explained in the previous section. On the other hand, when using the split fiber probe, the time-averaged velocity component and the fluctuation component are measured separately. Figure 3.2.4(2) shows a comparison of the scalar velocity corrected using the measured time-averaged velocity and turbulent kinetic energy k and the results obtained using the thermistor anemometer. Excluding two measurement points (nos. 49 and 59 in Figure 3-2-2), the correction achieves an overall

improvement in the correspondence between EXP_T and EXP_S. The large difference between these two points is a result of the extremely large experimental value of k at this point, which is caused by periodic fluctuation in the wake of the building. It is necessary to investigate the correction method further.

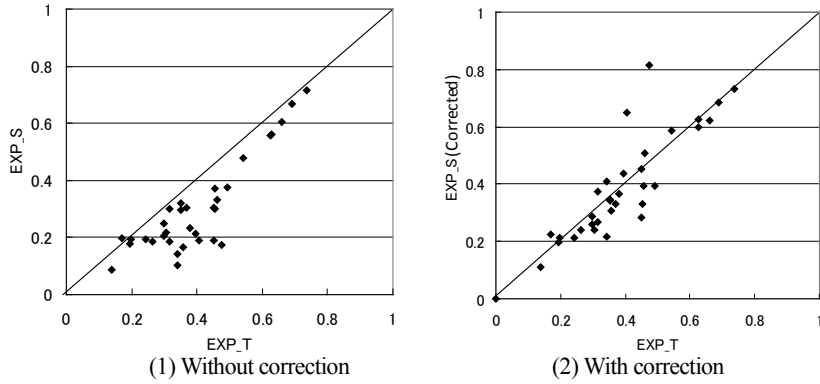


Figure 3-2-4. Comparison of scalar velocities obtained by two anemometers at wind direction of 0°

3.2.3 Calculation conditions

3.2.3.1 Study cases

Taking the wind direction of 0° as the basic case, analyses were performed for 0° , 22.5° , and 45° .

3.2.3.2 Computational domain

The experimental model was modeled within a circle with a diameter of 1.6 m ($= 6.4H$). The section of the wind tunnel used for the experiment was 1.8 m ($= 7.2H$) in the lateral (y) direction and 1.8 m ($= 7.2H$) in the height (z) direction. The computational domain was set to include the entire modeled geometry.

3.2.3.3 Grid discretization

The grid discretization near the ground was set so that a height 2 m above ground ($= 0.02H$) in actual scale was the third grid from the ground surface. The grids of the building shapes were generated based on computer-aided design (CAD) data.

3.2.3.4 Inflow boundary conditions

The mean velocity profile assumed was based on the roughness classification III recommended by AIJ [35]. The inflow boundary conditions for the wind tunnel experiment are listed in Table 3-2-2. Experimental values were interpolated for the CFD calculations. The values in the table were made dimensionless by normalization with respect to the model height H and inflow wind speed at this height U_H . The ε value is obtained by assuming that $P_k = \varepsilon$ at the inflow boundary.

3.2.3.5 Ground surface boundary conditions

In this case study, two types of ground surface boundary conditions were compared, i.e., a normal logarithmic law and a logarithmic law including z_0 . The value of z_0 in the logarithmic law was given as follows. Based on a value of 0.012 for k (normalized based on the inflow velocity at height H , U_H , which also applies to the following quantities) at the measurement point closest to the ground surface ($z/H = 0.02$):

$$u^* \equiv C_\mu^{1/4} \sqrt{k} = 0.09^{1/4} \sqrt{0.012} = 0.06 [-] \quad (3.2.1)$$

Substituting this value and the wind speed value $\langle u \rangle = 0.576 [-]$ at the height of the measurement point closest to the ground surface into the following logarithmic law:

$$\frac{\langle u(z) \rangle}{u_*} = \frac{1}{\kappa} \ln \frac{z}{z_0} \quad (3.2.2)$$

$$\ln \left(\frac{z}{z_0} \right) = \frac{0.576 \times 0.4}{0.06} = 3.84$$

$$\frac{z}{z_0} = \exp(3.84) = 46.525$$

z_0 is $0.02H / 46.525 = 4.3 \times 10^{-4} [-]$ (this value corresponds to $z_0 = 1.075 \times 10^{-4}$ [m] in the experimental scale and to $z_0 = 0.043$ [m] in the actual case).

Table 3-2-2. Inflow boundary conditions (normalized by H and U_H)

z/H	$\langle u(z) \rangle / U_K$	$k(z) / U_K^2$
0.02	0.576	0.0120
0.04	0.620	0.0137
0.08	0.650	0.0151
0.12	0.673	0.0151
0.20	0.713	0.0165
0.40	0.800	0.0170
0.80	0.945	0.0168
1.20	1.050	0.0157
1.60	1.135	0.0144
2.40	1.305	0.0103
3.20	1.432	0.0064
4.00	1.507	0.0028
4.80	1.514	0.0015

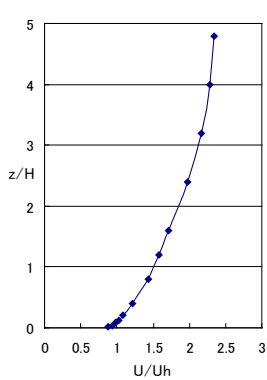


Figure 3-2-5. $\langle u \rangle$ at inflow boundary

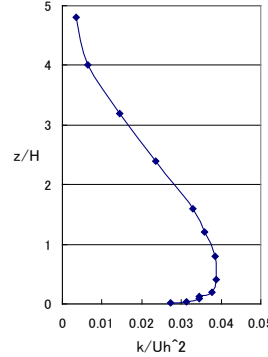


Figure 3-2-6. k at inflow boundary

3.2.4 Analysis cases

3.2.4.1 Analysis cases

Table 3-2-3 lists the analysis cases submitted.

Table 3-2-3. Analysis cases

Code	Case	Computational domain	Turbulence model	Ground surface condition
Code M	CFD_M1	6.4H (X) \times 6.4H (Y) \times 3.0H (Z) Basic	Standard $k-\epsilon$	Log law including z_0
	CFD_M2	9.6H (X) \times 9.6H (Y) \times 4.8H (Z)		

		Larger domain		
	CFD_M3	5.6H (X) \times 5.6 H (Y) \times 2.4H (Z) Smaller domain		
	CFD_M4	4.24H (X) \times 4.24H (Y) \times 2.0H (Z) Much smaller domain		
	CFD_M5	4.24H (X) \times 4.24H (Y) \times 2.0H (Z) Much smaller domain + surrounding buildings reduced		
Code T	CFD_T1	10.0H (X) \times 8.0H (Y) \times 4.0H (Z)	Standard $k-\varepsilon$	Log law including z_0
	CFD_T2		LK	
	CFD_T3		Standard $k-\varepsilon$	Generalized log law for smooth wall
Code O	CFD_O1	6.4H (X) \times 6.4H (Y) \times 7.2H (Z)	Standard $k-\varepsilon$	Log law including z_0
	CFD_O2		Standard $k-\varepsilon$	Generalized log law for smooth wall

3.2.4.2 Grid discretization used

Figure 3-2-7 shows an outline of the computational domain and grid discretization for each calculation case.

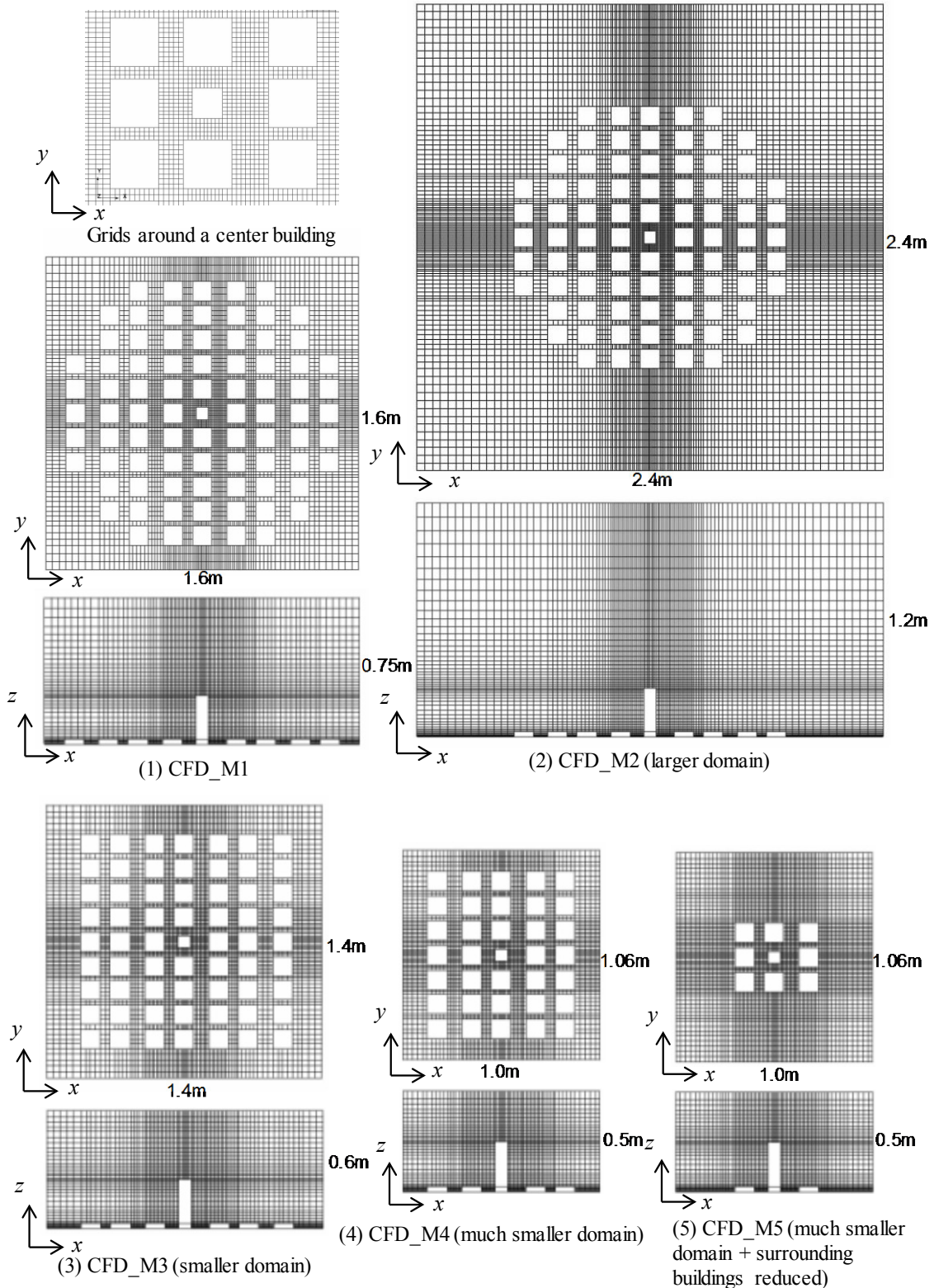


Figure 3-2-7. Computational domain and grid discretization (code M)

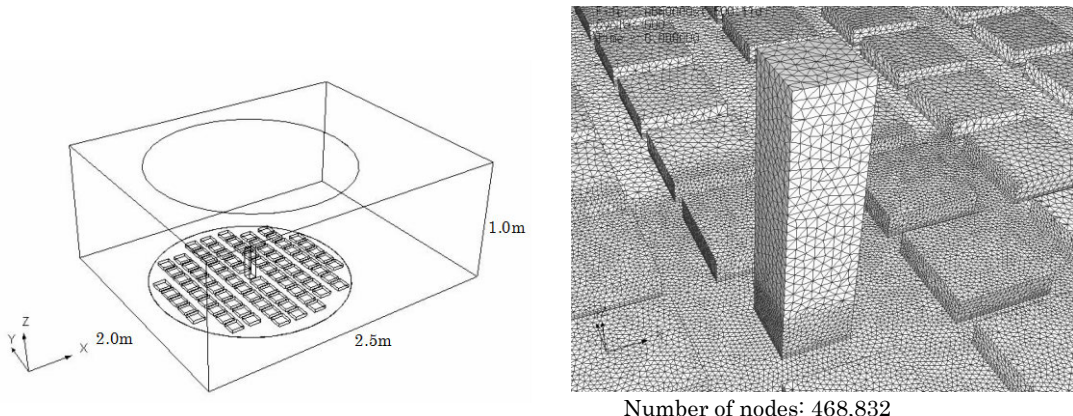
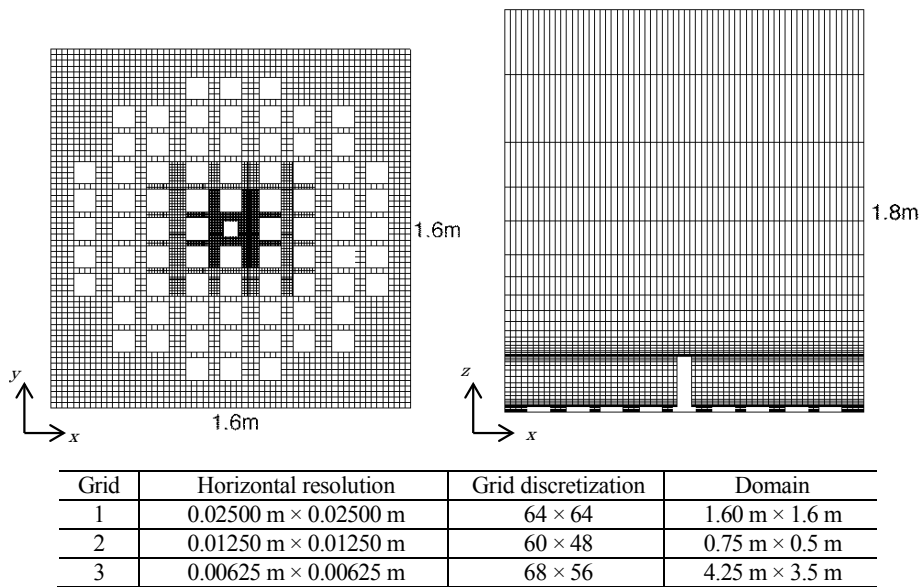


Figure 3-2-8.Computational domain and grid discretization (code T)



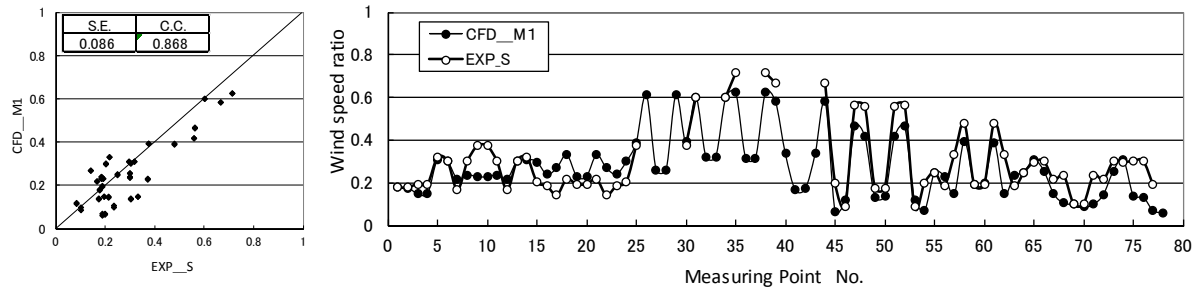
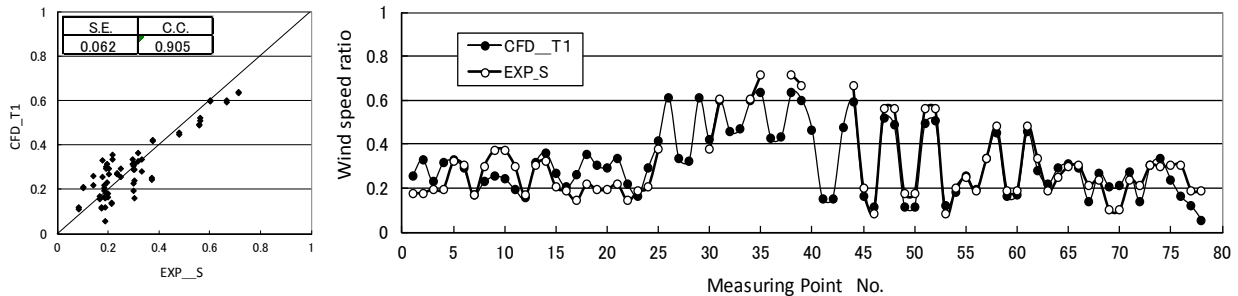
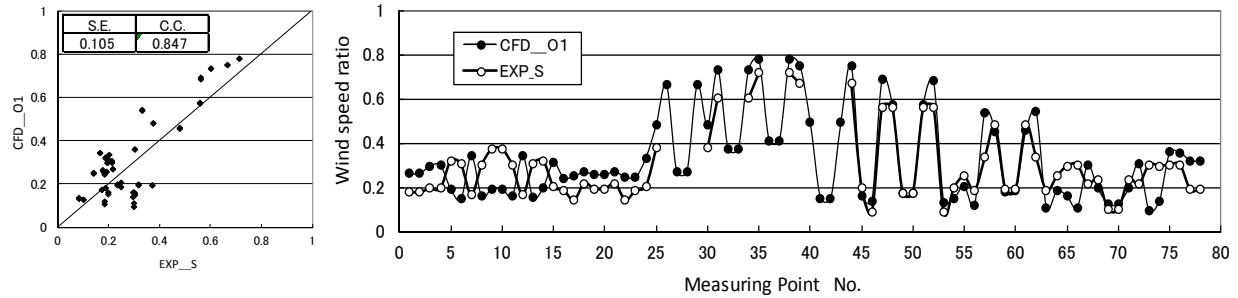
*Every grid has 46 grids per 1.8-m height in the vertical direction.

Figure 3-2-9. Computational domain and grid discretization (code O)

3.2.5 Comparison of analysis results

3.2.5.1 Comparison of results obtained by different CFD codes

Figures 3-2-10 to 3-2-12 show the predicted results obtained using three different CFD codes for the wind direction of 0° with the standard $k-\varepsilon$ model. All correlations between the CFD results and experimental results are shown, along with the standard errors (S.E.) and correlation coefficients (C.C.). Although there is some variation in the results in the low-velocity region (near measurement points 15–24), the correspondence with the experimental results is good in the high-velocity region for all of the codes. There are almost no differences between the standard errors or correlation coefficients for the different codes.

Figure 3-2-10. Comparison of wind speed ratios at wind direction of 0° (EXP_S and CFD_M1)Figure 3-2-11. Comparison of wind speed ratios at wind direction of 0° (EXP_S and CFD_T1)Figure 3-2-12. Comparison of wind speed ratios at wind direction of 0° (EXP_S and CFD_O1)

3.2.5.2 Effect of computational domain (code M)

Figure 3-2-13 shows how the prediction accuracy is affected by the computational domain. When the domain is as large as CFD_M2 or as small as CFD_M4, the results are almost identical to the results for the basic computational domain (CFD_M1). However, the prediction accuracy is poor when the computational domain is small and the number of surrounding buildings reproduced is decreased (CFD_M5).

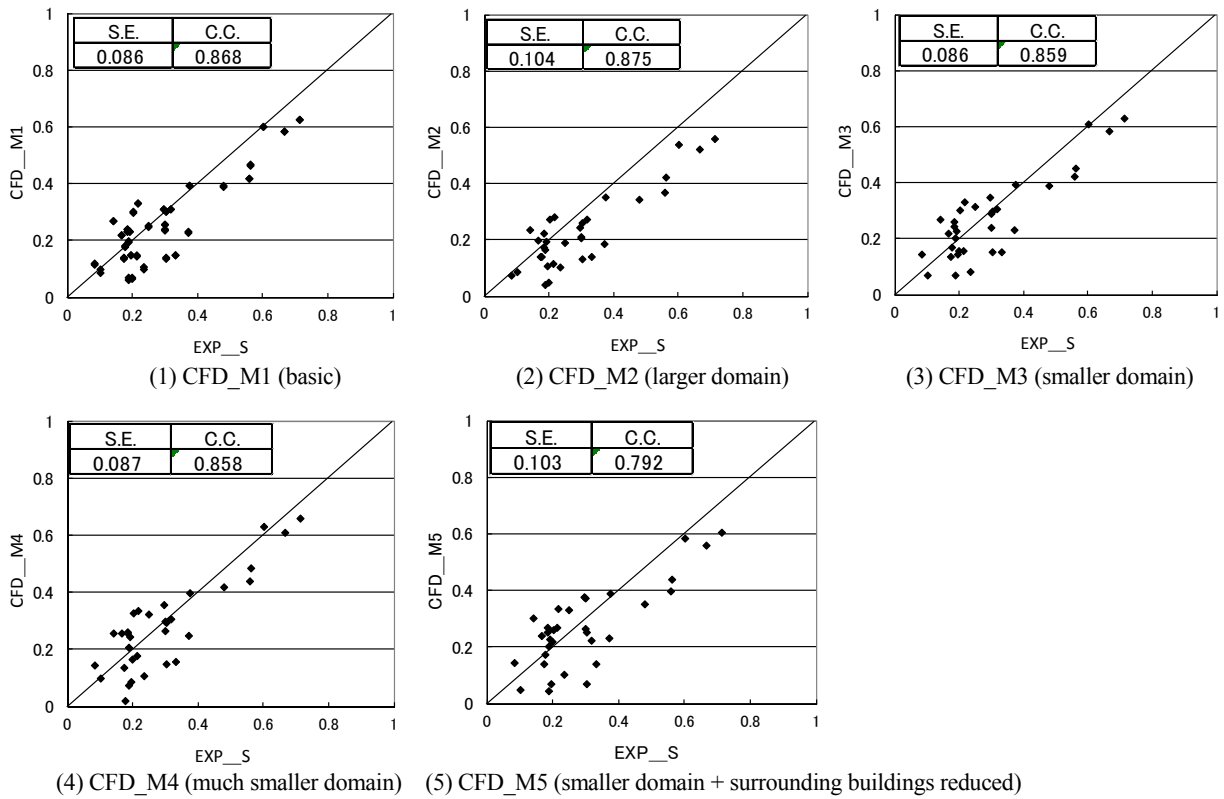


Figure 3-2-13. Impact of computational domain on prediction accuracy (code M)

3.2.5.3 Effect of wind direction

Figures 3-2-14 to 3-2-16 show comparisons of the results of the wind tunnel experiment (EXP_T) and the wind speed ratios for the cases in which the wind direction was varied for each CFD code. To compare the experimental results measured using thermistor anemometers, the CFD results were corrected using the k value from the calculation results. As the wind direction is oblique, many measurement points are located in the wake of the building. Thus, the differences become large in the low-velocity region. However, the predictions are more accurate in the high-velocity region.

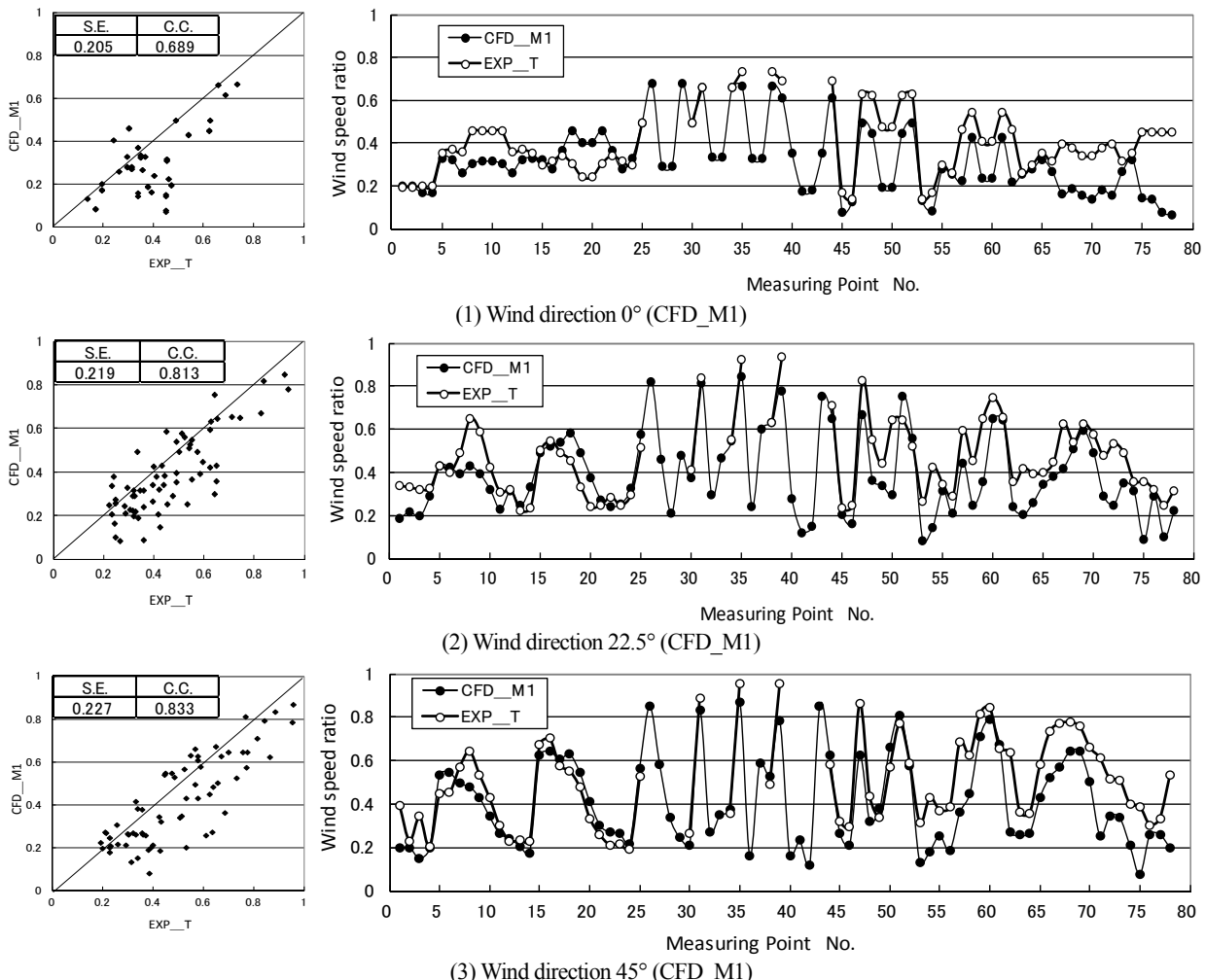


Figure 3-2-14. Comparison of wind speed ratios at each wind direction with experimental results (EXP_T) (code M)

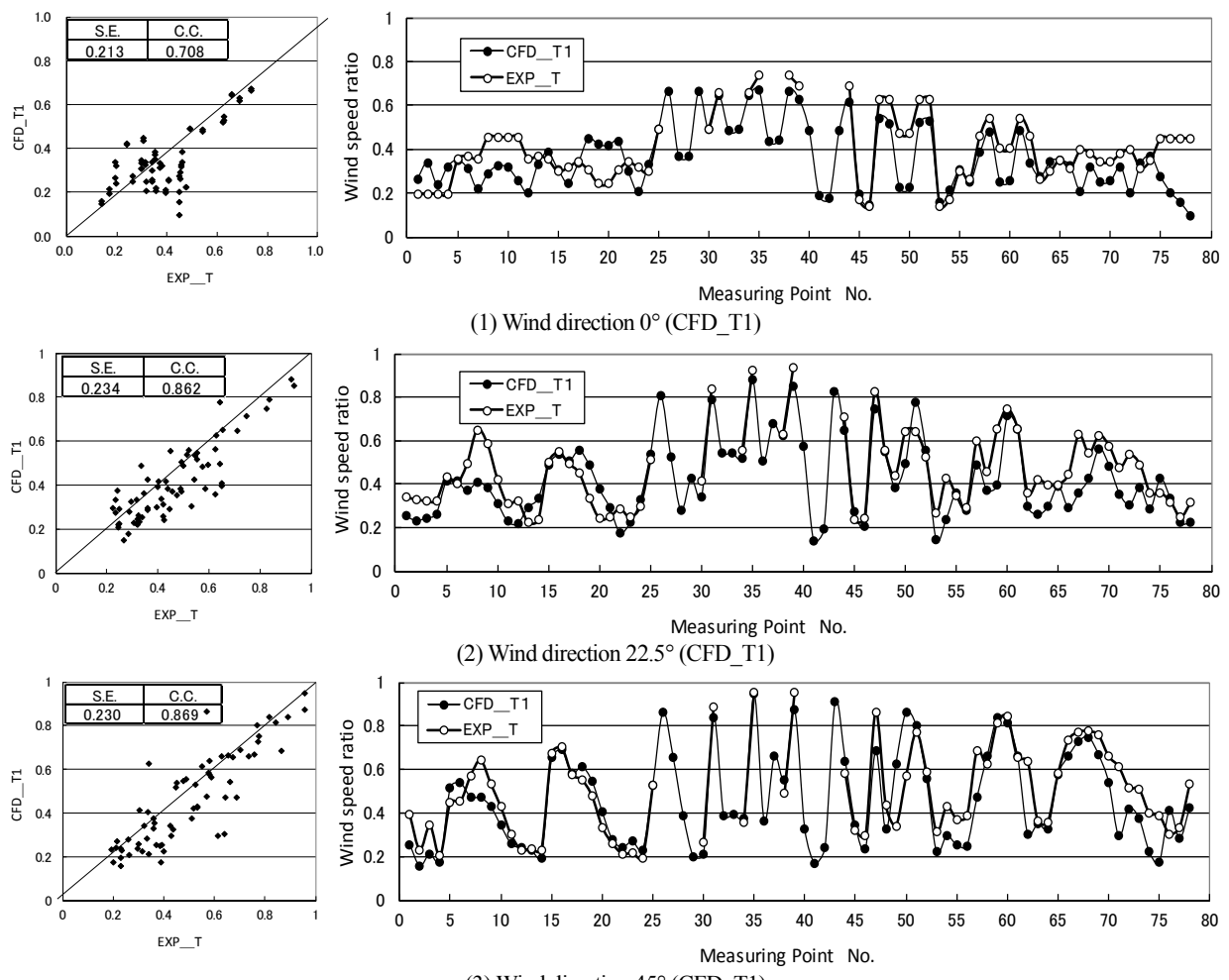


Figure 3-2-15. Comparison of wind speed ratios at each wind direction with experimental results (EXP_T) (code T)

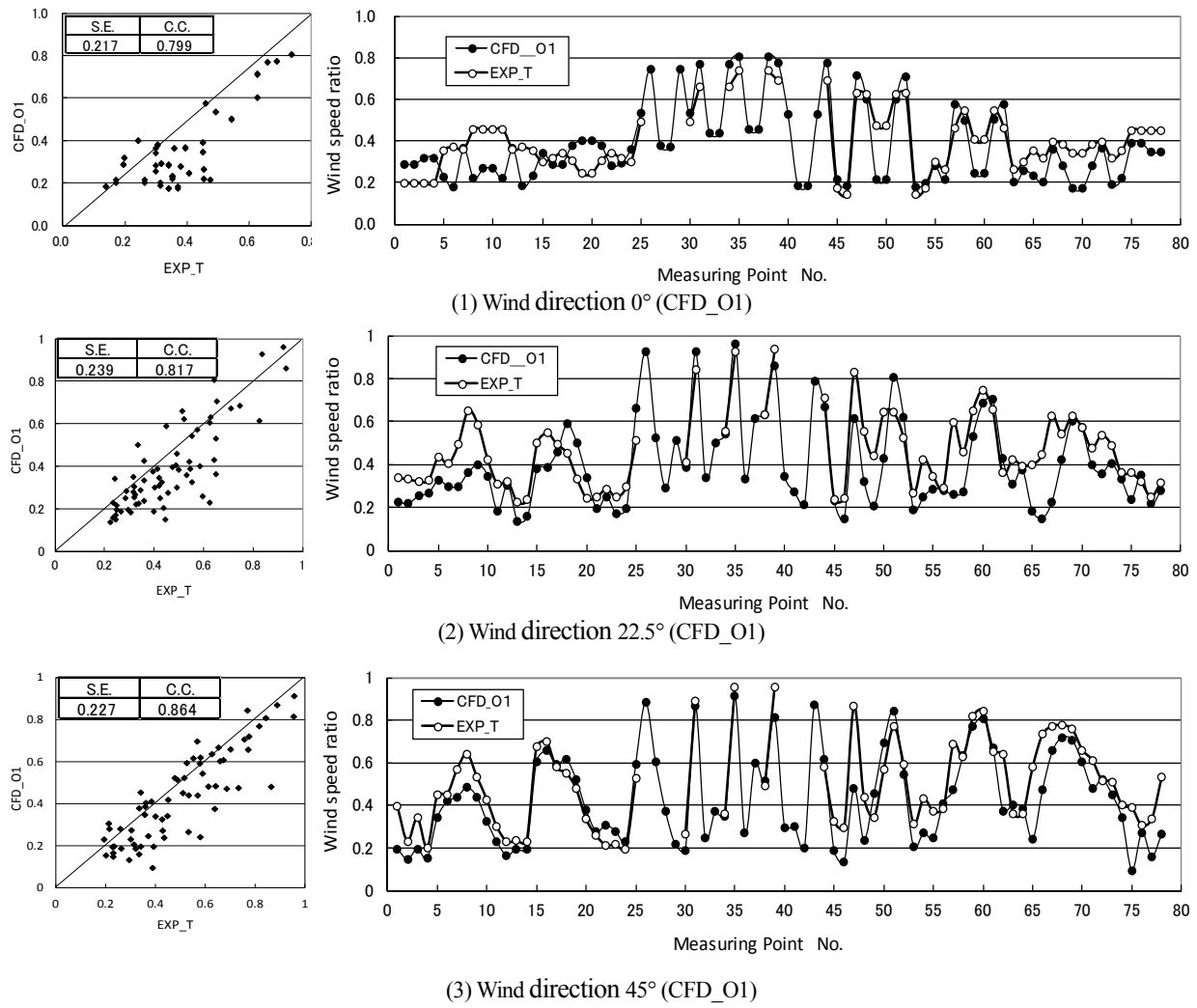


Figure 3-2-16. Comparison of wind speed ratios at each wind direction with experimental result (EXP_T) (code O)

3.2.5.4 Effect of ground surface boundary conditions

Figures 3-2-17 and 3-2-18 show comparisons of the prediction accuracy depending on differences in the ground surface boundary conditions (the z_0 -type logarithmic law and the logarithmic law for a smooth surface). The effect of the boundary conditions is not very large, but the effects appear to vary depending on the code used. For code T, the difference is small, but for code O, the effect is more noticeable. Using the logarithmic law for a smooth surface improves the standard error and the correlation coefficient.

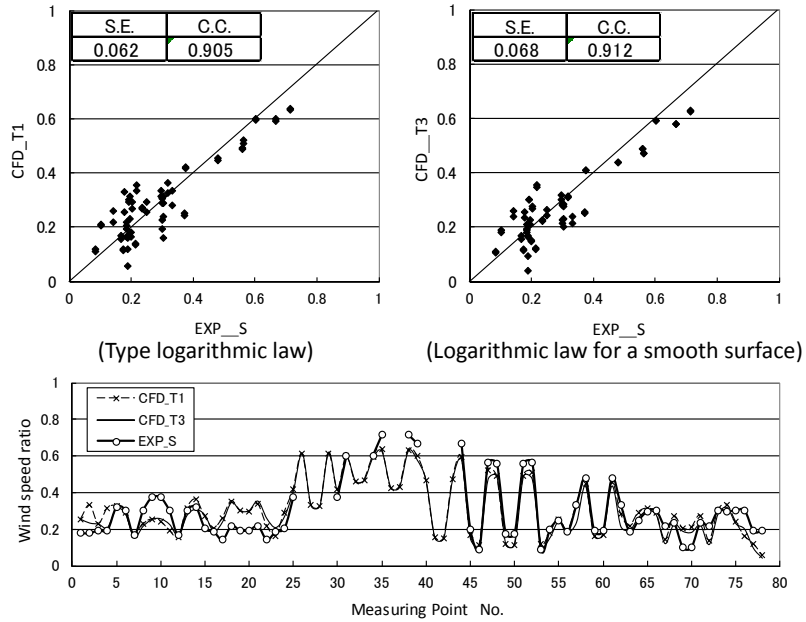


Figure 3-2-17. Comparison of prediction results for wind speed ratio for differences in ground surface boundary conditions (code T)

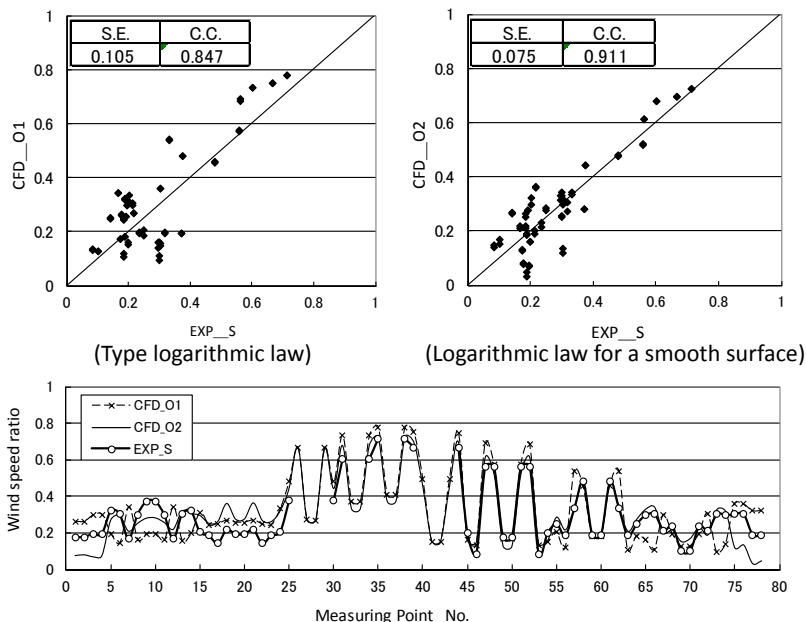


Figure 3-2-18. Comparison of prediction results for wind speed ratio for differences in ground surface boundary conditions (code O)

3.2.5.5 Effect of turbulence model

Figure 3-2-19 shows comparisons of the prediction accuracy obtained using different turbulence models, i.e., the standard $k-\varepsilon$ model and modified $k-\varepsilon$ model (LK model). The standard errors and correlation coefficients are not much different. However, when the details are compared, the modified $k-\varepsilon$ model (LK model) is found to produce a slightly higher velocity and improve the correlation with the experimental results at measurement points 35, 38, and 39, where the wind velocity peak appears.

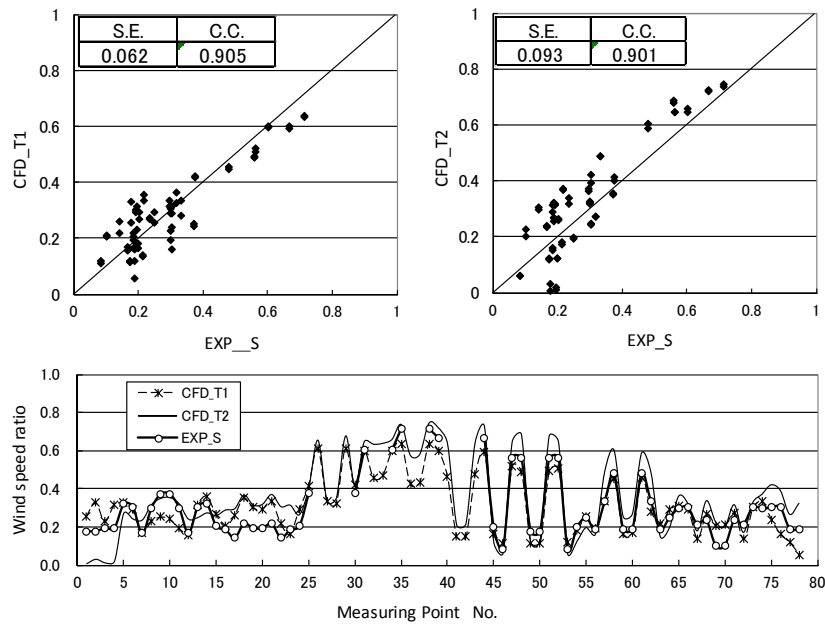


Figure 3-2-19. Comparison of prediction accuracies for wind speed ratio for different turbulence models (code T)

3.2.6 Summary of the analysis of flow around a high-rise building in a multi-block model

- The CFD results obtained in this study exhibit some variation in the low-velocity region (near measurement points 15–24), but the correlation with the experimental results was good in the high-velocity region for all of the codes. There were slight differences in the standard errors and correlation coefficients for the different codes compared.
- For the computational domain, almost no differences in the prediction results occurred when the domain width was narrowed from $9.6H$ to $4.24H$ (where H is the height of the center building). However, when the computational domain was narrowed and the number of reproduced surrounding buildings was decreased as well, the prediction accuracy became worse.
- As the wind direction is oblique, many measurement points were located in the wake of the building. Thus, differences between the calculation results and experiment results tended to be larger in the low-velocity region. However, the predictions were highly accurate in the high-velocity region.
- Differences in the ground surface boundary conditions had little effect, but the effects varied depending on the code used. The difference was small with code T, but with code O, the effect was more noticeable. Using the logarithmic law for a smooth surface improved the standard error and correlation coefficient.
 - In a comparison of the standard $k-\epsilon$ model and modified $k-\epsilon$ model (LK model), no significant differences were observed in the standard error or correlation coefficient. However, when the details were compared, the modified $k-\epsilon$ model (LK model) produced a slightly higher velocity and improved the correlation with the experimental results at measurement points 35, 38, and 39, where the wind velocity peak occurs.

4. Benchmark tests of flow in actual city block [44]

4.1 Introduction

Chapters 2 and 3 reported the results of benchmark tests conducted using relatively simple shapes, such as single buildings and groups of buildings. In actual urban areas, however, buildings have complicated shapes and are distributed in an irregular manner. To accurately reproduce them for a CFD simulation, a large number of grids are required. In particular, when an orthogonal structured grid system is used, it is difficult to provide grids that represent the building configuration accurately. Therefore, special care must be taken to account for the influence of this inaccuracy on the prediction accuracy. This problem can be solved using an unstructured grid system; however, there are some difficulties associated with preparing this type of grid system appropriately.

Furthermore, to predict the wind environment in urban areas, CFD simulations are normally performed for 16 wind directions using two patterns, i.e., before and after the construction of the target building. Moreover, in some situations, it is necessary to consider protection effects against wind achieved by activities such as planting trees. This increases the number of cases that need to be considered. Therefore, the calculation accuracy must be maintained under restrictive conditions in the practical application of CFD.

To examine these influences, two types of benchmark tests were performed with actual urban district models. The first example was a building complex in an actual urban area in which low-rise buildings are closely packed together (Niigata). Wind tunnel experiments and CFD simulations were carried out to investigate the prediction accuracy of the velocity distribution and wind environment criteria. Differences between three types of grid systems, i.e., a single structured grid system (orthogonal grid), a compound grid system consisting of multiple overlapping grids, and an unstructured grid system, were compared. This was followed by a comparison of the analysis results, wind tunnel tests, and field measurements for a group of high-rise buildings in an actual urban area (Shinjuku). This chapter concludes with practical guidelines to be followed when predicting the wind environment around high-rise buildings in an actual urban area.

4.2 Flow around a building complex in an actual urban area with dense concentration of low-rise buildings in Niigata City

4.2.1 Building complex studied

The building complex is a district with a dense concentration of two-story low-rise buildings on a flat topography near the mouth of the Shinano River in Niigata City. Assuming that a high-rise building 60 m high (building A) and two mid-rise buildings 18 m high (buildings B and C) are to be constructed, the impact of these buildings on the surrounding wind environment was predicted and evaluated. Figure 4-2-1 shows the wind tunnel experiment models of the district, and Figure 4-2-2 shows a computational model reproduced from CAD data. From the CAD data, a three-dimensional urban district model was prepared for use in the CFD calculations, as discussed below.

Building A faces relatively wide streets on the north, east, and south sides of its premises, and the highest existing building (at a height of 30 m) in the target block stands approximately 40 m to the northeast of building A. Buildings B and C face relatively wide streets on the north and east sides of their premises, with narrow lanes on their south and west sides. They are surrounded by two-story low-rise buildings.

Wind observation data measured at the Niigata Local Meteorological Observatory (averaged from January 1984 to December 1993 for an observation height of 15.9 m) were used for the wind environment evaluation. Table 4-2-1 lists the Weibull coefficients for each wind direction based on these data, including the wind rose.



Figure 4-2-1. Wind tunnel model (before construction of planned building)

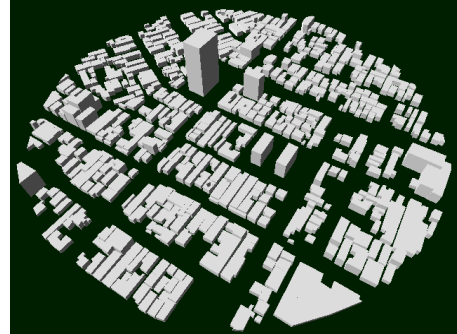


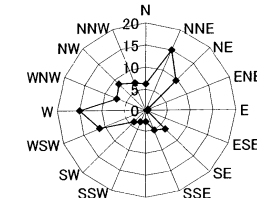
Figure 4-2-2. Urban district model (CAD data: after construction of planned building)



Figure 4-2-3 Measurement point locations

Table 4-2-1. Weibull coefficients and wind rose of daily maximum average wind speed at Niigata Local Meteorological Observatory (averaged from January 1984 to December 1993, at an observation height of 15.9 m)

Wind direction	N	NNE	NE	ENE	E	ESE	SE	SSE
A(a)(%)	6.13	15.03	9.28	0.44	0.44	0.33	6.05	5.09
C(a)	5.59	5.41	4.54	4.47	0.00	0.00	5.91	4.73
K(a)	3.23	3.16	2.63	4.46	0.00	0.00	3.87	2.72
Wind direction	S	SSW	SW	WSW	W	WNW	NW	NNW
A(a)(%)	2.55	2.93	3.81	11.03	14.82	7.04	8.40	6.65
C(a)	4.05	4.24	5.95	7.80	8.34	7.86	8.01	6.81
K(a)	4.58	4.17	2.54	3.72	3.38	3.15	3.23	3.20



4.2.2 Outline of wind tunnel experiment

The wind tunnel experiment was performed using the boundary layer wind tunnel at the Niigata Institute of

Technology. Table 4-2-2 gives an outline of the experiment. Figure 4-2-4 shows a vertical profile of the approaching flow. These values were made dimensionless using the boundary layer thickness H and average wind speed U_H at this height as representative values.

In the same manner as in previous studies, the roughness length z_0 of the ground surface was obtained as $z_0 = 9.6 \times 10^{-5}$ m (in model scale) and $z_0 = 0.024$ m (in actual scale) by substituting the average wind velocity $\langle u \rangle$ (2.77 m/s) at measurement point z (0.003 m) closest to the floor of the wind tunnel and substituting the turbulent kinetic energy k ($0.34 \text{ m}^2/\text{s}^2$) in the logarithmic law including z_0 .

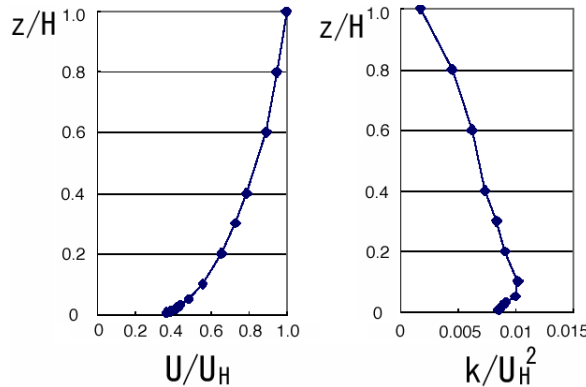


Figure 4-2-4. Vertical profile of inflow air flow (H is boundary layer thickness)

Table 4-2-2. Outline of wind tunnel experiment

Model scale	1/250
Diameter of turntable	1.6 m (400 m in actual scale)
Wind tunnel section	Width 1.8 m × Height 1.8 m
Inflow profile	Power law ($\alpha = 0.25$)
Boundary layer height H	1 m (250 m in actual scale)
Reference velocity U_H	7.8 m/s
Measurement	2 m height from ground surface in actual scale Scalar velocity was measured by thermistor anemometry

4.2.3 Outline of CFD simulations

Based on knowledge gained from the benchmark tests of relatively simple shapes, common calculation conditions were specified as listed in Table 4-2-3. The shape of the urban topography was prepared for each CFD code based on the CAD data shown in Figure 4-2-2. Table 4-2-4 lists the characteristics of and calculation conditions for the three different CFD codes compared. Figure 4-2-5 illustrates the calculation grids used by each CFD code. The standard $k-\varepsilon$ model was used as the turbulence model in all CFD codes, and code O used the four other turbulence models.

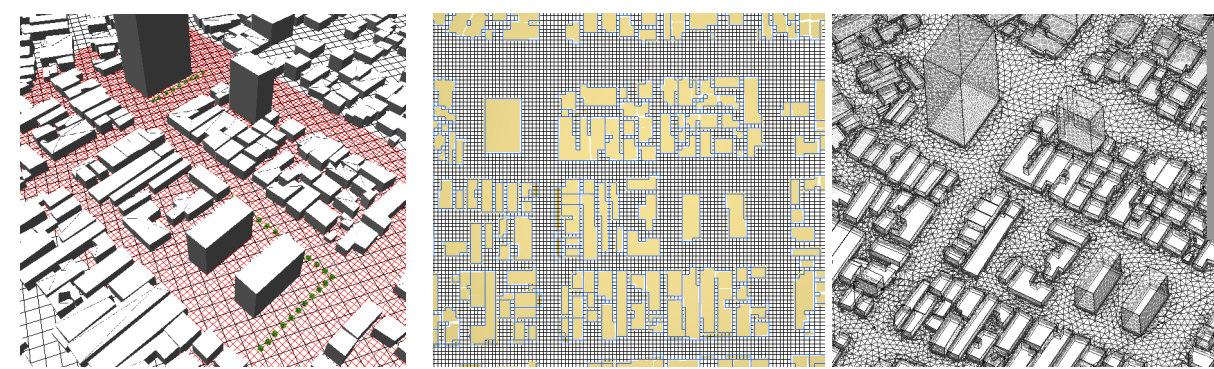
Table 4-2-3. Calculation conditions common to all analysis codes

Inflow boundary	Interpolated values of $\langle u \rangle$ and k from experimental value of the approaching flow. The value of ε is given from the relation $P_{k-\varepsilon}$.
-----------------	---

Computational domain	Area approximately 500 m (x) \times 500 m (y) \times 300 m (z), which includes whole urban block.
Upper surface of computational domain	Free slip wall condition.
Outflow boundary condition	Zero gradient condition.
Ground surface boundary	Logarithmic law with roughness length z_0 ($z_0 = 0.024$ m).
Building surface boundary	Logarithmic law for smooth wall.
Turbulence model	Not specified.
Grid discretization	Third fluid cell is located 2 m above the ground. No other condition specified.

Table 4-2-4. Outlines of calculation conditions for each analysis code

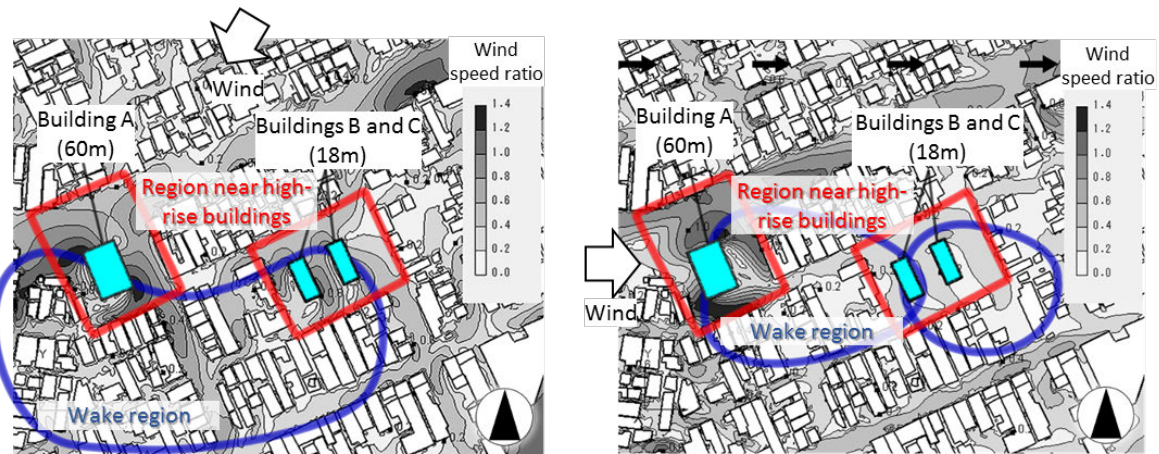
CFD Code	Code O	Code M	Code T
	Self-made code	Commercial code	Commercial code
Computational method and time integral scheme	Overlapping structured grid	Structured grid	Unstructured grid
	Finite volume method (FAVOR)	Finite volume method	Finite volume method (CVFEM)
Turbulence model	Standard $k-\varepsilon$ Durbin Modified LK S S- Ω	Standard $k-\varepsilon$	Standard $k-\varepsilon$
	3 rd -order upwind	QUICK	MUSCL(2 nd -order)
Algorithm	Artificial compressibility	SIMPLE, steady state	SIMPLE, steady state
Computational time	Approximately 2 hours per wind direction	Approximately 6 hours per wind direction	Approximately 1 hour per wind direction
	Pentium 4 2.1 GHz	Xeon 2 GHz	Pentium 4 2.8 GHz
Grid resolution	Overlapping grid. Whole domain: 5 m in horizontal plane. 0.25 million cells. Inner domain: 2 m in horizontal plane. Non-uniform grid with 0.7 m near ground surface in vertical section.	Single grid. Nonuniform. 0.80 million cells ($150 \times 140 \times 38$). 2 m \times 2 m in horizontal plane near planned buildings.	Single grid. Tetra, pyramid, prism cells. 0.80 million cells and 0.20 million nodes. Approximately 20 m near top surface and approximately 2.5 m near ground surface. Approximately 0.6 m by prism layer cells near building and ground surface.

(1) Code O (Structured grid/overlapping grid) (2) Code M (Structured grid) (3) Code T (Unstructured grid)
Figure 4-2-5. Grid discretization of each analysis code

4.2.4 Comparison according to wind speed ratio

4.2.4.1 Comparison between analysis codes

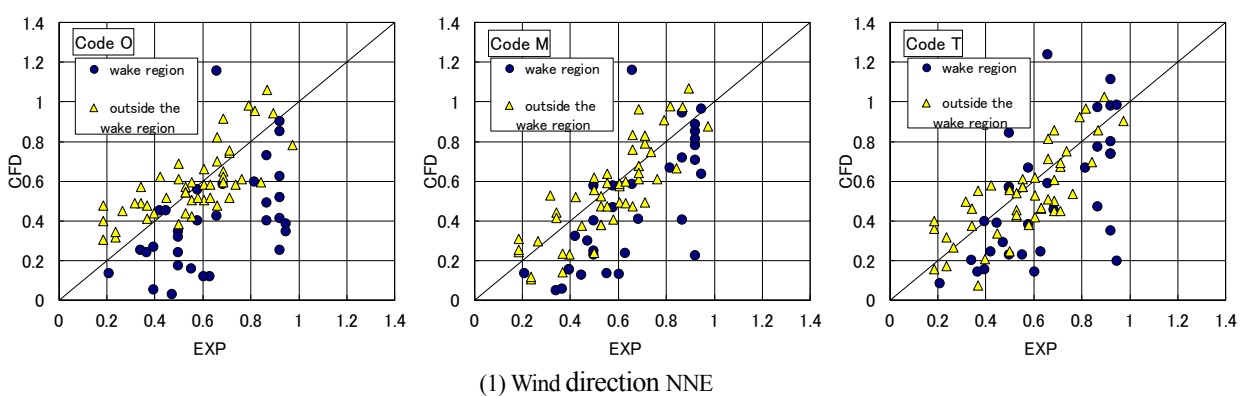
The results obtained with the three CFD codes with the standard $k-\varepsilon$ model were compared. All calculations were performed for 16 wind directions. Two wind directions, NNE and W, which are the two wind directions that occur most frequently, were considered, based on the wind rose shown in Table 4-2-1. The wind speed ratios were obtained using the inflow velocity at an evaluation height of 2 m as the reference velocity. Because no large differences in the overall distribution properties of the wind speed ratios were seen between the codes, the distribution of the wind speed ratio based on analysis code T (see Table 4-2-4) was selected as representative, as shown in Figure 4-2-6. In the case of wind direction NNE, a region of extremely high wind speed was observed at the building corner on the northwest and east sides of building A. In addition, strong winds are caused by contraction flows between building B and building C. In the case of wind direction W, on the other hand, a region of high wind speed was observed at the corner of the south side of building A, but overall, the wind speed in the side streets is lower than it is at wind direction NNE. In both wind directions, the wind velocity varied significantly by location on the street from west to northeast.



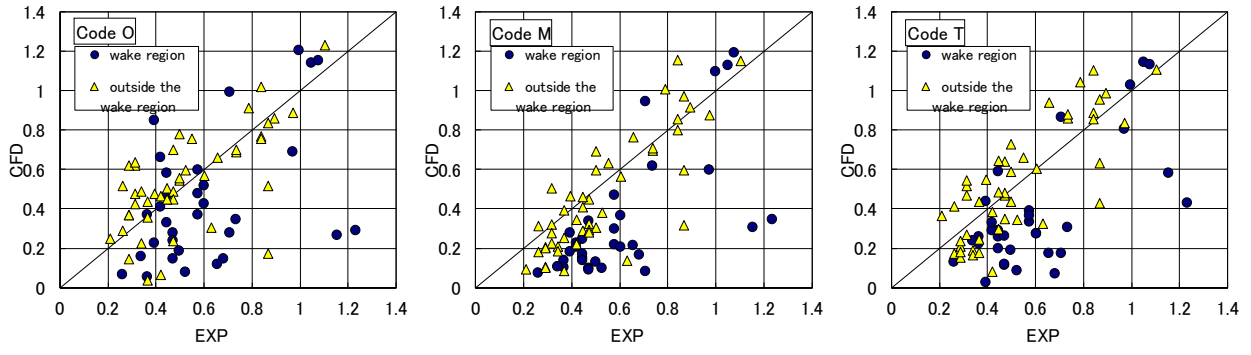
(1) Wind direction NNE

(2) Wind direction W

Figure 4-2-6. Distributions of wind speed ratios (CFD results by code T)

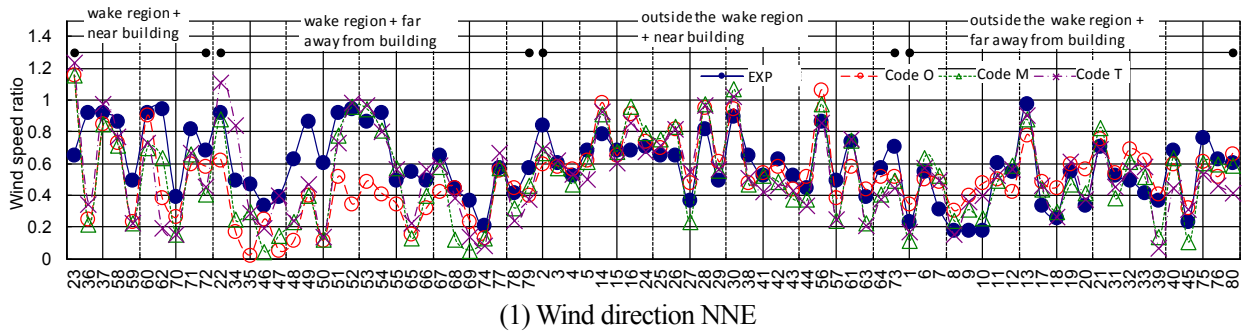


(1) Wind direction NNE



(2) Wind direction W

Figure 4-2-7. Correlation of wind speed ratio according to each analysis code with wind tunnel experiment results



(1) Wind direction NNE

(2) Wind direction W

Figure 4-2-8. Comparison of wind speed ratios at measuring points

Figure 4-2-7 shows the correlation of the wind speed ratios obtained from the CFD simulations and the wind tunnel experiment. The plots are categorized as inside and outside the wake region of the planned building. The prediction results obtained with the different CFD codes are generally similar, and no clear trend is observed for any differences between the codes. Overall, in every wind direction, in the wake region of the planned building, the CFD prediction results tend to underestimate the wind speed in comparison to the wind tunnel experiment results. In other regions, the prediction results are relatively well correlated with the experimental results. The underestimation of velocity in the wake region of the building is attributed partly to the difference in the definitions of the averaged scalar velocities obtained by CFD and thermistor anemometer, as discussed in relation to the previous benchmark tests.

Figure 4-2-8 shows a comparison of the wind speed ratios for each measuring point. Overall, the CFD results accurately reproduce the wind tunnel experiment results. The prediction accuracy near the building but outside the wake region of the building is particularly high. There are large discrepancies at several measurement points (for example, no. 49 at wind direction NNE and nos. 31 and 66 at wind direction W; see Figure 4-2-3 for the measurement point locations), but these are all on side streets, relatively far from the planned building. The presumed reason for this is the impact of slight differences in the prediction properties of the separated shear layer resulting from differences in

the reproducibility of the building shape. Errors in representing the building shapes and evaluation point locations in the CAD data used may also be factors.

4.2.4.2 Effect of differences in turbulence models

A comparison was made of the results obtained using five different turbulence models based on code O, i.e., the standard $k-\epsilon$ model, Durbin model, S model (mixed-time scale $k-\epsilon$ model), modified LK model, and S- Ω model. All of the predictions were performed for 16 wind directions. As seen in the wind roses shown in Figure 4-2-3, the predicted wind speed ratio for wind directions NNE and W, which are the prevailing wind directions in this area, are compared. The wind speed ratio was standardized by the inflow wind velocity at the evaluation height of 2 m.

Figure 4-2-9 shows a comparison of the wind speed ratios at each measurement point. Almost no difference is observed depending on the turbulence model adopted. This is because the measurement points are not sufficient to capture the properties of the strong wind region around the windward corners of the planned building in the wind tunnel test used for the comparison. In addition, the low-rise buildings are densely concentrated around the planned buildings. As a consequence, the inflow wind approaches the planned building along the main street, so that the error—the overestimation of turbulent kinetic energy at the impinging region, which is pronounced in the standard $k-\epsilon$ model—is less exposed.

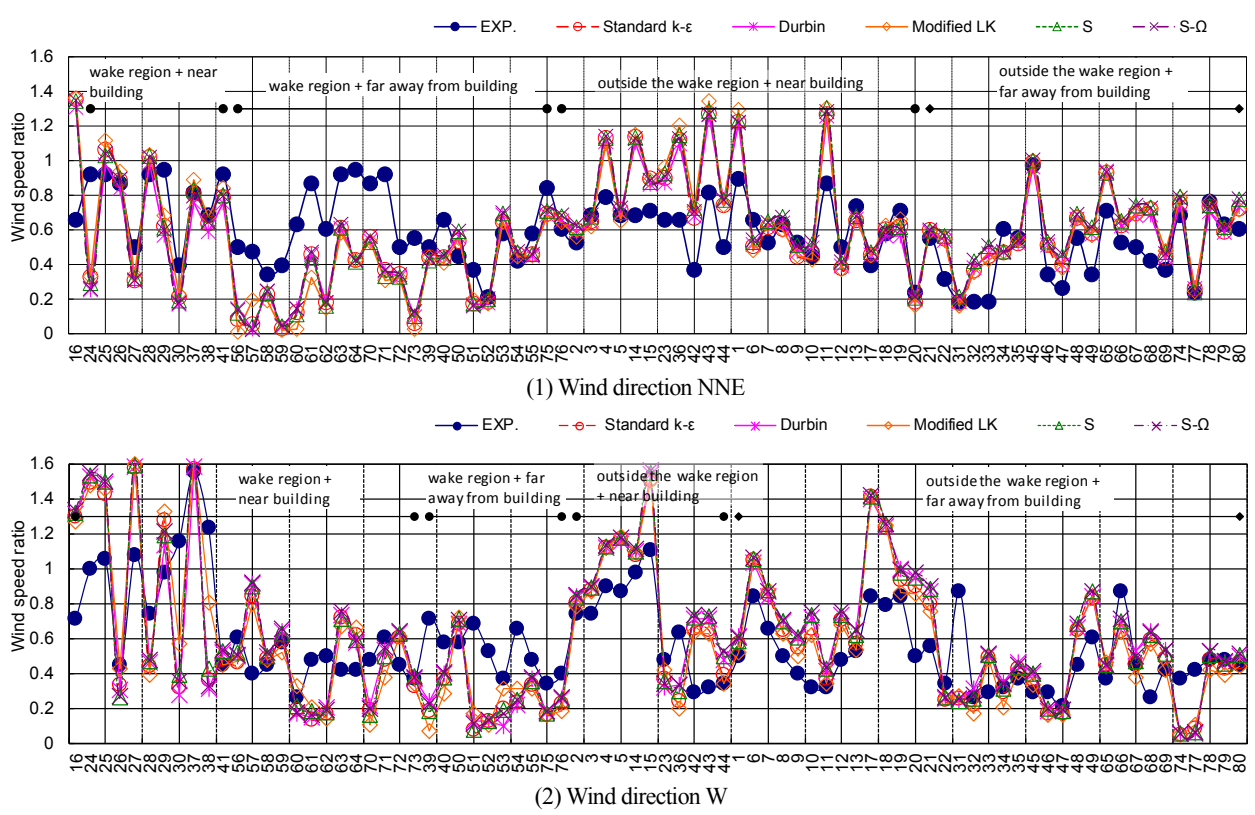
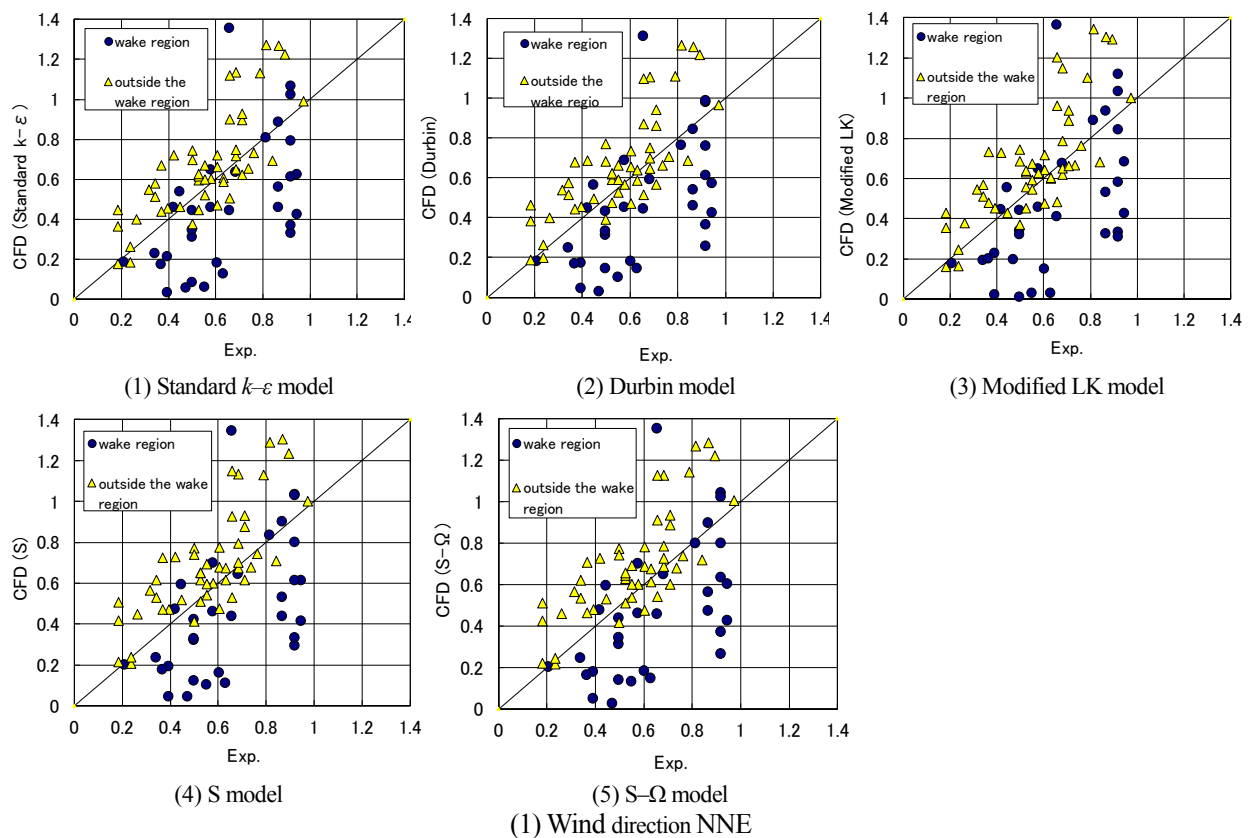


Figure 4-2-9. Comparison of wind speed ratios at each measuring point

Figure 4-2-10 shows the correlation of the wind speed ratios obtained by CFD with each turbulence model and the wind tunnel experiment. As mentioned above, the plots are categorized as inside and outside the wake region of the planned building. Other than slight differences between the turbulence models in the wake region of the planned building, no clear tendency is observed in the differences between the turbulence models compared.



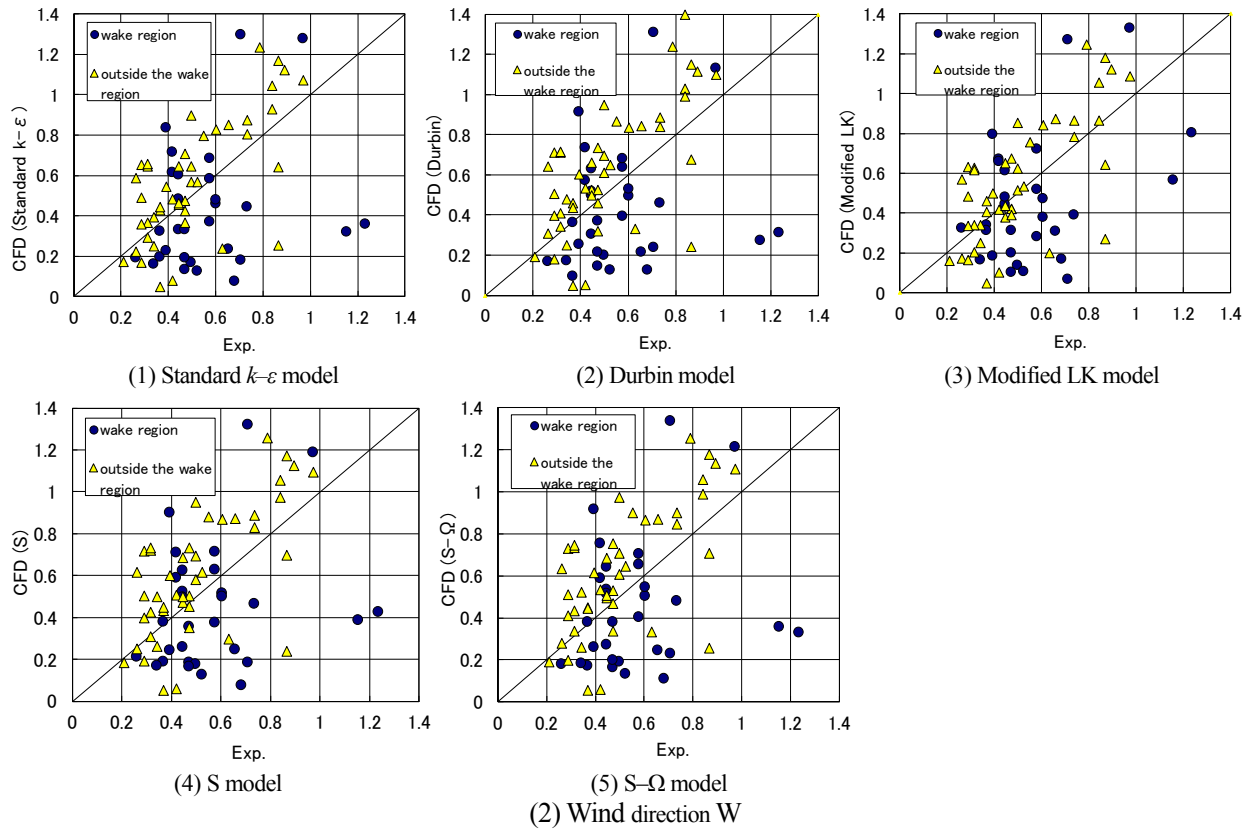


Figure 4-2-10. Correlations of wind speed ratios by CFD and wind tunnel experiment results for different turbulence models

Figure 4-2-11 shows the distribution of the wind speed ratios. Although slight differences are observed in the strong wind region near the northwest corners of building B in the NNE wind direction case and near the north corners of building A in the W wind direction case, no clear differences are observed in the overall distribution patterns.

A detailed comparison shows that in the NNE wind direction case, the region surrounded by the strong wind region (contour lines of 1.0–1.2) near the northwest corners of building B is very small in the standard $k-\varepsilon$ model results, but it clearly exists (Figure 4-2-12 shows the expanded figure) in the modified LK model, S model, and S- Ω model. In the W wind direction case, the region surrounded by the strong wind region at the north-side corners of building A (contour lines of 1.2–1.4) is wider in the Durbin model, S model, and S- Ω model results, compared to those of the standard $k-\varepsilon$ model. As seen in the single building cases, the impact of differences in the turbulence models on the prediction of flow separation is observed. In general, the standard $k-\varepsilon$ model predicts a narrower strong wind region than the other turbulence models. Because the strain rate S is extremely large at the corners of the planned building, in the case of the Durbin model [26], for the W wind direction, the time scale T was predicted to be smaller, and v_t was also predicted to be smaller. Therefore, overestimation of the turbulent kinetic energy k is suppressed in comparison with the standard $k-\varepsilon$ model case, and the strong wind region at the corner of the planned building becomes wider than in the standard $k-\varepsilon$ model results. Similarly, in the S model (the mixed-time-scale $k-\varepsilon$ model [29]), because the value of S is large in this region, the time scale τ_m becomes large and v_t becomes small. Therefore, because the overproduction of turbulent kinetic energy is prevented, the strong wind region at the corner of the planned building becomes wider than in the standard $k-\varepsilon$ model results. On the other hand, in the case of the modified LK model [27], because the production term of the turbulent kinetic energy k is represented by the product of S and Ω , the production

of k becomes small in the strong-wind region of the corners of the planned building, where $S > \Omega$. Therefore, in the case of the wind direction NNE, the strong wind region at the corner of the planned building in the modified LK model is wider than that in the standard $k-\varepsilon$ model case.

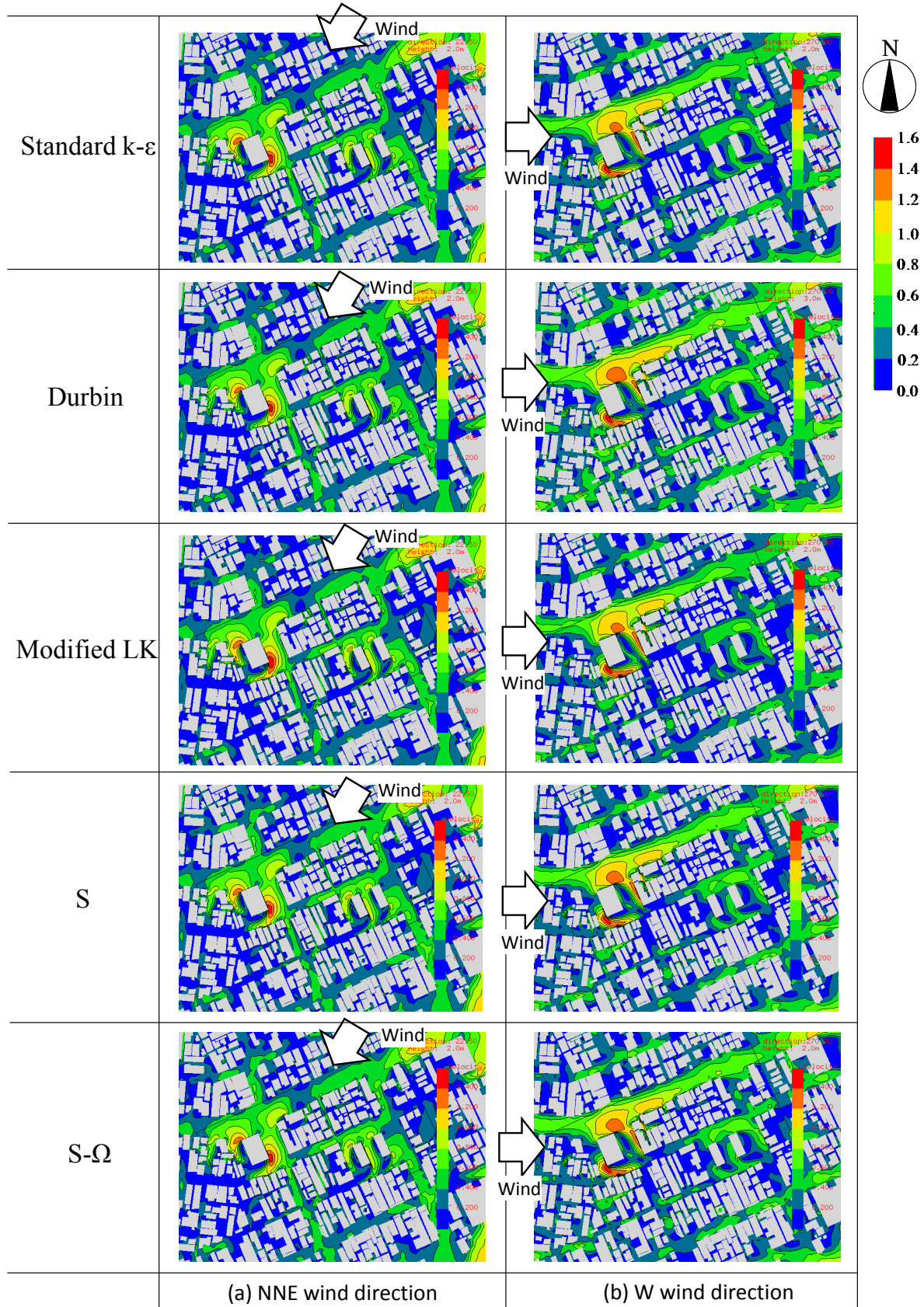


Figure 4-2-11. Distribution of wind speed ratios (ratio to inflow wind speed at height of 2 m: CFD results for code O)

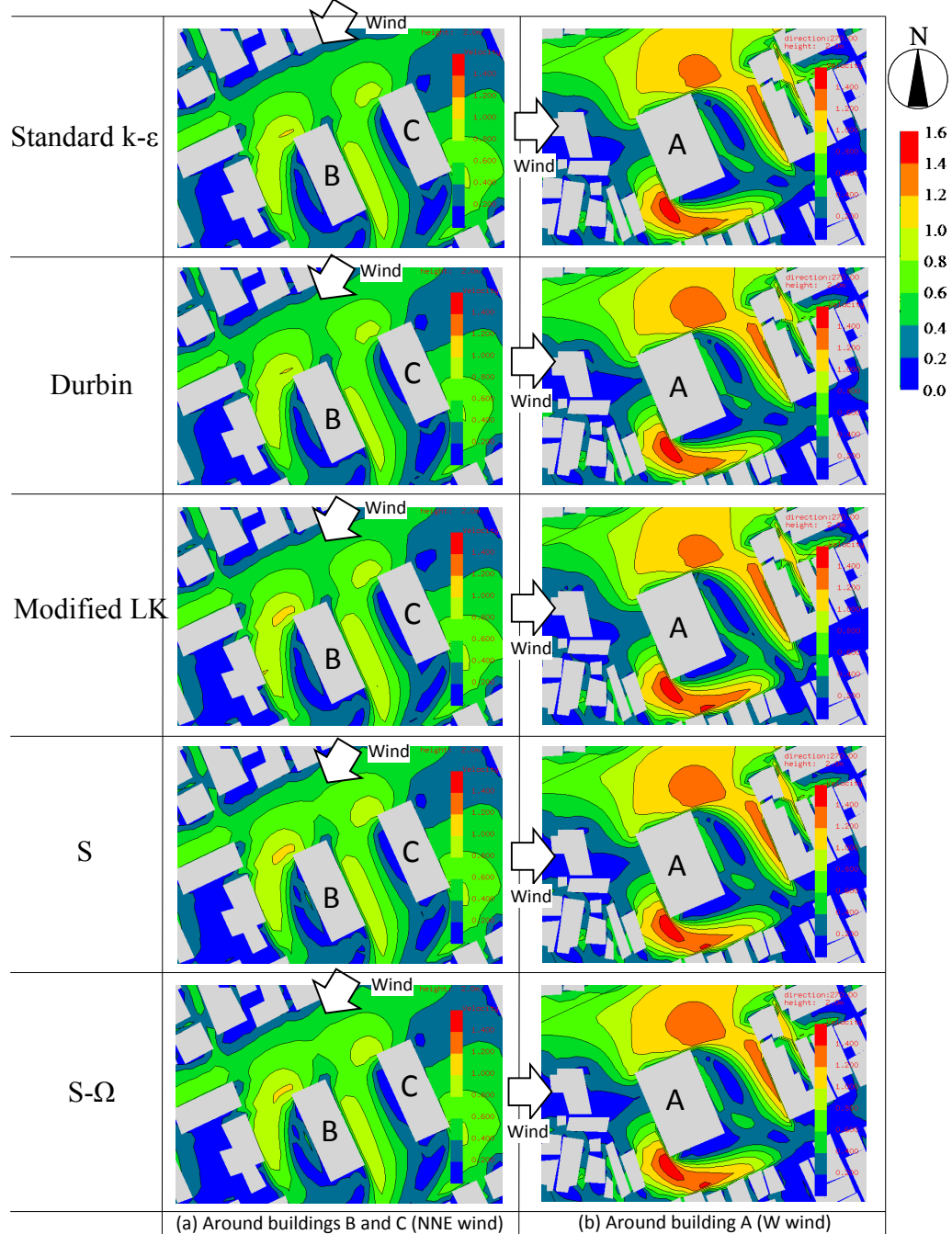


Figure 4-2-12. Distribution of wind speed ratios around planned building (ratio to inflow wind speed at height of 2 m: analysis results for code O)

4.2.5 Comparison according to wind environment evaluation scale

Figure 4-2-13 shows the predicted results for the wind environment criteria proposed by Murakami et al. [36, 37] using the wind tunnel experiment and CFD results based on the meteorological data observed at the Niigata Local Meteorological Observatory. Overall, at the measurement points marked as rank 1 on the northeast and south sides of building A, the CFD and wind tunnel experiment results correspond well. However, as previously mentioned, at the measurement points along the side streets and around the low-rise buildings along the main streets, some differences are evident between the experimental results and the CFD results obtained for each CFD code.

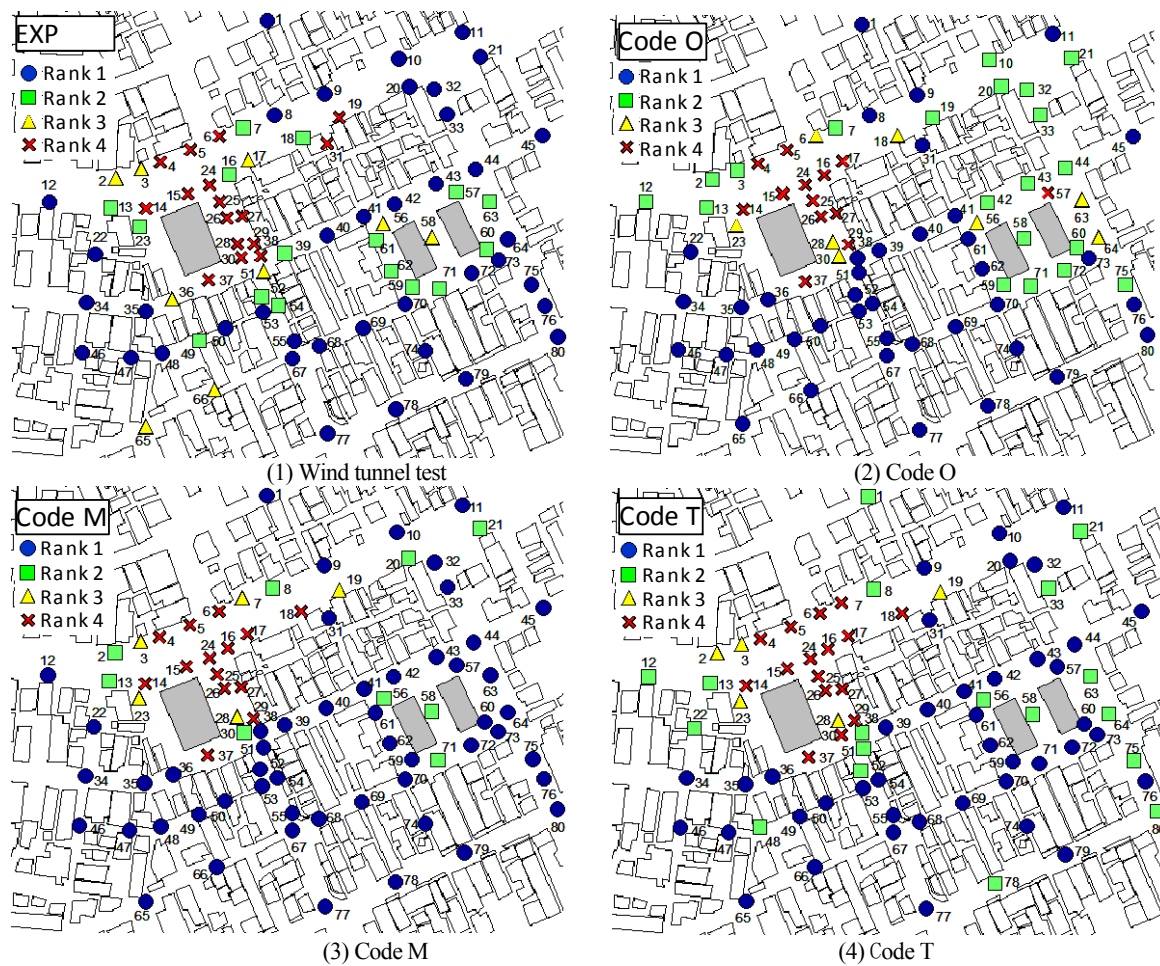


Figure 4-2-13. Comparison based on wind environment evaluation criteria

4.2.6 Summary of the analysis of flow around a building complex in an actual urban area with dense concentration of low-rise buildings in Niigata City

CFD analyses were carried out to predict the wind environment in a building complex in Niigata City where low-rise buildings are densely concentrated. The results were compared with the results of wind tunnel tests. The following information was obtained:

- Using a common grid resolution and boundary conditions, the different CFD codes considered produced almost identical results for the wind environment around the buildings, regardless of the grid system or type of analysis method used.
- Overall, the CFD results and experiment results were well correlated in the strong wind region near the high-rise building.
- However, in the wake region of the planned building, the CFD simulations underestimated the wind speed in comparison to that obtained in the wind tunnel experiment. This finding is consistent with the results obtained in the benchmark tests for the single building models.
- When a comparison was performed for the wind environment criteria proposed by Murakami et al., although there were some slight differences between the experiment results and CFD results, they generally agreed well.

In the analysis of actual urban building complexes, the modeling accuracy of the shapes of the surrounding buildings has a greater impact on the prediction results than the choice of the turbulence model and the ground surface boundary conditions assumed. However, in general, in the analyses conducted using CAD data for the experimental model, the wind environment in the urban district was reproduced accurately, excluding some exceptional locations. In addition, it was demonstrated that a structured grid system can be used in practical applications, because the prediction results obtained using a structured grid, for which it is difficult to represent complicated building shapes exactly, yielded results similar to those obtained using unstructured grids. Of course, in a case in which details of the flow close to the wall surface of buildings is of interest, a structured grid has the difficulty in reproducing building shapes. In such a case, it is necessary to make the grids finer in the structured grid than those in the unstructured grid. An overlapping grid is superior to a single structured grid because it permits the grid resolution near the building to be improved easily without significantly increasing the total grid number.

4.3 Flow around a group of high-rise buildings in the Shinjuku sub-central area

4.3.1 Outline of wind tunnel experiments and measurements compared

As a validation of the results of the CFD predictions, it is important to consider their correspondence with not only wind tunnel experiment results but also field measurements. However, because there were no appropriate field measurement results that could be used to validate the accuracy of CFD, almost no such study has been performed. Therefore, a benchmark test was performed for the Shinjuku sub-city center in the early stage of its development [5]. Detailed wind tunnel tests and field measurements were conducted at the construction stage with the cooperation of various research institutes to examine the prediction accuracy of CFD.

4.3.1.1 Wind tunnel experiment

Although several wind tunnel experiments have been performed for the Shinjuku sub-city center, the focus of the CFD simulations conducted for this validation was on the conditions of experiment B reported by Fujii et al. [5].

4.3.1.2 Field measurement

Although field measurements were obtained between December 1975 and November 1983, the building configuration in 1977, which corresponded to that used in the wind tunnel experiment, was analyzed. A three-cup anemometer was used, and its measurement height ranged from 3 to 9 m above the ground, depending on the measurement point. Figure 4-3-1 shows the urban district reproduced and the locations of the measurement points.

The following comparisons used the averaged wind speed ratios standardized by the reference wind velocity for each wind direction, under the condition that the reference wind velocity was over 5 m/s, from the observation data collected in 1977.



Figure 4-3-1. Reproduced area of building geometry and measurement points

4.3.2 Outline of calculations

As in the case of the building complexes in Niigata City, the calculation conditions listed in Table 4-3-1 were set as the basic conditions. With respect to the shapes of the building complexes, no wind tunnel experiment models were available at the time, so CAD data for the urban district shape and topography at that time were prepared using outline maps based on design drawings, photographs, and aerial photographs found in ref. [6]. The input data used for the CFD simulations were then prepared based on the CAD data. However, because the details of the model related to the elevation of the topography were unclear, it was reproduced in a staircase pattern using 5-m units with reference to the map at that time. Figure 4-3-2 shows the prepared CAD data.

Table 4-3-2 lists the differences between the characteristics of and calculation conditions for the CFD codes that were compared. Only CFD_A used a structured grid; the rest used unstructured grids. Because the measurement points were located not only beside the high-rise buildings but also among the group of surrounding low-rise buildings, in CFD_A, the entire computational domain was treated as a single grid structure with a horizontal resolution of 5 m.

Table 4-3-1. Specified common calculation conditions

Inflow boundary condition	$\langle u \rangle$: The interpolated values from the wind tunnel experiment (power law $\alpha = 1/4$). k : The estimated value from the turbulent intensity in the experiment. ε : Estimated from the relation $P_k = \varepsilon$.
Computational domain	Horizontal direction: More than 1000 m × 1000 m (the whole wind tunnel model is included; Figure 4-3-1). Vertical direction: More than 500 m (the boundary layer height in the wind tunnel).
Upper surface of computational domain	Free slip wall condition.
Outflow boundary condition	Zero gradient condition.
Ground surface boundary	Logarithmic law for smooth wall.
Building surface boundary	Logarithmic law for smooth wall.
Turbulence model	Not specified.
Grid discretization	Evaluation height, which is 5 m above the ground, should have more than three cells toward the ground.

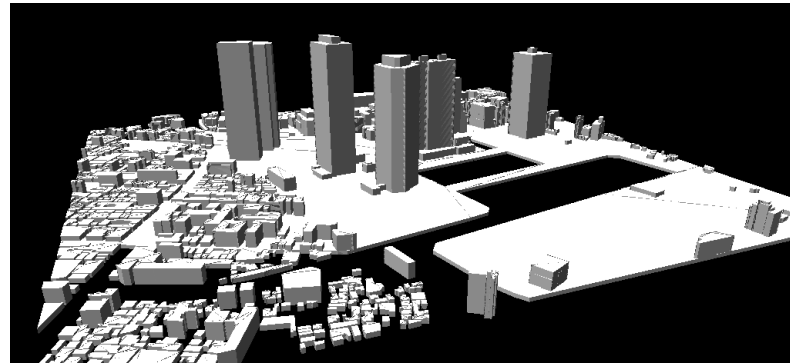


Figure 4-3-2. CAD data of urban area

Table 4-3-2. Outline of and calculation conditions for analysis codes

CFD code	CFD A	CFD B	CFD C
	Self-made code	Commercial code	Commercial code
Computational method and time integral scheme	Structured grid	Unstructured grid	Unstructured grid
	Finite volume method (FAVOR)	Finite volume method (CVFEM)	Finite volume method
Turbulence model	S- Ω model	LK model	RNG $k-\epsilon$ model
Scheme for advection term	3 rd -order upwind	MUSCL (2 nd -order)	QUICK
Algorithm	Artificial compressibility	SIMPLE, steady state	SIMPLE, steady state
Computation time	Approximately 17 hours per wind direction	Approximately 12 hours per wind direction	Approximately 2.5 hours per wind direction
	Xeon, 3.6 GHz	Pentium 4, 3.0 GHz	Alpha 667 MHz × 4 CPU
Grid resolution	Single grid Rectangular grid Total 2.95 million cells Uniform 5 m cell in horizontal plane (220×220) and nonuniform 61 cells (1 m minimum) in vertical plane	Single grid Tetra, pyramid, and prism cells. Total 1.18 million cells and 0.33 nodes 30 m resolution near top surface, 7.5 m near building, 0.6 m near the ground and building surfaces with prism cell	Single grid Hexa and prism cells. Total 1.60 million cells 1 m resolution near the ground and 3 m near the central region in horizontal plane

CFD_A (structured grid)	CFD_B (unstructured grid)	CFD_C (unstructured grid)
-------------------------	---------------------------	---------------------------

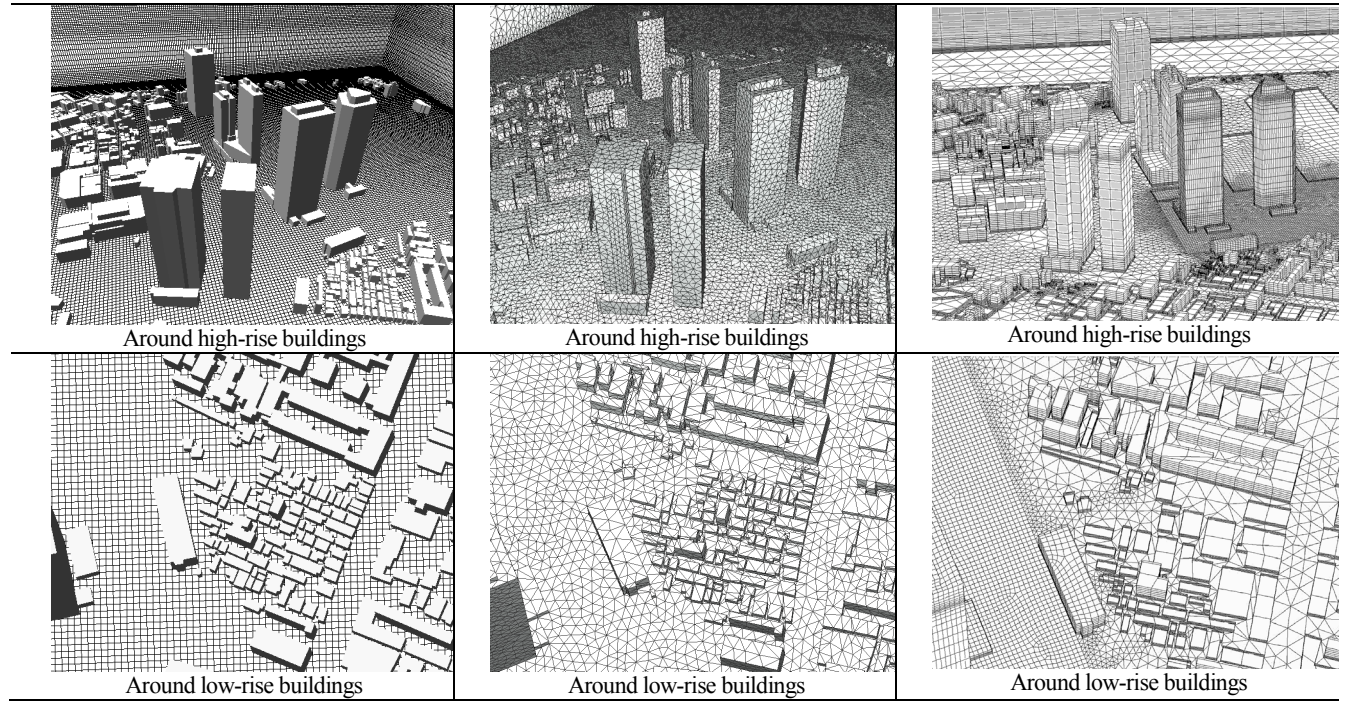


Figure 4-3-3. Grid discretization of analysis codes

4.3.3 Comparison of wind speed ratios

Based on the wind tunnel experiment and field measurement results, the CFD results were standardized by the wind speed at the reference measurement points (the Shinjuku Mitsui Building (D in Figure 4-3-1, with an observation height of 237 m) for the NE-N-NW wind directions and the KDD building (C in Figure 4-3-1, with an observation height of 187 m) for the other wind directions). The scalar wind speed obtained by CFD was corrected using the prediction results for the turbulent kinetic energy k , as described in section 3.1.

Figure 4-3-4 shows a comparison of the experimental and measured wind speed ratios at representative measurement points (in Figure 4-3-1, the circled measurement points). Overall, the wind tunnel experiment results are within the standard deviation of the field measurement values, and the CFD results are also generally in this range. Moreover, the differences between the CFD codes are small. However, at the following measurement points and wind directions, there are some differences between all of the CFD results and the experiment and field measurement results:

- Measurement point no. 7, wind direction E

The CFD results indicate higher wind speed ratios than the field measurement values. In the CFD results, because the edge of the separation flow formed from the northeast corner of the Shinjuku Mitsui Building reached this measurement point, the wind speed ratios become larger. This is attributed to the difference in the locations of the separated shear layer between the measurements and CFD, which is probably the result of representative errors of the measurement point locations and the existence of structures on the ground surface.

- Measurement point no. 13, wind direction SSW–WSW

The wind speed ratios indicated by CFD are lower than the experiment and field measurement values. At these wind directions, because the measurement points are downwind from the Shinjuku Mitsui Building, the velocity values are still underestimated, as a result of the shortcoming of the RANS model mentioned before, even if the correction based on the turbulent kinetic energy k is applied.

- Measurement point no. 15, wind direction NE

At this measurement point, the wind speed ratios of the field measurements change largely from wind direction NE to ENE. On the other hand, the change is large from NNE to NE in the CFD results. Because the location of the reference wind velocity changes for wind direction NE, a slight change in the wind directions between the reference locations produces notable difference between the field measurements and CFD results.

Figure 4-3-5 shows a comparison of the wind speed ratios at several measurement points when the wind direction is S. The difference between the CFD codes is also small in this case. Overall, the CFD results correspond well with the experiment and field measurement results.

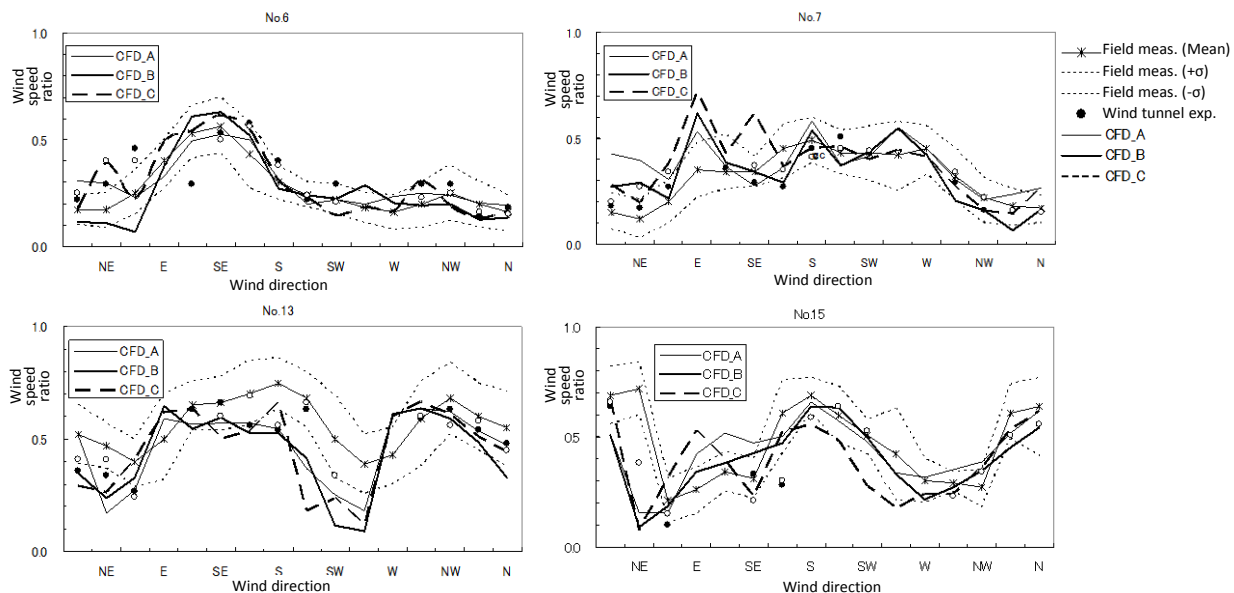


Figure 4-3-4. Comparison of wind speed ratios by wind direction at representative measurement points

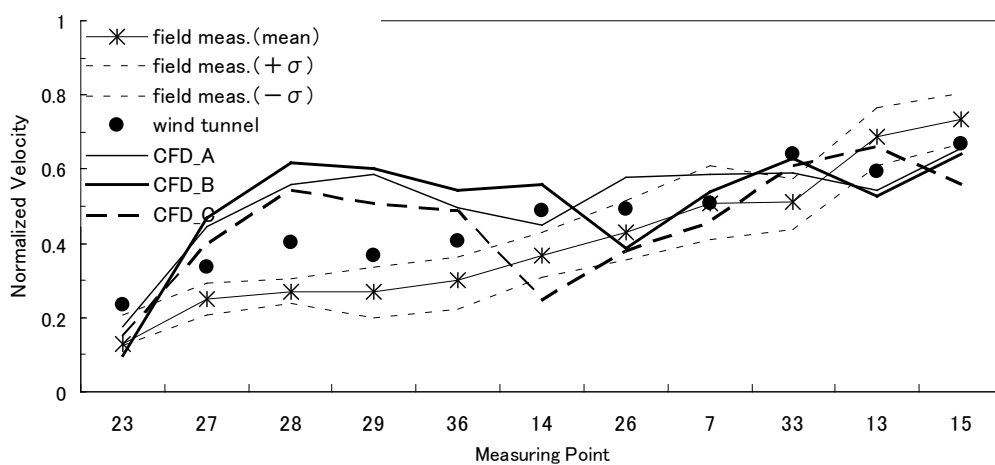


Figure 4-3-5. Comparison of wind speed ratio at each measurement point for wind direction S

4.3.4 Summary of the analysis of flow around a group of high-rise buildings in the Shinjuku sub-central area

CFD simulations were performed for the wind environment in and around a group of high-rise buildings in the Shinjuku sub-central area. The results were compared with those obtained from field measurements and a wind tunnel experiment. The following information was obtained:

- The CFD prediction results generally agreed well with the wind tunnel experiment and field measurement results for all the CFD codes.
- Around the low-rise buildings adjacent to the high-rise buildings, a higher grid resolution than that for the high-rise buildings is required to reproduce the building shapes. The results of the calculation that considered this point corresponded well with the field measurement and experiment results, even around the low-rise buildings.
- The CAD data used as the basis of the building complex model for the CFD analysis did not agree perfectly with the wind tunnel model, and this may be one reason for the differences between the experiment results and CFD results at some locations.

4.4 Summary of the benchmark tests of flow in actual city block

In the analyses of actual building complexes reported in this chapter, when the building geometries, grid resolutions, and boundary conditions were identical, there was little difference depending on the CFD code. However, the reproducibility and grid resolution of the building geometry are factors that influence the calculation results. For example, in the case of the building complexes in Niigata city, for which CAD data based on the existing wind tunnel model were used, slight differences between the model and the CAD data resulted in differences between the experiment results and the CFD prediction results. Consequently, in practical wind environment predictions, the building geometry in the planned buildings should be reproduced as accurately as possible, based on geographic information or field surveys. Moreover, CFD predictions are typically performed using a high-resolution grid only for the main object area to limit the computational load, while for other regions, a low-resolution grid is typically used. However, in a case such as the Shinjuku sub-city center, where low-rise buildings are densely concentrated over a wide area around a group of high-rise buildings and there are evaluation points among the low-rise buildings, the prediction accuracy is expected to be poor in the low-resolution region. When there are also evaluation points of interest outside the main area, such as around the planned building, it is necessary to be very careful in selecting the grid resolution for the surrounding area.

In the calculation example in the first half of this section, the z_0 -type logarithmic law, which was obtained from a wind tunnel experiment, was used as the ground surface boundary condition. However, it is presumed that for a case in which the shape of the surrounding buildings is reproduced exactly by the grid, the ground surface roughness is reproduced by the surrounding buildings. Thus, if the purpose of the calculation is not comparison with wind tunnel experiment results, it is not always essential to use the z_0 -type logarithmic law.

5. Benchmark test of flow around trees [45]

5.1 Introduction

This chapter discusses a benchmark test conducted using the tree canopy model used by various organizations for the flow in the wake of trees, which are often used as windbreak vegetation around buildings. A comparative study of its prediction accuracy was included. This benchmark test involved a comparison of the measurement results for the distributions of both the mean velocity and turbulent kinetic energy k in the flow around the Tsuiji Pines in the Izumo region, for which measurement results have been reported by Kurotani et al. [7]. The results of CFD analyses of this target were reported in refs. [30, 31].



Figure 5-1-1. Tsuiji Pines in Izumo District (courtesy of Shimane Prefecture Tourist Association)

5.2 Outline of measurements of objects for comparison

The target was the flow in the wake of the Tsuiji Pines (Figure 5-1-1). The Tsuiji Pines are screen-shaped black pines around homesteads seen in hamlets of scattered houses in the Izumo Plain in Shimane Prefecture. The field measurements were conducted at the west end of the playground of an elementary school in the town of Taisha in Hikawa-gun. The measurements were conducted twice—before and after the pruning of the Tsuiji Pines—but the benchmark test targeted the after-pruning state (shading rate: 81%). The size of the Tsuiji Pines is approximately $2\text{ m} (x) \times 74\text{ m} (y) \times 7\text{ m} (z)$. The streamwise flow direction is x , the direction lateral to the streamwise flow is y , and the vertical direction is z . According to ref. [7], using a movable observation tower equipped with three-dimensional ultrasonic anemometers at four heights— 1.5 m , 3 m , 4.5 m , and 6 m —the distributions of the average velocity and turbulent kinetic energy k were measured on the downwind side of the row of the vegetation (Figure 5-2-1).

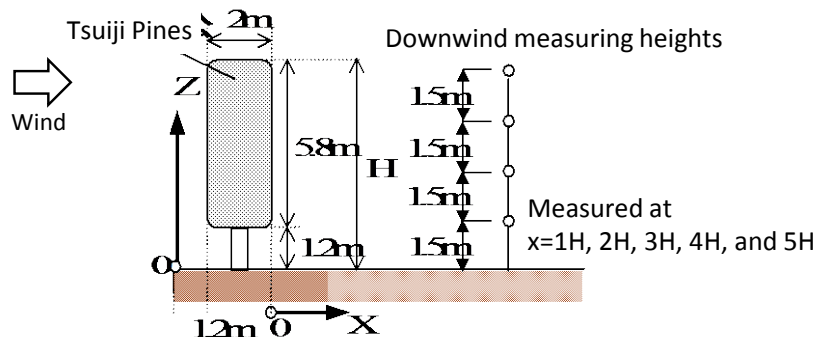


Figure 5-2-1. Configuration of test model

5.3 Outline of numerical calculations

A two-dimensional calculation of a vertical section ($x-z$ section) on the central axis of the Tsuiji Pines was performed. The results were compared with the results of measurements obtained under the condition of a wind direction perpendicular to the Tsuiji Pines. Table 5-3-1 lists the common calculation conditions for this benchmark test, and Table 5-3-2 lists the model used for this benchmark test. Table 5-3-3 lists the analysis cases.

The calculation conditions listed in Table 5-3-1 were designated as the basic condition. The turbulence model, grid discretization, ground surface boundary conditions, tree canopy model (Table 5-3-2) and its parameters, and model coefficients (a , C_f , C_{pe1}) were varied to examine their relative effects on the calculation results. Although no particular designation was provided concerning the selection of the turbulence model, most calculations were performed using the standard $k-\varepsilon$ model (Table 5-3-3). Moreover, although details were not designated for the tree canopy model, most calculations were performed use the type B model listed in Table 5-3-2 (Table 5-3-3). In some cases, to clarify the impact of the grid discretization, comparative calculations were performed using the calculation grids shown in Figures 5-3-1 and 5-3-2. In the analysis results reported in ref. [31], the fine grid discretization shown in Figure 5-3-2 was used. However, in wind environment prediction normally performed for practical purposes, the grid discretization has to be somewhat coarser than this. Thus, the grid discretization considered to be the basic one, shown in Figure 5-3-1, was set as the grid, with a resolution at the practical application level. A comparison of the results obtained using these two grids shows almost no difference between the average velocities, and the difference in k values was also relatively small (Figure 5-4-1). The calculation results were standardized based on the average wind velocity (U_h) at the tree height of the approaching flow.

Table 5-3-1. Outline of calculations

Computational domain	114 m in vertical direction(z), 48 m upwind of the tree, and 61 m downwind of the tree in streamwise direction(x)
Inflow boundary	The velocity profile was obtained by interpolating the measured values: $\langle u(z) \rangle = \langle u_b \rangle (z/H_b)^{0.22} [\text{m/s}]$ $\langle w(z) \rangle = 0 [\text{m/s}]$ $\langle u_b \rangle = 5.6 [\text{m/s}] \quad H_b = 9[\text{m}]$ (H_b : Reference measurement height of the approaching flow) $K = 3.02 [\text{m}^2/\text{s}^2]$ (Assuming a constant flux layer, k has no vertical variation) ε is provided by the assumption $P_k = \varepsilon$
Upper surface	Slip wall
Outflow boundary	Zero gradient
Ground surface	Not specified
Turbulence model	Not specified
Grid discretization	Basic grid: $37(x) \times 18(z)$; see Figure 5-3-1
Scheme for term	QUICK scheme for all variables
Tree canopy model	Not specified
Leaf area density	Measurement value ($a = 1.17 [\text{m}^2/\text{m}^3]$; see ref. [7])
Drag coefficient C_f	0.8 (see ref. [7])

Table 5-3-2. Tree canopy models (for details, see Section 2.8)

	F_i	F_k	F_ε
Type B [32]	$C_f a \overline{\langle u_i \rangle} \sqrt{\overline{\langle u_j \rangle}^2}$	$\overline{\langle u_i \rangle} F_i$	$\frac{\varepsilon}{k} C_{pe1} \overline{\langle u_i \rangle} F_i$
Type C [33]		$\overline{\langle u_i \rangle} F_i - 4\eta C_f a \sqrt{\overline{\langle u_j \rangle}^2} \cdot k$	$\frac{\varepsilon}{k} \left(C_{pe1} \overline{\langle u_i \rangle} F_i - C_{pe2} \cdot 4\eta C_f a \sqrt{\overline{\langle u_j \rangle}^2} \cdot k \right)$

F_i : Extra term of momentum equation, F_k : Extra term of k equation, F_ε : Extra term of ε equation

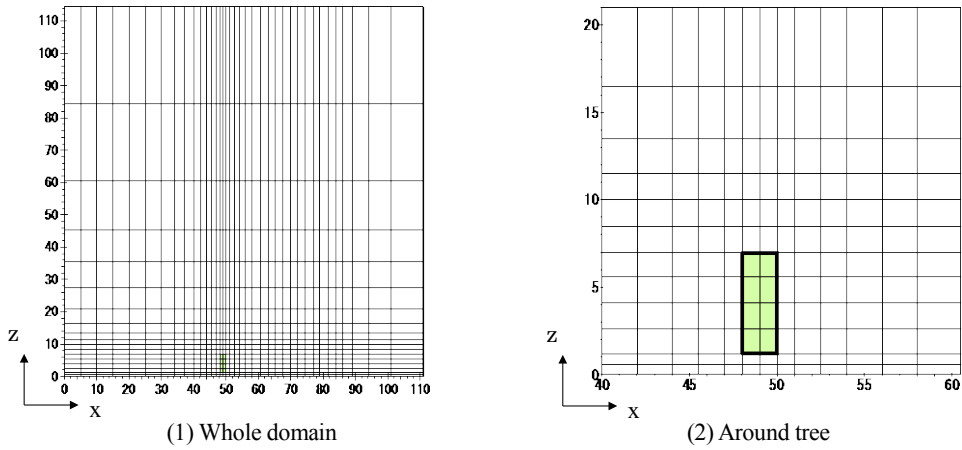


Figure 5-3-1. Basic grid discretization ($37(x) \times 18(z)$) (designated under basic conditions)

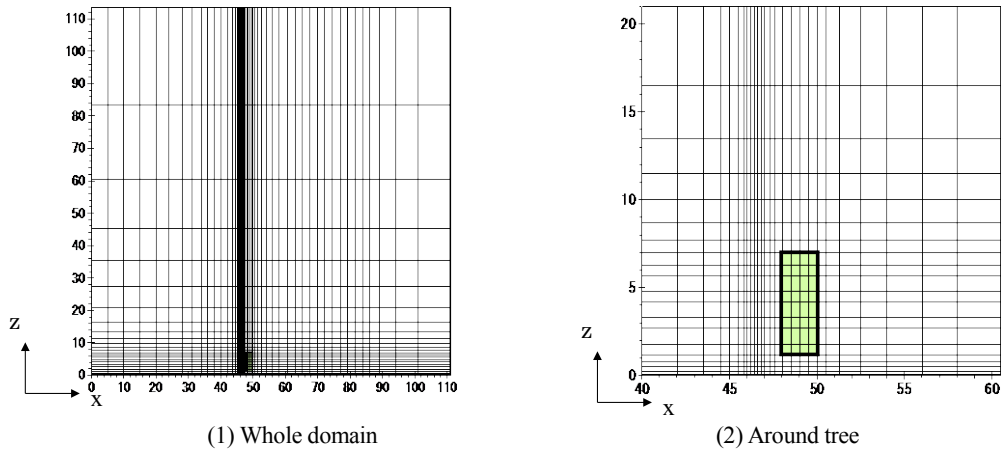


Figure 5-3-2. Finer grid discretization used for comparison (52 (x) \times 34 (z)) (cases TU2 and TU4 to 6 in Table 5-3-3)

Table 5-3-3. Analysis cases

Affiliation	Case	Code	Turbulence model	Grid discretization	Ground surface condition	Tree model (Type)	Model parameters and coefficients			
							Leaf area density a	Drag coefficient C_f	Model coefficient C_{pe1}	Model coefficient C_{pe2}
T	T1	Commercial	$k-\varepsilon$ (standard)	standard	Log law for smooth wall	B	1.17	0.8	1.8	—
	T2	Commercial	$k-\varepsilon$ (standard)	standard	Log law for smooth wall	B	1.17	0.8	2.0	—
TU	TU1	Self-made	LK	standard	Generalized log law for smooth wall	B	1.17	0.8	1.8	—
	TU2	Self-made	LK	finer	Generalized log law for smooth wall	B	1.17	0.8	1.8	—
	TU3	Self-made	$k-\varepsilon$ (standard)	standard	Generalized log law for smooth wall	B	1.17	0.8	1.8	—
	TU4	Self-made	LK	finer	Generalized log law for smooth wall	B	1.17	0.8	1.0	—
	TU5	Self-made	$S-\Omega$	finer	Generalized log law for smooth wall	B	1.17	0.8	1.8	—
	TU6	Self-made	$S-\Omega$	finer	Generalized log law for smooth wall	C	1.17	0.8	1.8	1.5
O	O1	Self-made	$k-\varepsilon$ (standard)	standard	Log law including z_0 ($z_0 = 0.0858$ m)	B	1.5	0.5	2.0	—

O2	Self-made	$k-\epsilon$ (standard)	standard	Log law including z_0 ($z_0 = 0.0858 \text{ m}$)	B	1.17	0.8	1.8	—
O3	Self-made	$k-\epsilon$ (standard)	standard	Log law including z_0 ($z_0 = 0.0858 \text{ m}$)	B	1.17	0.5	1.8	—
O4	Self-made	$k-\epsilon$ (standard)	standard	Log law including z_0 ($z_0 = 0.0858 \text{ m}$)	B	1.17	0.8	2.0	—
O5	Self-made	$k-\epsilon$ (standard)	standard	Log law including z_0 ($z_0 = 0.0858 \text{ m}$)	B	1.17	0.5	2.0	—
O6	Self-made	$k-\epsilon$ (standard)	standard	Generalized log law for smooth wall	B	1.5	0.5	2.0	—
O7	Self-made	$k-\epsilon$ (standard)	standard	Generalized log law for smooth wall	B	1.17	0.8	1.8	—
O8	Self-made	$k-\epsilon$ (standard)	standard	Generalized log law for smooth wall	B	1.17	0.5	1.8	—
O9	Self-made	$k-\epsilon$ (standard)	standard	Generalized log law for smooth wall	B	1.17	0.8	2.0	—
O10	Self-made	$k-\epsilon$ (standard)	standard	Generalized log law for smooth wall	B	1.17	0.5	2.0	—

5.4 Impact of boundary conditions/parameters

5.4.1 Impact of grid discretization (comparison of TU1 and TU2)

Figure 5-4-1 compares the mean streamwise velocity and the turbulent kinetic energy k behind the tree obtained from the calculations for the cases using the basic grid (Figure 5-3-1, TU1) and the finer grid (Figure 5-3-2, TU2). The LK model was used as the turbulence model. The predicted results for the mean velocity agree almost perfectly for both grids, and there is almost no effect of the different grid discretizations (Figure 5-4-1 (1)). In contrast, in the prediction results for the turbulent kinetic energy k , although the k values increase slightly with the finer grid (TU2), the difference is quite small (Figure 5-4-1(2)).

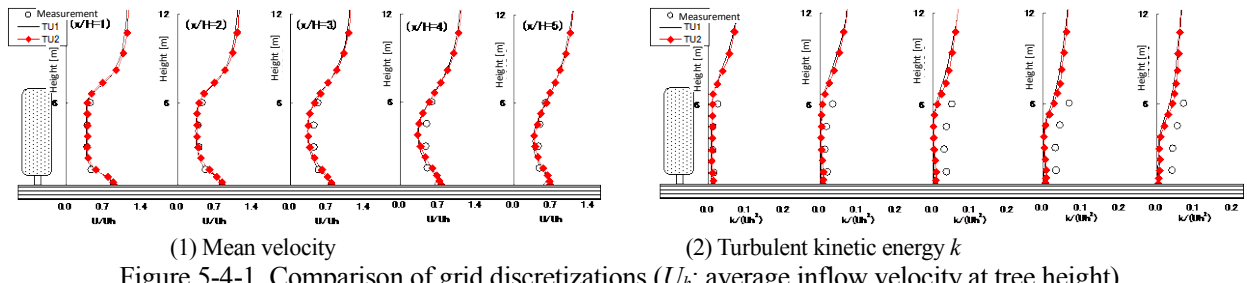


Figure 5-4-1. Comparison of grid discretizations (U_h : average inflow velocity at tree height)

5.4.2 Differences between analysis codes under identical conditions (comparison of TU1, TU3, and O7)

Figure 5-4-2 compares the results for three different CFD codes obtained under identical conditions. All of the CFD codes reproduce the tendency for the wind velocity to become small in the wake of the trees, and the results correspond well to the measured values (Figure 5-4-2(1)). The calculated turbulent kinetic energy k also corresponds well to the value measured just behind the trees. However, although the calculated values were lower than the measured values further downwind according to all of the CFD codes, the differences between the codes were larger than the differences in the mean velocity (Figure 5-4-2(2)).

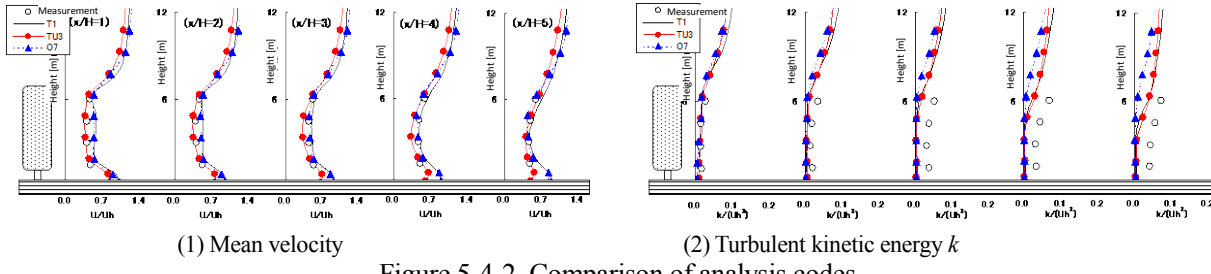


Figure 5-4-2. Comparison of analysis codes

5.4.3 Impact of turbulence model (TU1, TU3, TU2, and TU5)

Figure 5-4-3 compares the results of the predictions obtained using the standard $k-\varepsilon$ model (TU3) and LK model (TU1) for a case using the basic grid (Figure 5-3-1). No great differences were observed in either the mean wind velocity or k (Figure 5-3-4).

Figure 5-4-4 compares the results of predictions obtained using the LK model (TU2) and the S- Ω model (TU5) for a case in which the finer grid was used (Figure 5-3-2). In the results obtained using the S- Ω model, the mean wind velocity was a little larger and k was a little smaller than in the LK model. However, the differences between the two sets of results were equal to or smaller than the differences between the CFD codes under identical conditions, shown in Figure 5-4-2.

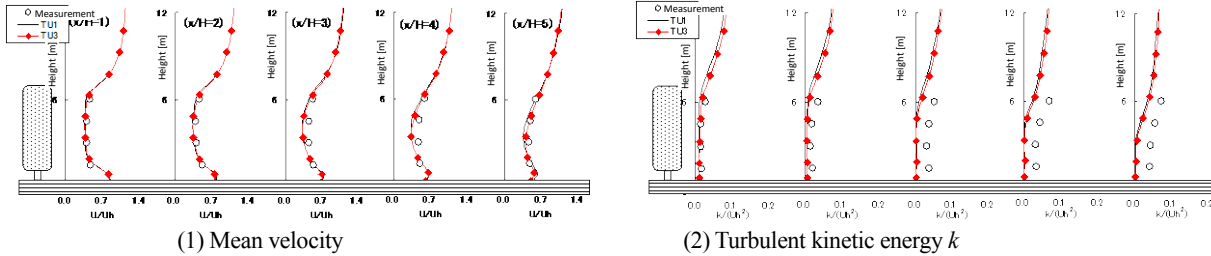


Figure 5-4-3. Impact of turbulence model (with basic grid)

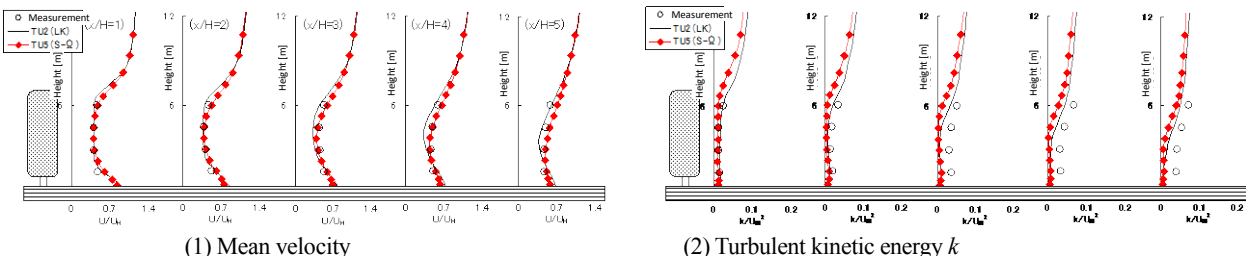


Figure 5-4-4. Impact of turbulence model (with finer grid)

5.4.4 Impact of ground surface boundary conditions (comparison of O2 and O7)

Figure 5-4-5 shows the results for a case in which the logarithmic law including z_0 was used (O2) and a case in which the logarithmic law for a smooth wall surface was used (O7) for the ground surface boundary condition. A difference between the two sets of results was observed in the lower part of the canopy (height 0 to 1.2 m). Although the flow is accelerated under the canopy in the O7 case (the smooth surface condition), the velocity decreases near the ground surface in the O2 case (the rough surface condition). Therefore, there is a great difference near the ground surface (Figure 5-4-5(1)). However, this difference has almost no impact on the distribution of the mean velocity and turbulent kinetic energy k at the canopy height and greater heights.

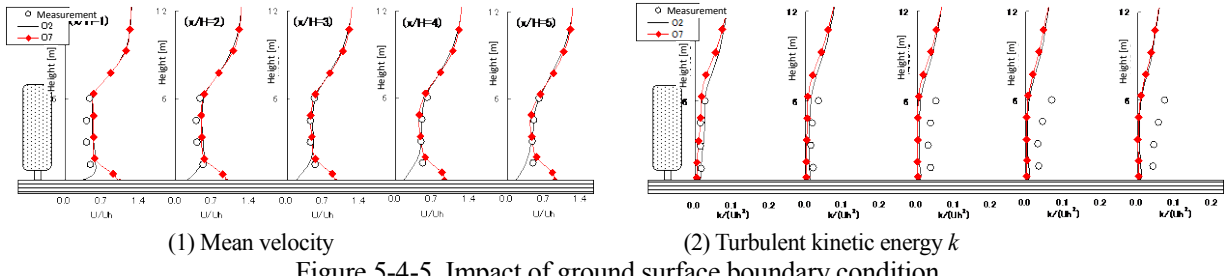


Figure 5-4-5. Impact of ground surface boundary condition

5.4.5 Impact of leaf area density a (comparison of O6 and O10)

Figure 5-4-6 compares the results obtained using the tree canopy model type B (Table 5-3-2) for the two different leaf area densities a , i.e., 1.5 (O6) and 1.17 (O10). A larger leaf area density a results in a smaller wind speed in the wake of the trees, but the difference is small.

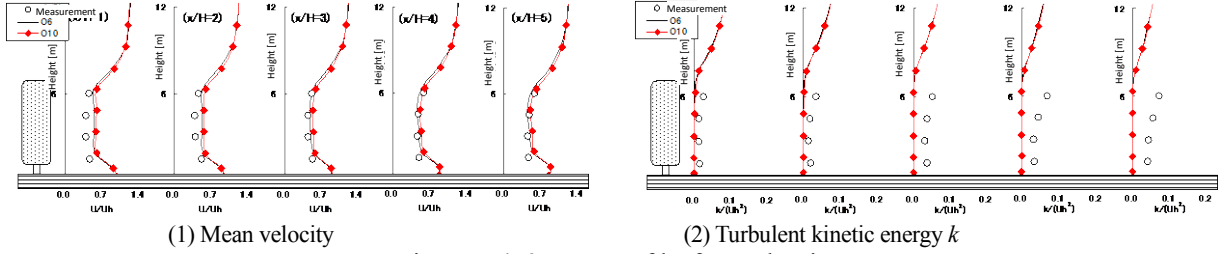
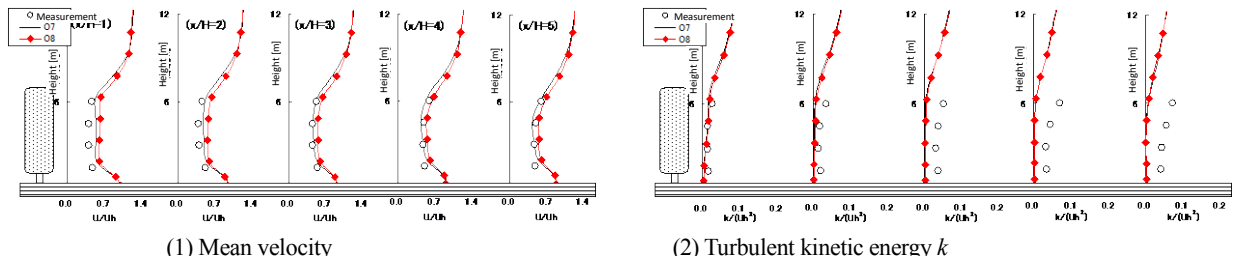


Figure 5-4-6. Impact of leaf area density

5.4.6 Impact of resistance coefficient C_f (comparison of O7 and O8)

Figure 5-4-7 compares the results obtained using the tree canopy model type B for the two different resistance coefficients C_f , i.e., 0.8 (O7) and 0.5 (O8). The change in the case of the larger C_f is similar to the case with the larger leaf area density. In other words, the wind velocity in the wake of the trees is slightly smaller when C_f is larger, but there is almost no difference in the k distributions.

Figure 5-4-7. Impact of resistance coefficient C_f

5.4.7 Impact of model coefficient C_{pel} (comparison of TU2 and TU4)

Figure 5-4-8 compares the cases in which the model coefficient C_{pel} , which is included in the extra term F_e in the ε equation in the tree canopy model type B (Table 5-3-2), was considered to be 1.8 (TU2) and 1.0 (TU4). In this calculation, the basic grid (Figure 5-3-1) was not used, but the finer one (Figure 5-3-2) was used. The LK model was used as the turbulence model. In the case in which $C_{pel} = 1.0$, almost no velocity deficit was observed, and the value of k was very different from the measured one. It should be noted that the impact of a change in C_{pel} is much greater than that of a change in either the leaf area density a or the resistance coefficient C_f . However, according to ref. [31], in the C_{pel} range of 1.5–2.0, the impact on the prediction results is relatively small, and overall, the results for $C_{pel} \approx$

1.8 agree most closely with measured results.

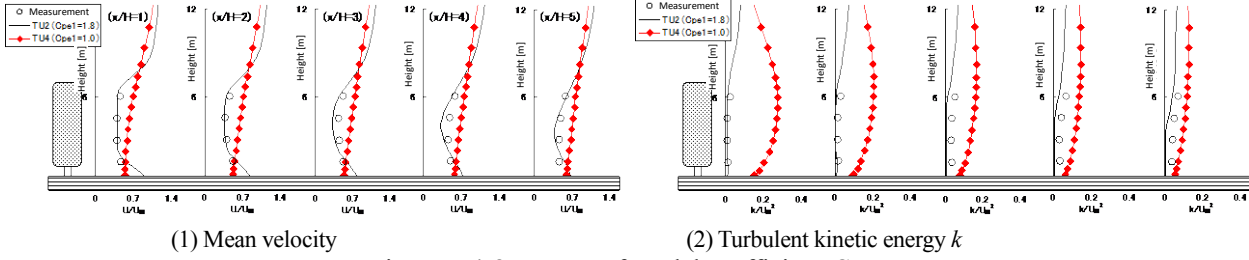


Figure 5-4-8. Impact of model coefficient C_{pcl}

5.4.8 Comparison of type B and type C tree canopy models (comparison of TU5 and TU6)

Figure 5-4-9 compares the results for the cases using the tree canopy models type B (TU5) and type C (TU6) listed in Table 5-3-2. In ref. [31], the model coefficients (C_{pcl}) included in type B and in type C were changed to investigate their impacts on the prediction results. For the TU5 and TU6 cases, the values of the model coefficients that yielded the best agreement with the measurements in each case (type B and type C), were used. The velocity deficit effects were reproduced by all the models, but in the type C case, the velocity tended to be slightly larger than the measured value. The distribution of k , on the other hand, was more accurately reproduced by the type C, from the wake of the trees to downwind, than by the type B.

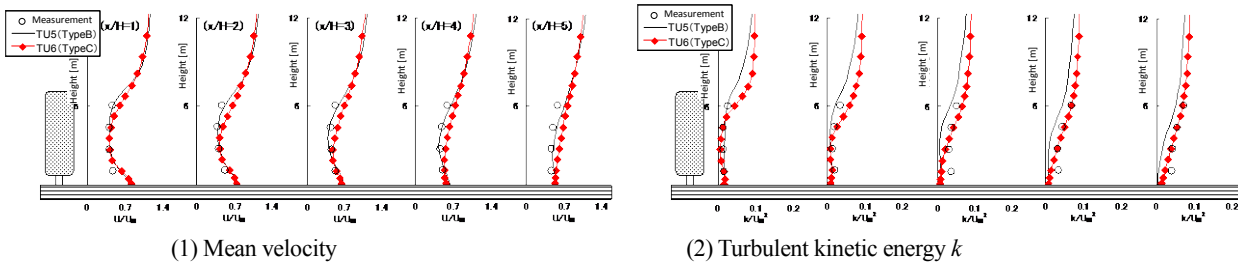


Figure 5-4-9. Comparison of type B and type C tree canopy models

5.5 Summary of the benchmark test of flow around trees

Benchmark tests for the flow around trees were performed using tree canopy models. The mean wind velocity and turbulent kinetic energy k were compared with the measured values. The following information was obtained:

- When the grid discretization, turbulence model, tree canopy model, boundary conditions, and other conditions were identical, even using different CFD codes, almost identical results were obtained.
- When the leaf area density a , resistance coefficient C_f , and model coefficient C_{pcl} included in the tree canopy model type B were changed parametrically, the model coefficient C_{pcl} had the greatest impact on the calculation results.
- In cases that used the type B tree canopy model, all cases for which C_{pcl} was 1.8 or 2.0 accurately reproduced the velocity deficit effects downwind of the trees. Overall, good correspondence between the calculations and measurements was shown.
- The type B results showed that the predicted value of k was slightly smaller than the measured value further downwind of the trees.

- In the results for the type C tree canopy model, the distribution of k in the wake of the trees was reproduced more accurately than in the type B case, but the average wind velocity differed slightly from the measured values. However, the agreement could be improved by optimizing the model coefficients in more detail in a future study.

References

- [1] Y. Meng, K. Hibi (1998): Turbulent measurements of the flow field around a high-rise building, *Journal of Wind Engineering, Japan Association for Wind Engineering*, **76**, 55-64. (in Japanese)
- [2] K. Uehara, S. Wakamatsu, R. Ooka (2003): Studies on critical Reynolds number indices for wind-tunnel experiments on flow within urban areas, *Boundary-Layer Meteorology*, **107**, 353-370.
- [3] T. Miyazaki, Y. Tominaga (2003): Wind tunnel experiment on flow field around a building model with a scale ratio of 4:4:1 placed with in the surface boundary layer, *Proceedings of Annual Meeting of Hokuriku Chapter, Architectural Institute of Japan*, 201-204. (in Japanese)
- [4] Y. Nonomura, N. Kobayashi, Y. Tominaga, A. Mochida (2003): The cross comparison of CFD results for flow field around building models (Part 3) - Wind tunnel test for the verification of models for the flow field around building blocks, *Summaries of Technical Papers of Annual Meeting, Japan Association for Wind Engineering*, **95**, 83-84. (in Japanese)
- [5] K. Fujii, Y. Asami, Y. Iwasa, Y. Fukao et al. (1978): Wind in Shinjuku sub-central area - Comparison between field measurement and wind tunnel experiment, *Proceedings of 5th Symposium on Wind Resistance of Structures*, 91-98. (in Japanese)
- [6] The Research Committee on Strong Wind Around High-rise Buildings, Development Council of Shinjuku Sub-central Area: Technical Report on Wind in Shinjuku Sub-central Area -Field Measurement, Experiment, and Observation. (in Japanese)
- [7] Y. Kurotani, N. Kiyota, S. Kobayashi (2001): Windbreak effect of Tsujiimatsu in Izumo Part. 2, *Summaries of Technical Papers of Annual Meeting of the Architectural Institute of Japan (D-2)*, 745-746. (in Japanese)
- [8] Working Group for CFD Prediction of Wind Environment Around Building, Air Environment Sub-committee, Environment Engineering Committee, AIJ (2001): Development of CFD method for predicting wind environment around a high-rise building - Part 1 Cross comparison of CFD results using various $k-\epsilon$ models, *Journal of Technology and Design, Architectural Institute of Japan*, **12**, 119-124. (in Japanese)
- [9] S. V. Patankar, (1980): *Numerical Heat Transfer and Fluid Flow*, Hemisphere, New York.
- [10] A. Mochida, S. Murakami, Y. Hayashi (1991): Comparison between $k-\epsilon$ model and LES for turbulence structure around a cube, *Journal of Architecture, Planning and Environmental Engineering, Architectural Institute of Japan*, **423**, 23-31. (in Japanese)
- [11] R. Ooka, A. Mochida, S. Murakami, Y. Hayashi (1997): Examining ASM by means of wind tunnel test, LES and DSM numerical simulation of anisotropic turbulent flow field around cubic model by means of ASM, *Journal of Architecture, Planning and Environmental Engineering, Architectural Institute of Japan*, **495**, 61-68. (in Japanese)
- [12] S. Sakamoto, A. Mochida, S. Murakami, W. Rodi (1994): Comparison of LES with DSM, $k-\epsilon$ and experiments for turbulent vortex shedding flow past 2-D square cylinder, *Journal of Structural and Construction Engineering, Architectural Institute of Japan*, **459**, 49-56. (in Japanese)
- [13] A. Mochida, S. Murakami, Y. Tominaga, H. Kobayashi (1996): Comparison between standard and dynamic types of Smagorinsky SGS model - Large eddy simulation of turbulent vortex shedding flow past 2-D square

- cylinder using dynamic SGS model (Part 1), *Journal of Architecture, Planning and Environmental Engineering, Architectural Institute of Japan*, **479**, 41-47. (in Japanese)
- [14] Y. Tominaga, S. Murakami, A. Mochida (1997): LES prediction of gas diffusion near building using dynamic mixed SGS model based on composite grid technique, *Journal of Architecture, Planning and Environmental Engineering, Architectural Institute of Japan*, **496**, 53-58. (in Japanese)
- [15] T. S. Lund (1998): Generation of turbulent inflow data for spatially-developing boundary layer simulations, *Journal of Computational Physics*, **140**, 233-258.
- [16] H. Kataoka, M. Mizuno (1999): Numerical flow computation around 3-D square cylinder using inflow turbulence, *Journal of Architecture, Planning and Environmental Engineering, Architectural Institute of Japan*, **523**, 71-77. (in Japanese)
- [17] H. Werner and H. Wengle (1991): Large eddy simulation of turbulent flow over and around a cube in a plate channel, *8th Symposium on Turbulent Shear Flows*, 155-168.
- [18] Y. Ishida, A. Mochida, Y. Tominaga, T. Shirasawa (2003): LES of flow around a high-rise building with generated inflow turbulence, *Proceedings of the 17th Symposium on Computational Fluid Dynamics*, E6-1. (in Japanese)
- [19] Y. Ishida, S. Murakami, R. Ooka, A. Mochida (1999): Study on method for reducing numerical oscillation for LES of flow around a cube - 3-D CFD analysis with staggered grid system based on generalized curvilinear coordinates (Part 2), *Journal of Architecture, Planning and Environmental Engineering, Architectural Institute of Japan*, **521**, 63-71. (in Japanese)
- [20] Y. Ishida, Y. Tominaga, A. Mochida (2003): LES of flow around a high-rise building with generated inflow turbulence, *Summaries of Technical Papers of Annual Meeting, Architectural Institute of Japan (D-2)*, 757-758. (in Japanese)
- [21] M. Hino (1977): *Spectrum Analysis*, Asakura Publishing Co., Ltd., 221. (in Japanese)
- [22] H. Kataoka (2003): Large eddy simulation of turbulent flow around a 4:4:1 square cylinder, *Journal of Wind Engineering, Japan Association for Wind Engineering*, **95**, 87-88. (in Japanese)
- [23] T. H. Shih, W. W. Liou, A. Shabbir, Z. Yang, J. Zhu (1995): A new $k-\epsilon$ eddy viscosity model for high Reynolds number turbulent flows, *Computers & Fluids*, **24**(3), 227-238.
- [24] V. Yakhot, S. A. Orszag, S. Thangam, T. B. Gatski, C. G. Speziale (1992): Development of turbulence models for shear flows by a double expansion technique, *Physics of Fluid A*, **4**(7), 1510-1520.
- [25] T. H. Shih, J. Zhu, J. L. Lumley (1993): A Realizable Reynolds Stress Algebraic Equation Model, *NASA*, TM-105993.
- [26] P. A. Durbin (1996): On the $k-\epsilon$ stagnation point anomaly, *International Journal of Heat and Fluid Flow*, **17**, 89-90.
- [27] B. E. Launder and M. Kato (1993): Modeling flow-induced oscillations in turbulent flow around a square cylinder, *ASME Fluid Engineering Conference*, **157**, 189-200.
- [28] K. Abe, Y. Nagano, T. Kondoh (1992): An improved $k-\epsilon$ model for prediction of turbulent flows with separation and reattachment, *Transactions of the JSME*, B, **58**(554), 3003-3010. (in Japanese)
- [29] H. Hattori, K. Inagaki, Y. Nagano (2002): Turbulence model for prediction of flow over a local area, *Proceedings of the 16th Symposium on Computational Fluid Dynamics*, B13-4. (in Japanese)

- [30] J. Suzuki, S. Yoshida, R. Ooka, Y. Kurotani (2002): Study on windbreak effect of Tsujimatsu in Izumo using CFD analysis, *Summaries of Technical Papers of Annual Meeting, Architectural Institute of Japan (D-1)*, 871-872. (in Japanese)
- [31] T. Iwata, A. Kimura, A. Mochida, H. Yoshino (2004): Optimization of tree canopy model for CFD prediction of wind environment at pedestrian level, *Proceedings of the 18th National Symposium on Wind Engineering*, 69-74. (in Japanese)
- [32] I. Uno, H. Ueda, S. Wakamatsu (1989): Numerical modeling of the nocturnal urban boundary layer, *Boundary-Layer Meteorology*, **49**, 77-98.
- [33] S. R. Green (1992): Modelling turbulent air flow in a stand of widely-spaced trees, *PHOENICS Journal Computational Fluid Dynamics and Its Applications*, **5**(3), 294-312.
- [34] Y. Tominaga, A. Mochida, R. Yoshie, H. Kataoka, T. Nozu, M. Yoshikawa, T. Shirasawa (2008): AIJ guidelines for practical applications of CFD to pedestrian wind environment around buildings, *Journal of Wind Engineering and Industrial Aerodynamics*, **96**(10-11), 1749-1761.
- [35] Architectural Institute of Japan (2006): *AIJ Recommendations for Loads on Buildings*. 2004 Edition, Architectural Institute of Japan.
- [36] S. Murakami, Y. Iwasa, Y. Morikawa (1983): Investigation of statistical characteristics of wind at ground level and criteria for assessing wind-induced discomfort - Part III criteria for assessing wind-induced discomfort, *Transactions of the Architectural Institute of Japan*, (325), 74-84. (in Japanese)
- [37] S. Murakami, Y. Iwasa, Y. Morikawa (1986): Study on acceptable criteria for assessing wind environment at ground level based on residents' diaries, *Journal of Wind Engineering and Industrial Aerodynamics*, **24**(1), 1-18.
- [38] M. Tsuchiya, S. Murakami, A. Mochida, K. Kondo, Y. Ishida (1997): Development of a new $k-\varepsilon$ model for flow and pressure fields around bluff body, *Journal of Wind Engineering and Industrial Aerodynamics*, **67&68**, 169-182.
- [39] A. Mochida, Y. Tominaga, S. Murakami, R. Yoshie, T. Ishihara, R. Ooka (2002): Comparison of various $k-\varepsilon$ model and DSM applied to flow around a high-rise building - report on AIJ cooperative project for CFD prediction of wind environment -, *Wind & Structures*, **5**(2-4), 227-244.
- [40] Y. Tominaga, A. Mochida, S. Murakami, S. Sawaki (2008): Comparison of various revised $k-\varepsilon$ models and LES applied to flow around a high-rise building model with 1:1:2 shape placed within the surface boundary layer, *Journal of Wind Engineering and Industrial Aerodynamics*, **96**(4), 389-411.
- [41] Y. Tominaga, A. Mochida, T. Shirasawa, R. Yoshie, H. Kataoka, K. Harimoto, T. Nozu (2004): Cross Comparisons of CFD Results of Wind Environment at Pedestrian Level around a high-rise Building and within a Building Complex, *Journal of Asian Architecture and Building Engineering*, 63-70.
- [42] R. Yoshie, A. Mochida, Y. Tominaga, H. Kataoka, K. Harimoto, T. Nozu, T. Shirasawa (2007): Cooperative project for CFD prediction of pedestrian wind environment in the Architectural Institute of Japan, *Journal of Wind Engineering and Industrial Aerodynamics*, **95**(9-11), 1551-1578.
- [43] R. Yoshie, A. Mochida, Y. Tominaga, H. Kataoka, M. Yoshikawa (2005): Cross Comparisons of CFD Prediction for Wind Environment at Pedestrian Level around Buildings - Part 1 Comparison of Results for Flow-field around a High-rise Building Located in Surrounding City Blocks, *The Sixth Asia-Pacific Conference*

on Wind Engineering (APCWE-VI), Seoul, Korea, September 12-14, 2005

- [44] Y. Tominaga, R. Yoshie, A. Mochida, H. Kataoka, K. Harimoto, T. Nozu (2005): Cross Comparisons of CFD Prediction for Wind Environment at Pedestrian Level around Buildings - Comparison of Results for Flowfield around Building Complex in Actual Urban Area, *The Sixth Asia-Pacific Conference on Wind Engineering (APCWE-VI)*, Seoul, Korea, September 12-14, 2005
- [45] A. Mochida, Y. Tabata, T. Iwata, H. Yoshino (2008): Optimization of Tree Canopy Model for CFD Prediction of Wind Environment at Pedestrian Level, *Journal of Wind Engineering and Industrial Aerodynamics*, **96**(10-11), 1667-1677.